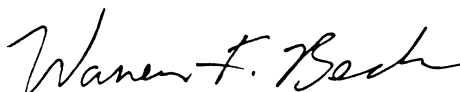This is to certify that the

dissertation entitled

Reactive intermediates and structure determination

of heme proteins studied by using Resonance Raman

spectroscopy   presented by

Jose F. Cerda

has been accepted towards fulfillment
of the requirements for

___Ph.D.___ degree in _Chemistry_

Warren F. Beck
Major professor

Date _26 April 2002_

PLACE IN RETURN BOX to remove this checkout from your record.
TO AVOID FINES return on or before date due.
MAY BE RECALLED with earlier due date if requested.

DATE DUE	DATE DUE	DATE DUE
JAN 1 0 2006		
JAN 1 1 2006		JUN 2 6 2004

REACTIVE INTERMEDIATES AND STRUCTURE DETERMINATION OF HEME

PROTEINS STUDIED BY USING RESOSNANCE RAMAN SPECTROSCOPY

By

Jose F. Cerda

A DISSERTATION

Submitted to
Michigan State University
in partial fulfillment of the requirements
for the degree of

DOCTOR OF PHILOSOPHY

Department of Chemistry

2002

ABSTRACT

REACTIVE INTERMEDIATES AND STRUCTURE DETERMINATION OF HEME PROTEINS STUDIED BY USING RESOSNANCE RAMAN SPECTROSCOPY

By

Jose F. Cerda

Resonance Raman (RR) spectroscopy is particularly useful for studies involving metalloporphyrin enzymes because of the enhancement effect from the porphyrin scattering due to its strong absorption. The RR technique has been used to study the reaction of cytochrome c oxidase (CcO) with O_2, characterize the peroxidase site of prostanglandin H synthase-1 (PGHS-1), and the study of histidine rich protein II ($HR_{ich}P$-II) and the effects of the anti-malarial drug chloroquine (CQ) on the heme-bound structure.

Time resolved RR spectroscopy has been used in the past to detect transient intermediates formed during O_2 reduction in CcO, and a number of intermediates, identified by their oxygen-isotope sensitive iron-ligand modes, have been detected. There is a consensus on the vibrations of several of the intermediates that are formed in the reaction of the fully reduced CcO and O_2. However, due its transient nature, there has been a controversy as to whether the first intermediate that is produced after the O-O bond cleavage, P_r, can be detected by time resolved RR. In this study, the P_r intermediate has been detected with at about 50 µs after the O_2 binding. This species shows a vibration at 804 cm^{-1} and is assigned to a ferryl-oxo heme intermediate. In addition, careful examination of the spectra produced by 10-ns laser pulses revealed a new vibration at 590/543 cm^{-1} for the reaction between fully reduced CcO and $^{16}O_2/^{18}O_2$. This

mode parallels the formation of the 786 cm^{-1} band, from the ferryl-oxo unit of Compound F. The intensity of the 590 cm^{-1} mode increases at higher probe power at the expense of the 786 cm^{-1} mode, indicative of a photoreaction involving this ferryl-oxo compound.

Resonance Raman spectroscopy was used to gain insights in to the structure of the peroxidase site of PGHS-1. This enzyme has an unusually weak bond between the heme iron and the proximal histidine compared to that of other peroxidases. A strong bond between the heme iron and the imidazolate at the proximal position is believed to play an essential role in the mechanism of O-O bond cleavage by most known peroxidases. However in PGHS-1, the proximal ligand plays a more important role in terms of the stability of the intermediates that are formed during the peroxidase reaction. Since a tyrosyl radical is formed in PGHS-1, the weaker proximal histidine makes the ferryl-oxo intermediate in PGHS-1 (Compound I) a better oxidant than that of other peroxidases that are involved instead in the oxidation of substrates.

Malaria infects the red blood cells and digests hemoglobin and uses an enzyme, HR$_{ich}$P-II, to aggregate the free hemes into an insoluble polymer called hemozoin. HR$_{ich}$P-II can bind up to 50 hemes to form a stable heme-bound protein. The resonance Raman spectroscopic results indicate that the majority of the hemes, in the 50-heme-bound HR$_{ich}$P-II, are 6-coordinate, low-spin with two histidines as the axial ligands. The addition of the antimalarial agent, chlroquine (CQ), to heme-bound HR$_{ich}$P-II results in the formation a free heme-CQ complex. Therefore, CQ may act by sequestering the heme from the heme-bound HR$_{ich}$P-II to form a heme-CQ complex.

To the memory of my grandparents, Joyce & Juan

TABLE OF CONTENTS

LIST OF TABLES

LIST OF FIGURES

LIST OF ABBREVIATIONS

2MeIm	2-methyl imidazole
5-c	5 coordinate
6-c	6 coordinate
a	heme a in cytochrome c oxidase
a_3	heme a_3 in cytochrome c oxidase
APX	cystolic ascorbate peroxidase
ARP	*Arthromyces ramosus* peroxidase
Asp	aspartate
ATP	adenosine triphosphate
BP1	barley peroxidase
CCD	charged couple device
CcO	cytochrome c oxidase
CcP	cytochrome c peroxidase
CIP	*Coprinus cinereus* peroxidase
Compound F	intermediate F in cytochrome c oxidase
Compound O	intermediate O in cytochrome c oxidase
Compound P_m	intermediate P_m in cytochrome c oxidase
Compound P_r	intermediate P_r in cytochrome c oxidase
COX	cyclooxygenase
CQ	chloroquine
cys	cysteine
D	aspartate

EPR	electron paramagnetic resonance
FRCcO	fully reduced cytochrome c oxidase
Hb	hemoglobin
HHMb	horse heart myoglobin
his	histidine
$HR_{ich}P\text{-}II$	histidine rich protein II
HRP	horseradish peroxidase
HRP-C	horseradish peroxidase isoenzyme C,
hs	high spin
Im	imidazole
ls	low spin
Mb	myoglobin
MPO	myeloperoxidase
MVCcO	mixed-valance cytochrome c oxidase
N	asparagine
OEP	octaethylporphoryrin
PGHS	prostaglandin H synthase
PP	protoporphorin-IX
RR	resonance Raman
sGc	soluble guanylate cyclase
TRRR	time resolved resonance Raman
tyr	tyrosine
Y	tyrosine

CHAPTER I: Application of Resonance Raman to Heme Proteins

1.1 Introduction

Heme proteins are involved in a wide range of functions, from electron transfer to complex substrate modification. The catalytic site of a heme protein not only comprises the heme cofactor, but also its surrounding amino acids, which can play as important a role as the heme. Proteins can control the reactivity of the iron through the porphyrin ring (shown in Figure 1.7). In this regard, proteins can use the same heme cofactor to perform different tasks. For example, the heme iron in hemoglobin (Hb) and myoglobin (Mb) is used to simply bind O_2, i.e. an oxygen carrier, while in horseradish peroxidase (HRP) the same type of heme is used to reduce H_2O_2 to H_2O. There are many questions as to how the proteins utilize effectively the same heme cofactors to achieve different metabolic functions. For example, in cytochrome c oxidase (CcO), the energy that results from O-O splitting is used for proton translocation. This means that there is a tight coupling between O_2 reduction and the movement of protons within this membrane enzyme. A great deal of effort has been focused on understanding how this machinery works. Although good progress has been made in understanding how O_2 is reduced in CcO, far more needs to be done because processes such as electron and proton transfers within an enzyme are still not well understood.

The heme pocket is normally the active site of enzymes, so the understanding of how proteins control the reactivity of the heme iron can begin by studying the heme and its surrounding amino acids. Heme proteins that are not used for electron transfer normally have five-coordinate hemes. The side of the heme that is coordinated to protein by a covalent bond between the heme iron and an amino acid residue is known as the

1

proximal site. This proximal residue is normally a histidine (his), cysteine, or tyrosine ligand. In CcO, the proximal ligand is a histidine, while in P-450$_{cam}$ (a monooxygenase) a cysteine acts as the proximal residue. The other side of the heme protein is known as the distal side, which interacts with the iron-bound ligands. While heme proteins tend to have small variations in their proximal ligand site, the distal side can be of varied configurations. For example, in heme peroxidases, the distal side is normally composed by a histidine-arginine pair that assists the O-O splitting during the peroxidase reaction. On the other hand, CcO has a very distinct configuration in its distal side, mainly composed by a copper (Cu$_B$) that interacts strongly with the heme iron from heme a_3. The reason for the distinct conformations in the distal sites to achieve the same goal (i.e. O-O splitting) needs to be still understood. These types of questions can be answered by obtaining detailed information, at the atomic level, of the heme pocket. A technique that is useful, in this respect, is resonance Raman spectroscopy. The resonance Raman spectrum not only contains vibrations from the heme macrocycle but also contain information on the iron-ligand modes that are affected by the proximal and distal sites. The various proximal and distal configurations affect the heme in different manners, so resonance Raman spectroscopy can be used to learn about the distinct mode of operations of heme proteins. In this thesis, resonance Raman spectroscopy has been used to understand different metabolic processes that are performed by different heme proteins.

The structure of the heme intermediates that are formed during the conversion of O$_2$ to H$_2$O in CcO will be discussed in Chapter I. The main objective of this chapter is a description of the use of nanosecond time-resolved resonance Raman spectroscopy for the detection of the first intermediate that is immediately formed after O-O bond

2

cleavage. The information about the oxy structure of this species is important because of the importan question of the coupling between the O-O splitting process and the proton pumping. As will be discussed, there are various conflicting proposals about the nature of the structures of the hemes in CcO at this stage of the reaction. Resonance Raman spectroscopy cannot provide a complete picture on proton movement in CcO because it only yields information about the structure of the heme pockets. However, it is a useful technique for the identification of heme intermediates, in the O-O splitting mechanism in CcO.

In Chapter III, the Raman spectroscopic properties of another heme protein involved in O-O splitting, prostaglandin h synthase-1 (PGHS-1) will be reported. This enzyme converts arachidonic acid into the endoperoxide, hydroperoxide, prostaglandin G_2 (PGG$_2$) and then reduces it to its corresponding alcohol, prostaglandin H_2 (PGH$_2$), which is a precursor for the formation of other metabolic substrates. This enzyme has two types of activities, a cyclooxygenase and a peroxidase. The cyclooxygenase reaction in PGHS-1 is coupled to the peroxidase reaction through the formation of heme intermediates during the substrate modification. From the results obtained by stopped-flow methods (1), various heme intermediates are formed during the peroxidase reaction. However, none of these intermediates have been detected by Raman spectroscopy. In this thesis, the properties of the proximal site of the heme pocket of PGHS-1 will be compared to that of other peroxidases. As will be shown, there are differences in the heme pockets between PGHS-1 and other known peroxidases. Although Chapter III does not include the study of the heme intermediates that are formed in the peroxidase reaction of PGHS-1, it is proposed that the stability of these is affected by the heme pocket

configuration. Thus, the heme pocket configuration has been studied by the application of resonance Raman spectroscopy to the resting, ferrous, and CO-bound ferrous states of PGHS-1 and compared to that of other well known heme peroxidases.

In the final chapter (Chapter IV) the structure of the heme in histidine rich protein II (HR$_{ich}$P-II) will be discussed. The malarial parasite, *Plasmodium falciparum*, produces this enzyme, which acts as a sponge for as many as 50 hemes; it binds and polymerizes the hemes into a compound called hemozoin. In this thesis, the heme-bound protein has been characterized by resonance Raman spectroscopy. In addition, the anti-malarial properties of chloroquine have been studied by using resonance Raman. The mode of action of this anti-malarial drug will be discussed in light of its effects on the structure of heme-bound HR$_{ich}$P-II.

1.2 Resonance Raman spectroscopy and its applicability to heme proteins

Vibrational information can be obtained by infrared (IR) or Raman spectroscopy. In the infrared absorption process, the molecule absorbs IR radiation, which results in a vibrational transition. On the other hand, the Raman phenomenon is a scattering process in which there is an energy exchange between the scattered photons and the molecule. In Raman spectroscopy, high intense electromagnetic radiation is used to induce a dipole moment within the molecule; this is achieved by the use of Lasers. When a molecule is irradiated by the Laser light at a frequency, v_L, two types of scattering are produced: Rayleigh and Raman scattering. The Rayleigh scattering derives from photons that have not exchanged energy with the system. This type of scattering is detected at a frequency, v_L. During the Raman effect, the molecule exchanges energy with the

scattered photons to produce vibrational transitions. The Raman scattered photons are detected at frequencies $v_L \pm v_i$, where v_i is the frequency of vibration of the ith mode. Figure 1.1 shows a schematic representation of the two types of Raman scattering that can occur. The photons at frequencies $v_L - v_i$, are known as the Stokes scattering and are produced by transitions from an initial vibrational ground level to a higher one. The anti-Stokes lines have frequencies at $v_L + v_i$, in which the system has undergone through a transition that results in a final lower vibrational state than its initial one.

A brief description of the theory of Raman scattering will be described, following the treatment used by Rousseau $et\ al.$ (2). The expression that describes the intensity of the Raman scattering, I_s, resulting from a transition from an initial ground state, G, to the final state, F, is the following:

$$I_S = \left(\frac{2^7 \pi^5}{9}\right) I_L v_s^4 \sum_{\rho\sigma} \left|\left(\alpha_{\rho\sigma}\right)_{G\to F}\right|^2 \qquad (1)$$

In this equation, I_L is the intensity of the laser and v_s is the frequency of the Raman-scattered photons. The molecular polarizability tensor is represented by $(\alpha_{\rho\sigma})_{G\to F}$, where ρ and σ represent incident and scattered polarizations, respectively. The expression for $(\alpha_{\rho\sigma})_{G\to F}$ is,

$$\left(\alpha_{\rho\sigma}\right)_{G\to F} = \frac{1}{hc}\sum_{E}\left[\frac{\langle F|\hat{\mu}_\rho|E\rangle\langle E|\hat{\mu}_\sigma|G\rangle}{v_{GE} - v_L + i\Gamma_E} + \frac{\langle F|\hat{\mu}_\sigma|E\rangle\langle E|\hat{\mu}_\rho|G\rangle}{v_{GE} + v_L + i\Gamma_E}\right] \qquad (2)$$

The excited intermediate state is represented by E and $\hat{\mu}$ is the electric dipole moment operator. The damping factor is represented by Γ_E, which is the natural half-width of the

5
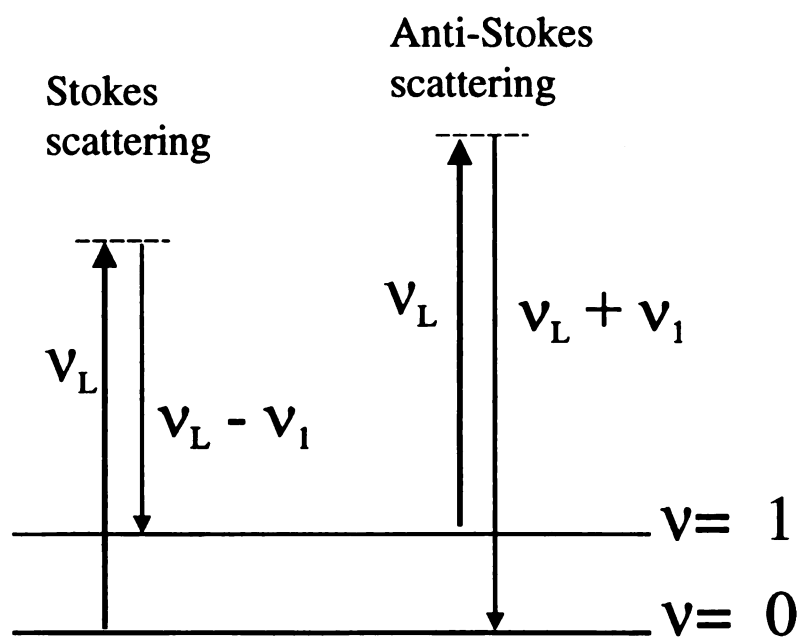
Figure 1.1. Schematic representation of the Stokes and anti-Stokes scattering (adapted from Nakamoto (3)).

state E. Planck's constant and the velocity of the light are denoted in the equation by h

and c, respectively. The summation is over all possible electronic states E. At resonance,

$v_{GE} \cong v_L$, and the first term in equation 2 becomes more important than the second term.

Thus, at resonance, equation 2 can be written as:

$$\left(\alpha_{\rho\sigma}\right)_{G\to F} \approx \frac{1}{hc}\sum_E \frac{\langle F|\hat{\mu}_\rho|E\rangle\langle E|\hat{\mu}_\sigma|G\rangle}{v_{GE} - v_L + i\Gamma_E} \tag{3}$$

Application of the Born-Oppenheimer approximation to equation 3 results in the

separation of the nuclear and electronic wavefunctions. Now the ground state G is

represented by the ground electronic state, g, and it vibrational state, u. The excited state

E is represented by the excited electronic state, e, and its vibrational state, v. The final

state F is now represented by the electronic wavefunction g, and vibrational

wavefunction, w. The Raman process is shown schematically in Figure 1.2. Now

equation 3 can be written in the form,

$$\left(\alpha_{\rho\sigma}\right)_{u\to w} = \frac{1}{hc}\sum_e \sum_v \frac{\langle gw|\hat{\mu}_\rho|ev\rangle\langle ev|\hat{\mu}_\sigma|gu\rangle}{\Delta v + i\Gamma} \tag{4}$$

Where $v_{ge} - v_L$ has been substituted with Δv. The advantage of equation 4 is that the sum

now includes the vibrational states. The electronic part can be factored out of equation 4,

because the electric dipole moment is $M_{eg} = \langle g|\hat{\mu}_\rho|e\rangle = \langle e|\hat{\mu}_\sigma|g\rangle$, thus the polarizability

tensor is now in the form of

$$\left(\alpha_{\rho\sigma}\right)_{u\to w} \approx \frac{1}{hc}M_{eg}^2\sum_v \frac{\langle w_g|v_e\rangle\langle v_e|u_g\rangle}{\Delta v + i\Gamma} \tag{5}$$

7
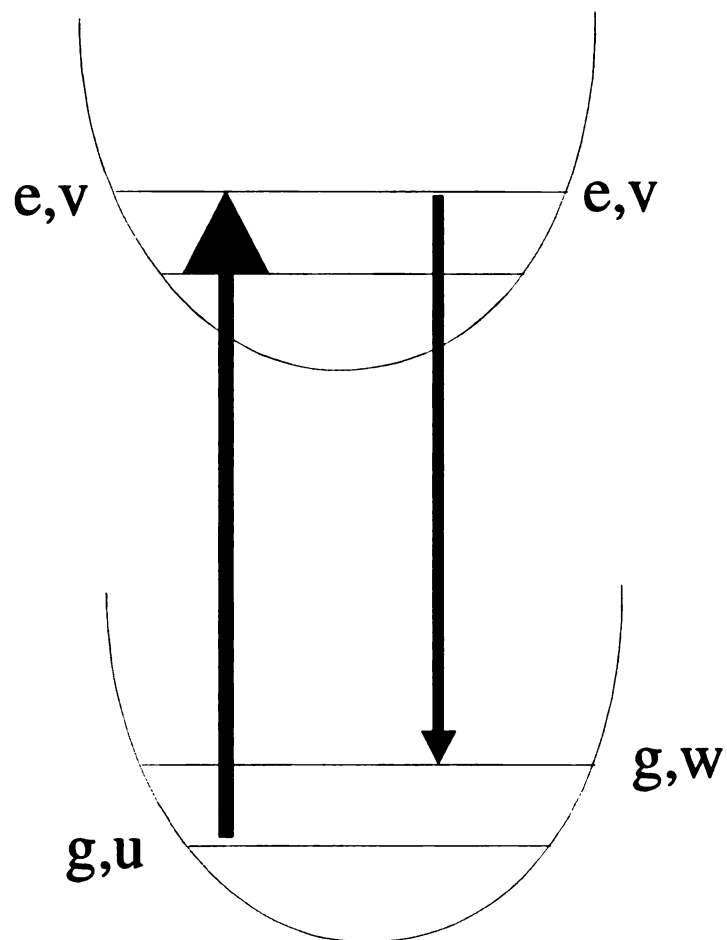
Figure 1.2. Schematic representation of the resonance Raman process. The figure

depicts how the system goes through the different electronic and vibrational levels during

the Raman scattering. The electronic manifolds are denoted by g and e, while the

vibrational levels are u, v, and w.

Equation 5 shows the dependence of the polarizability tensor on the Franck-Condon factors. This equation only shows the A-term, which for now will be more important than the B- and C- terms. These terms are described elsewhere (2,4,5). Since the square of the electronic dipole moment is proportional to the extinction coefficient ϵ, $M_{eg}^2 \propto \epsilon(v)$ and the intensity of the resonance Raman scattering is proportional to the square of the extinction coefficient of the molecular system: $I_S \propto \epsilon(v)^2$.

Hemes absorb strongly in the UV and visible regions of the electromagnetic spectrum (see Figure 1.3 for an example of a typical UV-Vis spectrum of a heme); thus, the resonance Raman technique is suitable for the application to heme proteins. The heme proteins exhibit a strong absorption band ($\epsilon \sim 100,000 \ M^{-1}cm^{-1}$) near the UV called the Soret band (see Figure 1.3). By tuning the laser frequency to match the λ_{max} of the Soret band, the Raman scattering will be greatly enhanced and it will give vibrational information only about the heme macrocycle.

In the next section, a brief description will be given about the information that is obtained with the application of the resonance Raman technique to heme proteins and model compounds.

1.3 The resonance Raman spectrum of a heme protein

The resonance Raman spectrum of a heme protein contains useful information in the 150 to 2000 cm^{-1} region. The three types of vibrational modes that are normally reported are: iron-ligand modes; vibrations related to the peripheral subsistent groups in
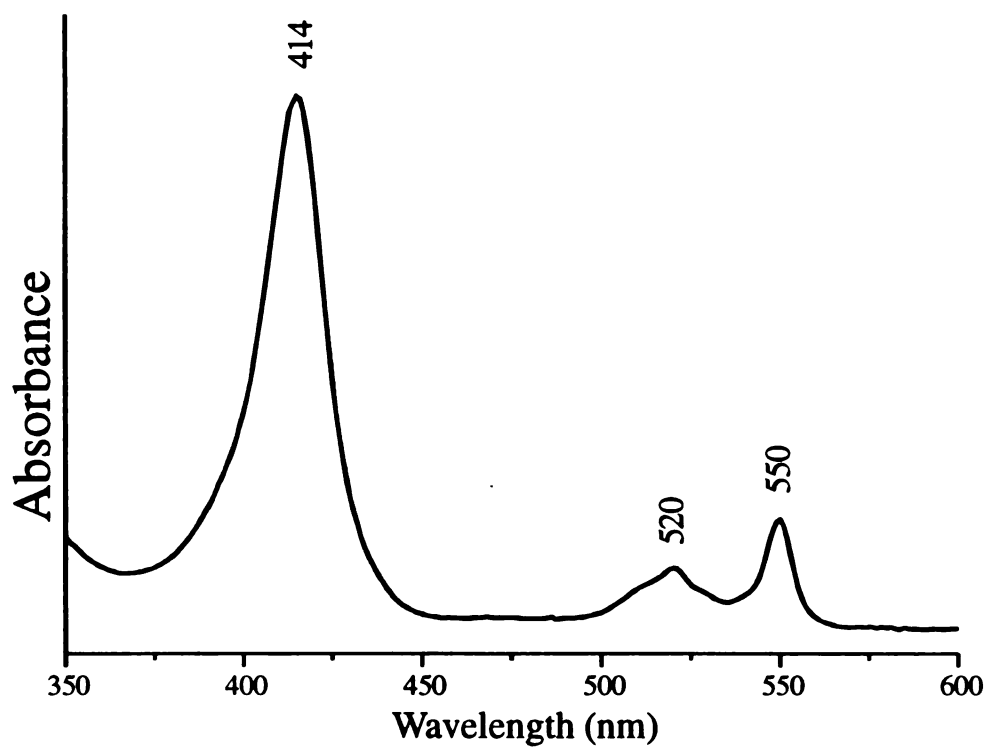
Figure 1.3. UV-Vis absorption spectrum of ferrous cytochrome c. The strong band at

414 nm is the Soret band, characteristic of heme proteins. The smaller bands in the

visible region are known as the Q bands.

the porphyrin macrocycle, e.g., propionate, vinyl and formyl groups in heme a; and modes that are sensitive to the heme iron, known as the "core size marker bands" (5). Most of these types of modes are found in two regions of the resonance Raman spectrum, the low and high frequency regions, which comprise the 150 to 700 cm^{-1}, and 1300 to 1700 cm^{-1} regions, respectively. The intermediate region from ~ 700 to 1200 cm^{-1} is particularly rich in vibrations that are from the iron-oxo stretching modes (Fe^{4+}=O) in oxo ferryl hemes and O-O stretching modes from dioxygen- and peroxy-bound iron heme complexes (6). Iron-ligand modes from other ligand-bound iron complexes are located in the low frequency region (7,8), see Figure 1.3-a. The modes that denote the oxidation, spin and coordination states ("core size marker bands") of the heme iron are found in the high frequency region (Figure 1.3-b) (5).

1.3.1 Iron-ligand modes

The resonance Raman spectra of ferrous, five coordinate, heme proteins exhibit iron-ligand vibrations that are due to the covalent bond between the heme iron and the proximal ligand (7). Most of the heme proteins have a cysteine, tyrosine, or a histidine as the amino acid that provides the covalent link between the heme iron and the protein. Histidine is the preferred proximal ligand, as it is found in the majority of the heme proteins. The iron-N_{his} stretching modes of heme proteins with proximal histidine ligand occur in the 200 to 250 cm^{-1} region (7). Figure 2a shows an example of a Raman spectrum of a ferrous heme protein, soluble guanylate cyclase (sGC), reported by Schelvis et al. (9). This protein has an $v(Fe-N_{his})$ stretching vibration at 206 cm^{-1}, which is a low value for typical heme proteins (7). Oxygen-carrier heme proteins, e.g.,

myoglobin and hemoglobin, have iron-his vibrations in the 210 to 225 cm^{-1} region. On

the other hand, heme protein peroxidases tend to have higher frequency $v(Fe-N_{his})$

vibrations around 240 cm^{-1}. The basis for a ~20 cm^{-1} difference in the Fe-N$_{his}$ stretching

modes between oxygen carriers and peroxidase heme proteins will be discussed later.

Although resonance Raman spectroscopy is a technique for which the strength of the

proximal ligand can be monitored, i.e., the basicity of the ligand, this can only be

observed when the heme iron is ferrous, five coordinate. Thus, the iron-N$_{his}$ stretching

mode is inactive when the heme iron is either 6-coordinate or in its ferric oxidation state

(7). This behavior is not well understood and may be related to the symmetry of the

heme (10), which is D$_{4h}$ when the iron is in the heme plane. This symmetry is broken

when the iron is displaced from the heme plane (e.g. ferrous high-spin state heme

compounds). Stavrov (11) used vibronic theory to show that the iron displacement out of

the plane of porphyrin nitrogens plays a crucial role in mixing the $\sigma(Fe-N_{his})$ molecular

orbital (MO) to the $\pi(a_{2u})$ MO of the heme. In his view, the Fe-N$_{his}$ mode should gain

more activity during Soret excitation, as the iron is more displaced from the heme plane.

While the resonance Raman spectra of ferrous 5-coordinate heme proteins contain

useful information about their proximal ligand, the frequencies of the $v(Fe-CO)$ and

$v(CO)$ stretching modes from carbon monoxy-bound heme proteins can give us an idea

on the interactions between the distal side and the ligand site of the protein. The iron-CO

vibrations are commonly located in the 480 to 540 cm^{-1} region of the resonance Raman

spectra (8). An example is shown for ferrous-CO sGC in Figure 1.3-a, in which the $v(Fe-$

CO) is at 478 cm^{-1}. The $v(CO)$ stretching mode of the Fe-CO unit is found in the 2000 to

12

a)

his

C=O

side view

ferrous-CO

478 v(Fe-CO)

v(Fe-N$_{his}$)
206

ferrous

200 300 400 500 600 700 800

b)

N   N
   Fe
N   N

spin, redox,
coordination

ferrous-CO

ferrous

1100 1200 1300 1400 1500 1600 1700
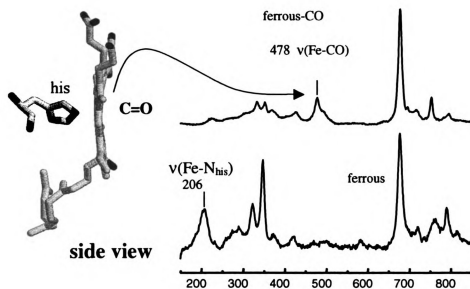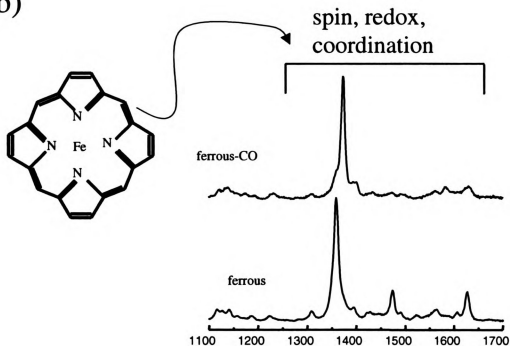
Figure 1.4. Typical resonance Raman spectra of heme proteins. The low frequency region is shown in a), while the high frequency region is shown in b) (adapted from (9)).

2050 cm^{-1} region, but it is a much weaker mode than that of v(Fe-CO) (12). The CO

molecule is a π-acid ligand that can accept electron donation from the d_π iron orbital to its

π^* MO orbital. Hence, an inverse correlation exists between the v(Fe-CO) and the v(CO)

stretching modes of CO-bound heme compounds. Figure 1.5 displays the v(Fe-CO) vs.

v(CO) frequencies for various heme proteins and model compounds obtained from Lou *et*

al. (13). These are grouped according to the basicity of the proximal ligand (8). The CO-

bound heme proteins and model compounds with proximal cysteines and thiolate ligands

are in a correlation curve below that of the corresponding complexes with proximal

histidines or imidazole ligands. This is because of the stronger basicity of the thiolate

over the imidazole ligand. In this case, the heme compounds with a proximal thiolate

ligand have decreased σ-donation from the coordinated CO, because of the stronger σ

bond between the iron and the thiolate ligand. This results in a lower v(Fe-CO) vibration

for hemes with proximal thiolate ligands than those of the corresponding compounds that

have a *trans*-imidazole ligands. CO-bound heme compounds that have no proximal

ligands or 5 coordinate CO-heme complexes are located further above the correlation

curve for heme proteins with proximal histidines. The v(Fe-CO) and v(CO) frequency

values can be used to identify the proximal ligand, in cases for which the frequency of the

Fe-ligand$_{proximal}$ is not discernable. Normally, if the vibration is not obvious the

assignment must be done by using isotopes. For this, the heme iron needs to be

substituted with ^{57}Fe or ^{54}Fe, which only produce a 1 to 2 cm^{-1} shifts (7). An easier

alternative is to measure the resonance Raman spectra of the CO-bound heme protein for

normal abundance and isotopically enriched CO. The CO isotopes are easier to use

because of the 6 to 10 cm^{-1} shifts that are produced by the ^{13}C^{16}O and ^{13}C^{18}O isotopes,

respectively. Once the ν(Fe-CO) and ν(CO) frequency values have been obtained, the

heme protein can be placed on a particular correlation curve, which is characterized by

the type of proximal ligand. This method is rarely used for heme proteins with proximal

histidine ligands, however, as will be discussed in Chapter III, the ν(Fe-CO) and ν(CO)

correlation turned out to be a very convincing indication of the weak proximal ligand in

PGHS-1 (14).

Within a particular correlation curve, the ν(CO) frequency depends on the

interaction between the distal pocket and the CO-bound heme ligand (15). In this case,

the polarity of the pocket increases the π-back donation from the Fe (d_π) to the CO (π^*)

orbital, which increases the π-bonding of the Fe-C bond and decreases the order of the

CO bond. The CO-bound heme proteins with a proximal histidine that have a polar distal

side are found at the higher end of the correlation curve (15). Most heme peroxidases,

myoglobins, and hemoglobins have a distal histidine at about 5 Å from the heme iron and

can form hydrogen bonding to the coordinated CO ligand (16). This hydrogen bonding

increases π-backbonding between the iron and the CO molecule. Such heme proteins

have vibrations from 507 to 530 cm^{-1} for the ν(Fe-CO) stretching modes and ν(CO)

frequencies from 1910 to 1950 cm^{-1} (15). Meanwhile, heme model compounds, which

lack the protein environment, have higher ν(CO) values and lower ν(Fe-CO) frequencies

than those of heme proteins and are found at the lower end of the correlation curve for

proteins with proximal imidazole ligands (8).

hemes with proximal histidine, imidazole ligands

heme with a weak proximal ligand or no ligand

hemes with proximal Cys, S-, ligand
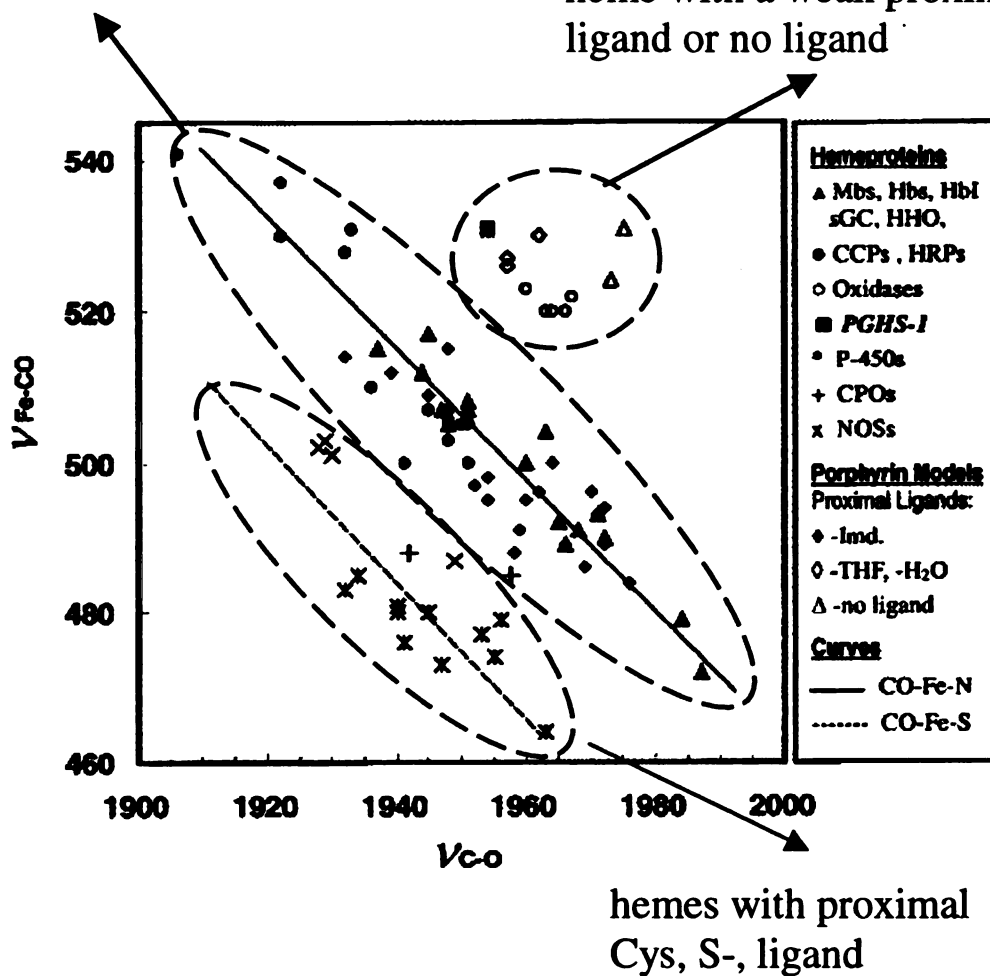
Figure 1.5. The v(Fe-CO) vs. (C=O) correlation curve for heme proteins and model compounds (adapted from Lou *et al.* (13)).

16

The ligand and iron-ligand modes from O_2-bound heme proteins in oxygen

carriers can give information on how O_2 is stabilized in hemoglobins and myoglobins.

The intensity of the $v(Fe-O_2)$ stretching vibration is relatively weaker than the $v(Fe-CO)$

modes in heme proteins. Moreover, the $v(O=O)$ stretching modes of most of the

dioxygen-bound hemoglobins and myoglobins are resonance Raman inactive and can

only be detected by IR spectroscopy (8). When the iron is substituted with cobalt in

hemoglobin, the $v(O=O)$ mode is detected around 1134 cm^{-1}; this vibration is very close

to that of the superoxy ligand in metal-O_2^- complexes (17). This value has been

confirmed recently for O_2-bound heme iron hemoglobins from *Chlamydomonas* and

Synechocystis (17).

The $v(Fe-O_2)$ stretching modes of oxy hemoglobin and myoglobins are normally

detected from 565 to 573 cm^{-1} region of the resonance Raman spectra (8). Similar to the

$v(Fe-CO)$ stretching modes and $v(CO)$ frequencies in CO-bound heme compounds, the

$v(Fe-O_2)$ and $v(O=O)$ stretching modes from dioxygen-bound heme complexes exhibit a

linear inverse correlation due also to π-backbonding. However, these are less

documented because of the difficulty in detecting the $v(O=O)$ stretching modes. The

$v(Fe-O_2)$ stretching modes of dioxygen-bound heme peroxidases have values lower than

hemoglobins and myoglobins, ~560 cm^{-1} (18). According to Oertling *et al.* (18), this

difference in frequencies between the peroxidases and the oxygen-carriers can be

attributed to distinct distal side effects on the coordinated O_2 ligand. The distal sides of

peroxidases normally tend to have a histidine-arginine couple that assists in O-O splitting

of the coordinated peroxide. While the histidine acts as an acid-base residue, the

positively charged arginine removes electron density from the O-O unit of the bound

peroxide; this positively charged arginine is absent in oxygen-carrier proteins. When O_2

coordinates to the heme in a peroxidase, the removal of electron density results in an

increase in the bond order of the O=O bond, while the Fe-O bond experiences a decrease

in its strength. The opposite mode of action is observed in myoglobin, where the O_2-

bound ligand is stabilized by increased π-backbonding from the iron to the O_2 π^* orbital,

caused by hydrogen bonding from the proximal histidine (18).

The ferryl-oxo heme intermediates that are formed during O_2 and peroxide

catalysis have $v(Fe^{4+}=O)$ stretching modes in the 750 to 850 cm^{-1} region of the Raman

spectrum (6,18-20). The $v(Fe^{4+}=O)$ modes of ferryl-oxo heme model compounds are

affected by the *trans*-ligand; strong electron-donating ligands lessen the σ and π

donations from the oxo ligand to the heme iron. In contrast to the dioxygen, the oxo

ligand is both a σ and π donor, hence the $v(Fe^{4+}=O)$ and $v(Fe-O_2)$ modes may be affected

differently (18). One major disadvantage in studying ferryl-oxo heme intermediates and

model compounds is that they are unstable, especially when subjected to laser exposure

during the Raman measurements (21). In addition, changes in the value of the $v(Fe^{4+}=O)$

stretching mode does not hint to whether it may be caused by changes in the interactions

from the distal or the proximal side of the protein. More specifically, the $Fe^{4+}=O$ and Fe-

N_{his} bond strengths cannot be measured simultaneously with resonance Raman because

the $v(Fe-N_{his})$ mode is not active in six coordinate hemes, as was explained before in this

section. The approach that is normally taken, is to assume that the Fe-N_{his} bond strength,

deduced from the $v(Fe-N_{his})$ mode in the ferrous five-coordinate state, is only affected by

the oxidation state of the heme iron. With this assumption, the different $v(Fe^{4+}=O)$

frequencies among various heme proteins and model compounds can be explained in

terms of the differences in the $v(Fe-N_{his/imidazole})$ mode (21). Oertling *et al.* (21) showed a

correlation between the $v(Fe^{4+}=O)$ frequencies and the $v(Fe-N_{his/imidazole})$ stretching modes

of the corresponding compounds in their respective ferrous 5-coordinate state. The

$v(Fe^{4+}=O)$ and $v(Fe-N_{his/imidazole})$ modes have a negative linear correlation due to the σ

and π donor properties of the oxo ligand. For example, myoglobin has a lower $v(Fe-N_{his})$

stretching mode than horse radish peroxidase (HRP), however, the ferryl-oxo adduct of

myoglobin has a higher $v(Fe^{4+}=O)$ mode than that of the ferryl-oxo HRP-compound II,

797 and 775 cm^{-1}, respectively (21).

The effects of the distal side on the oxo-bound ligand of the ferryl-oxo heme

protein should be less pronounced than effects on the dioxygen-bound ligand of ferrous-

oxy heme, because the Fe-O bond is shorter than the Fe-O$_2$. Therefore, the chemical

control of the ferryl-oxo adducts in heme proteins is mainly dictated by the proximal

effects. In this respect, there is a strong hydrogen bond between a nearby aspartate and

the proximal histidine in heme peroxidases. The oxygen-carrier heme proteins lack this

strong hydrogen bond to the proximal histidine, as there are no nearby aspartate residues.

This is the reason that the $v(Fe-N_{his})$ modes in peroxidases are 20 cm^{-1} higher than the

$v(Fe-N_{his})$ modes in myoglobin (7); this will be discussed in details in Chapter III because

of its relevance to the peroxidase activity PGHS-1. Whether this strong hydrogen bond

between the conserved aspartate and the proximal histidine in peroxidases plays a role in

O-O splitting or in the stabilization of the ferryl-oxo intermediate will later be discussed

in Chapter III. The distal side can also have an effect on the oxo ferryl compound, but

through interactions that cause changes in the proximal side of the heme protein and thus

affect the ferryl-oxo unit of the protein. This effect has been observed in HRP, for which

the protonation of the distal histidine causes a 3 cm^{-1} shift in the v(Fe-N$_{his}$)(7,22); the pKa

of this effect is ~ 7.5. The v(Fe^{4+}=O) mode in HRP is also affected by the pH and has a

similar pKa as the v(Fe-N$_{his}$) mode, therefore the implications of indirect distal side

effects on the ferryl-oxo adduct of HRP (7).

1.3.2 The core size marker bands

The size of the Fe ion has an effect on the skeletal structure of the porphyrin ring;

this in turns, affects the vibrational modes of the heme macrocycle (5). The high

frequency region of the Raman spectrum contains various vibrations that are from the

skeletal modes of the porphyrin ring. Some of the most important modes in this region

are shown for the different heme adducts of hemoglobin I from *Lucina pectinata* (23),

shown in Figure 1.6. These modes are v_2, v_3, v_4, and v_{10}, which are all sensitive to the

type of heme complex. As the ionic radius of the iron decreases, the frequency values of

all of these modes increase (5). To understand this behavior, Figure 1.7 shows a

porphyrin ring with some of the in-plane skeletal Raman modes with their respective

major coordinate of vibrations, based on the assingments made for Ni^{2+}-

octaethylporphyrin complex (5,24,25). When the heme iron is in the ferrous high-spin

state, the iron becomes displaced from the heme plane because it is too large to fit in the

core of the porphyrin ring; this causes elongation of the bonds in the skeletal domed

structure. On the other hand, when in the ferric low-spin state, the size of the iron ion

will be smaller and the bonds will be shorter. In this case, the iron will be in the same

plane as the heme, as it will now fit in the core of the ring. Thus, the greatest frequency

shifts in these modes will be experienced when the heme iron changes from the ferrous

high-spin state to ferric low-spin state. In between these two extremes, there are various gradations in the size of the heme core, which are produced by the combination of the different spin, oxidation, and coordination states of the iron.

Among the high frequency "core size makers", modes v_3 and v_{10} are the most sensitive to the size of the heme iron ion (5). These have different values for each distinct combination of oxidation, spin and coordination states. This is because they are the most sensitive to the different sizes of the heme iron. The major coordinate of vibration for these modes is the C_a-C_m bond (24). Figure 1.6 shows the different frequency values of modes v_3 and v_{10} for the different heme compounds of HbI according to the assignments made by Silfa et al. (23). The deoxy Hb, is a ferrous high-spin heme and have v_3 and v_{10} values at 1468 and 1606 cm^{-1}, respectively. Mode v_3 shifts to 1484 cm^{-1} in the ferric-aquo complex (Hb-H$_2$O), while mode v_{10} (not shown) shifts to the 1617 cm^{-1} region, which is overlapped by the strong $v(C=C)$ stretching modes from the vinyls at 1622 cm^{-1} (23). The CO-bound ferrous hemoglobin (HbI-CO), is a six-coordinate low-spin complex, which have frequencies at 1498 and 1620 cm^{-1} (not shown) for modes v_3 and v_{10}, respectively. When the heme iron is ferric, six-coordinate low-spin in the CN-bound Hb, modes v_3 and v_{10} have their respective highest values at 1506 and 1640 cm^{-1}, respectively. Mode v_2 is the less sensitive to the size of the heme iron, because its major coordinate of vibration, the C_b-C_b bond in the pyrrole ring, does not deform to the same extent as the C_a-C_m bond when there are changes in the core of the porphyrin (5). The frequency of this mode is only indicative of the spin state of the heme iron. Thus, Figure 1.6 shows that among the different heme complexes, this mode has two types of frequencies, at 1561 and 1582 cm^{-1}, for high- and low-spin state iron, respectively. The

redox state of the iron has an effect on the nitrogens from the pyrrole ring of the heme (5). This oxidation change affects mode v_4 because the major coordinate of the vibration is the C_a-N bond. This mode is at 1355 cm^{-1} for the ferrous deoxy form of the heme in Figure 1.6 and at 1376 cm^{-1} for the ferric low-spin metCN adduct. Interestingly, the ferrous-CO complex has a vibration at 1376 cm^{-1}, which is at the same frequency of the ferric-CN complex. This is because CO is a π-acid ligand that competes with the nitrogens, which are part of the π^* orbital of the porphyrin, for the electrons in Fe(d_π) orbital (5). Removal of electron density from π^* MO increases the order of the C_a-N bond. This is the reason that O_2-bound heme compounds also have v_4 frequencies in the 1376 cm^{-1} region, as will be seen for the ferrous-oxy CcO intermediate (Chapter II).
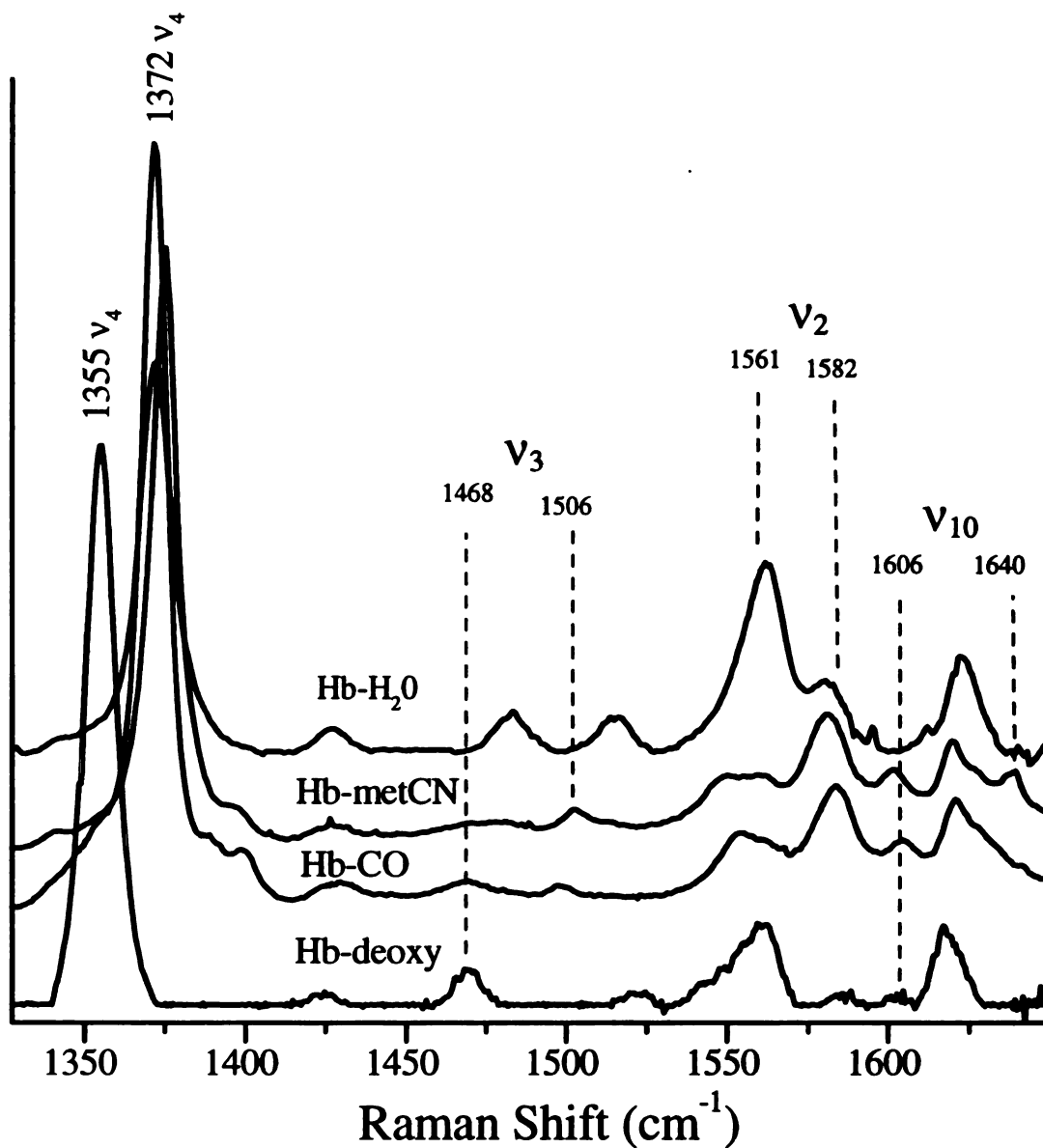
Figure 1.6. High frequency region of the resonance Raman spectra of various heme derivative of HbI from *L. pectinata*. This region shows some of the modes that are core size markers (adapted from reference (23)).
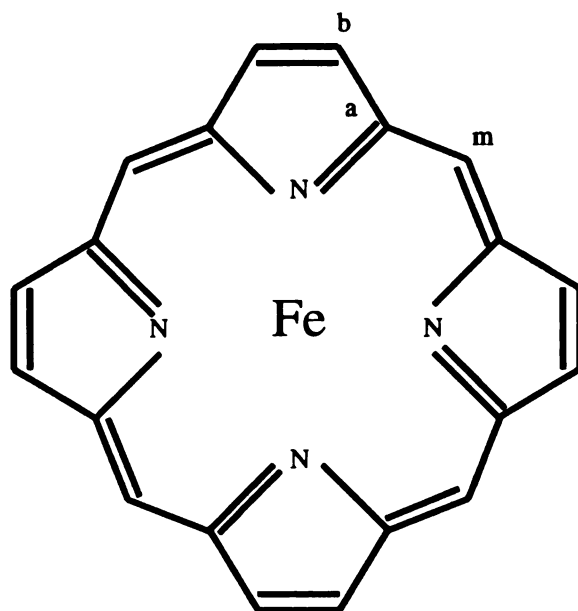
$$\nu_2 \rightarrow \nu(C_b\text{-}C_b)$$

$$\nu_3 \rightarrow \nu(C_a\text{-}C_m)$$

$$\nu_4 \rightarrow \nu(C_a\text{-}N)$$

$$\nu_{10} \rightarrow \nu(Ca\text{-}C_m)$$

Figure 1.7. The heme macrocyle with some of the core size maker modes and their respective major coordinate of vibration according to Spiro (5).

1.4 Literature Cited

1. Dietz, R., Nastainczyk, W., and Ruf, H. H. (1988) *Eur. J. Biochem.* **171**, 321-328.

2. Rousseau, D. L., Friedman, J. M., and Williams, P. F. (1979) in *Raman Spectroscopy of Gases and Liquids* (Weber, A., ed) Vol. 11, pp. 203-252, Springer-Verlag.

3. Nakamoto, K. (1997) *Infrared and Raman spectra of inorganic and coordination compounds / Kazuo Nakamoto.*, 5th ed. Ed., A, John Wiley & Sons, Inc..

4. Asher, S. A. (1988) *Annu. Rev. Phys. Chem.* **39**, 537-588.

5. Spiro, T. G., and Li, X.-Y. (1988) in *Biological Applications of Raman Spectroscopy* (Spiro, T. G., ed) Vol. 3, pp. 1-38, 3 vols., John Wiley & Sons.

6. Kitagawa, T., and Mizutani, Y. (1994) *Coord. Chem. Rev.* **135**, 685-735.

7. Kitagawa, T. (1988) in *Biologial Applications of Raman Spectroscopy* (Spiro, T. G., ed) Vol. 3, pp. 97-132, 3 vols., John Wiley & Sons.

8. Kerr, E. A., and Yu, N. T. (1988) in *Biological Applications of Raman Spectroscopy* (Spiro, T. G., ed) Vol. 3, pp. 39-96, 3 vols., John Wiley & Sons.

9. Schelvis, J. P. M., Zhao, Y., Marletta, M. A., and Babcock, G. T. (1998) *Biochemistry* **37**, 16289-16297.

10. Champion, P. M. (1988) in *Biological Application of Raman Spectroscopy* (Spiro, T. G., ed) Vol. 3, pp. 249-292, 3 vols., Wiley & Sons.

11. Stavrov, S. S. (1993) *Biophys. J.* **65**, 1942-1950.

12. Wang, J. L., Takahashi, S., and Rousseau, D. L. (1995) *Proc. Natl. Acad. Sci. U. S. A.* **92**, 9402-9406.

13. Lou, B. S., Snyder, J. K., Marshall, P., Wang, J. S., Wu, G., Kulmacz, R. J., Tsai, A. L., and Wang, J. (2000) *Biochemistry* **39**, 12424-12434..

14. Seibold, S. A., Cerda, J. F., Mulichak, A. M., Song, I. S., Garavito, R. M., Arakawa, T., Smith, W. L., and Babcock, G. T. (2000) *Biochemistry* **39**, 6616-6624.

15. Ray, G. B., Li, X. Y., Ibers, J. A., Sessler, J. L., and Spiro, T. G. (1994) *J. Am. Chem. Soc.* **116**, 162-176.

16. Smulevich, G., Evangelista-Kirkup, R., English, A., and Spiro, T. G. (1986) *Biochemistry* **25**, 4426-4430.

17. Das, T. K., Couture, M., Ouellet, Y., Guertin, M., and Rousseau, D. L. (2001) *Proc. Natl. Acad. Sci. U. S. A.* **98**, 479-484.

18. Oertling, W. A., Kean, R. T., Wever, R., and Babcock, G. T. (1990) *Inorg. Chem.* **29**, 2633-2645.

19. Sitter, A. J., Reczek, C. M., and Terner, J. (1985) *Biochim Biophys Acta* **828**, 229-235.

20. Varotsis, C., and Babcock, G. T. (1990) *Biochemistry* **29**, 7357-7362..

21. Oertling, W. A., and Babcock, G. T. (1988) *Biochemistry* **27**, 3331-3338..

22. Mukai, M., Nagano, S., Tanaka, M., Ishimori, K., Morishima, I., Ogura, T., Watanabe, Y., and Kitagawa, T. (1997) *J. Am. Chem. Soc.* **119**, 1758-1766.

23. Silfa, E., Almeida, M., Cerda, J., Wu, S. X., and Lopez-Garriga, J. (1998) *Biospectroscopy* **4**, 311-326.

24. Kitagawa, T., Abe, M., and Ogoshi, H. (1978) *J. Chem. Phys.* **69**, 4516-4525.

25. Abe, M., Kitagawa, T., and Kyogoku, Y. (1978) *J. Chem. Phys.* **69**, 4526-4534.

Chapter II: Detection of Intermediates in the Reaction of Cytochrome c oxidase

2.1 Introduction

Cytochrome c oxidase (CcO) is the last enzyme in the electron transport chain located in the inner membrane of the mitochondria. CcO reduces O_2 to H_2O and uses the energy released during this process to drive protons across the membrane. More specifically, CcO catalyzes the following reaction,

$$O_2 + 4e^- + 8H^+ \text{ (in)} \rightarrow 2H_2O + 4H^+ \text{ (out)}$$
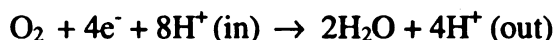
The proton gradient that is formed during O_2 reduction is then used for the formation of adenosine triphosphate (ATP), the molecule that provides the energy to a wide range of metabolic processes. The mechanism by which proton pumping is controlled by dioxygen reduction in CcO is important for the understanding of energy transduction in enzymes, certainly a valuable contribution to the field of bioenergetics. Most of the structural details of the catalytic intermediates that are formed during the reaction between CcO and O_2 have come from resonance Raman spectroscopic studies. This work will later be described in detail, but first, the static structure and the changes that CcO undergoes during O_2 reduction will be discussed in terms of the X-ray crystallographic and optical absorption studies.

2.1.1 The redox metal cofactors and their spatial arrangements in CcO

The mammalian bovine heart CcO is a molecule with a weight of over 200 KDa that comprises 13 subunits; two of these, subunits I and II, contain the four redox metal centers: Cu_A, heme a, heme a_3 and Cu_B. The metal cofactors Cu_A and heme a only

27

participate in electron transfer, while heme a_3 and Cu_B are involved in O_2 binding and reduction. There is also a third important subunit (III) that provides a hydrophobic entry port for dioxygen and leads to the active site of CcO. The proton, electron, and O_2 routes, along key metal centers, are depicted in Figure 2.1.

The relative location of the pieces that form the proton-pumping machinery was first figured out by using various spectroscopic methods and later confirmed, with more details, by X-ray crystallographic data from bovine (1,2) and bacterial (3) CcO. The X-ray crystallographic structure showed that hemes a and a_3 are located at the same depth within CcO, 13 Å from the surface of the membrane. The heme planes are almost perpendicular to each other, with an edge-to-edge and iron-to-iron distances of ~7 and 14 Å, respectively. The Cu_A site is composed of a binuclear copper center, located at 19 Å from heme a and 22 Å from heme a_3; this redox center is the first one to accept the electrons from cytochrome c during O_2 catalysis.

The O_2 binding site is the a_3 -Cu_B binuclear center, in which the copper-to-iron distance is 5.2 Å in bovine heart CcO in its resting state (oxidized). Figure 2.2 shows the X-ray crystallographic structure of the binuclear center of CcO from *R. sphaeroides* (4). In this figure, two of the three histidines that are coordinated to Cu_B are not shown; the importance of histidine 284 (H284, H240 in beef heart enzyme), shown in Figure 2.2, is that is a crossed-link to tyrosine 240 (Y240, Y244 in bovine heart). The role of this cross-link has not yet been established, although it was shown that the crossed-link tyrosine 244 is oxidized during O_2 catalysis in bovine heart CcO (5). The cross-link may induce changes in the chemical properties of the Tyr244, since it has been demonstrated
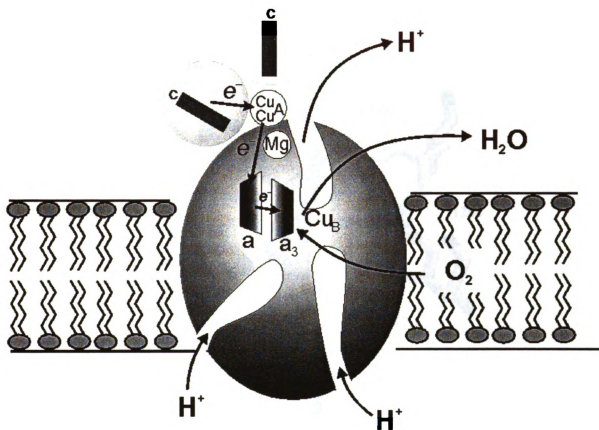
Figure 2.1. The electron, proton, and O_2 routes along with key metal centers in cytochrome c oxidase are shown in this schematic representation (courtesy of the Shelagh Ferguson-Miller lab from the Department of Biochemistry at Michigan State University).
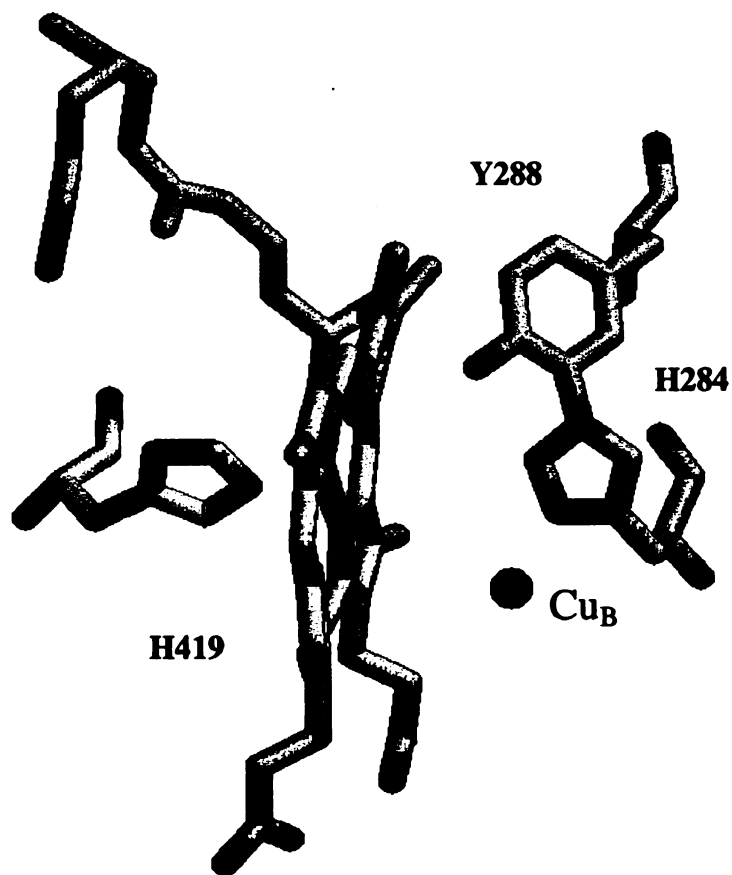
Figure 2.2. The X-ray crystallographic structure of the binuclear a_3-Cu_B center from *R.*

sphaeroides (4) shows that there is a covalent bond between histidine 284 (H284, H240

in beef heart enzyme) and tyrosine 240 (Y240, Y244 in bovine heart).

that the presence of a covalent link between the imidazole and the phenol rings changes the pKa of the phenol in model compounds that mimic the his-tyr link (6).

2.1.2 Intermediates in the reaction of CcO and O_2

The reaction between CcO and O_2 is extremely fast: it takes the enzyme about 3 ms to convert O_2 to H_2O. Hence, this reaction cannot be studied by conventional techniques such as the stopped-flow method. In order to avoid the relatively long times of the mixing techniques, Gibson and Greenwood devised a methodology in which CcO is inhibited with the photolabile carbon monoxide (CO) ligand and mixed with O_2-saturated buffer, then O_2 catalysis is initiated once the CO has been flashed off (7). The first intermediate that is formed during O_2 reduction is a dioxygen complex, termed Compound A and originally identified by Chance and colleagues (8). This intermediate is formed in the reaction of the fully reduced (the four metal centers are reduced) CcO as well as with the mixed-valence form (a_3 and Cu_B are reduced, while a and Cu_A are oxidized), however, its decay rate depends on the initial state of the enzyme. In the reaction of mixed-valence CcO, the rate of disappearance of Compound A is 5×10^3 s^{-1} (9). The next and last intermediate that is formed with the mixed-valence CcO is a compound termed P that has an absorption peak at 607 nm in the difference spectrum relative to the oxidized enzyme. Originally, it was believed that the structure of P was a peroxy intermediate with an intact O-O bond, however, resonance Raman spectroscopic studies showed that this bond is cleaved at this stage (9). The P notation is still maintained in the literature and in this chapter it will be referred to as P_m (P in mixed-valence reaction) and P_r (P in the fully reduced reaction).

The reaction of the fully reduced CcO and O_2 is more complex than that of the mixed-valence CcO because of the transfer of electrons between Cu_A and heme a, and between a and a_3, during O_2 reduction. The decay of Compound A in this reaction is 3 x 10^4 s^{-1} (10-12), 6 times faster than the decay rate in the reaction of mixed-valence CcO. This process is accompanied by the oxidation of heme a, where there is an electron transfer from $a \rightarrow a_3$ as Compound A disappears in the reaction of the fully reduced CcO. Various groups have observed that this electron transfer rate exhibits a kinetic isotope effect (KIE) of ~ 1.5 (13-15). The decay of Compound A in the mixed-valence reaction displays a KIE of ~ 1.9 and in both reactions the decay rate is pH-independent in the range of 6.5 to 9.0. Accordingly, this suggests that the disappearance of Compound A in both reactions is coupled to an internal proton transfer.

Whereas there is only one transition in reaction of the mixed-valence CcO (the A-to-P_m conversion), the reaction between the fully reduced CcO and O_2 produces various oxygen-containing intermediates before it reaches its final oxidized-resting state. Time-resolved optical absorption (TROA) spectroscopic study of the reaction between fully reduced CcO and O_2 showed that there are various kinetic phases that contain distinctly optical-absorbing species and which are designated as, in the order appearance during the reaction[†]: Compound A, Compound P, Compound F, and Compound H. There is a consensus that the valency of the enzyme in the A and H states are, $\{Cu_A^{+1}$ a^{+2} a_3^{2+}-O_2 $Cu_B^{1+}\}$ and $\{Cu_A^{+2}$ a^{+3} a_3^{3+}-OH $Cu_B^{2+}\}$, respectively. These catalytic intermediates are the first and last ones to be formed during catalysis with time constants of, $\tau = 10$ μs and 1.5 ms, respectively, at room temperature. At the oxo ferryl state (F) of the reaction, an

---

[†] in this thesis, intermediates Pm, Pr, F, and H, will also be denoted as Compound Pm, Compound Pr Compound F, and Compound H, respectively.

equilibrium is established between Cu_A and heme a: $\{Cu_A^{+1}\ a^{+3}\ a_3^{4+}=O\ Cu_B^{2+}\}$ and $\{Cu_A^{+2}\ a^{+2}\ a_3^{4+}=O\ Cu_B^{2+}\}$.

The assignment of the valency and structure of the enzyme at the "P" state in the mixed-valence and in the fully reduced CcO reaction has been controversial (as will be discussed in the next section). Although the EPR- trapping experiments and TROA spectroscopic studies were successful in detecting some of the transient compounds that are formed in both reactions, the time-resolved resonance Raman (TRRR) spectroscopy technique resolved the structural nature of most of these intermediates that are shown in the reaction cycles in Figure 2.3. Hence, in the next section, a summary of the most important findings in the TRRR field will be presented with some of the questions that still linger about Compound P and the O-O splitting[†] mechanism of CcO.

2.1.3 Structural details of the catalytic intermediates revealed by Raman spectroscopy

Babcock and co-workers were the first to use TRRR to show that the first intermediate, Compound A, produced in the reaction of fully reduced CcO, is a photolabile oxy-heme a_3 compound (16). Later on, detailed studies performed by various groups, in which O_2 isotopes were used for this reaction, it was shown that this intermediate exhibits a vibration at 570 cm^{-1} with $^{16}O_2$ that shifts to 545 cm^{-1} with $^{18}O_2$ (17-19). This vibration is identical to that of other dioxygen-containing heme protein moieties, e.g., oxy-myoglobin and -hemoglobin, and was therefore assigned to the $v(Fe^{2+}-O_2)$ stretching vibration of the ferrous-oxy heme a_3 complex of Compound A. Similarly,

---

[†] In this thesis, "O-O bond cleavage" and "O-O splitting" will be used indistinguishably.

R {a^{2+} Cu_A^{1+}}
a_3^{2+} Cu_B^{1+} O_2
$t \sim 20$ μs

4e⁻

{a^{3+} Cu_A^{2+}}

a_3^{3+}—OH Cu_B^{2+}
H

2e⁻

{a^{2+} Cu_A^{1+}}
a_3^{2+}O=O Cu_B^{1+}
A

$t \sim 1$ ms

H⁺

{a^{2+} Cu_A^{2+}}
{a^{3+} Cu_A^{1+}}

a_3^{4+}=O^{2-} Cu_B^{2+}
F

{a^{3+} Cu_A^{+1+}}
$t \sim 50$ μs
a_3^{4+}=O^{2-} Cu_B^{2+} + ⁻OH
P_r

H_2O
$t \sim 400$ μs   H⁺

R(MV)

O_2

a_3^{2+} Cu_B^{1+}

a_3^{2+}O=O Cu_B^{1+}
A

Tyr•
a_3^{4+}=O^{2-} Cu_B^{2+} + ⁻OH
P_m
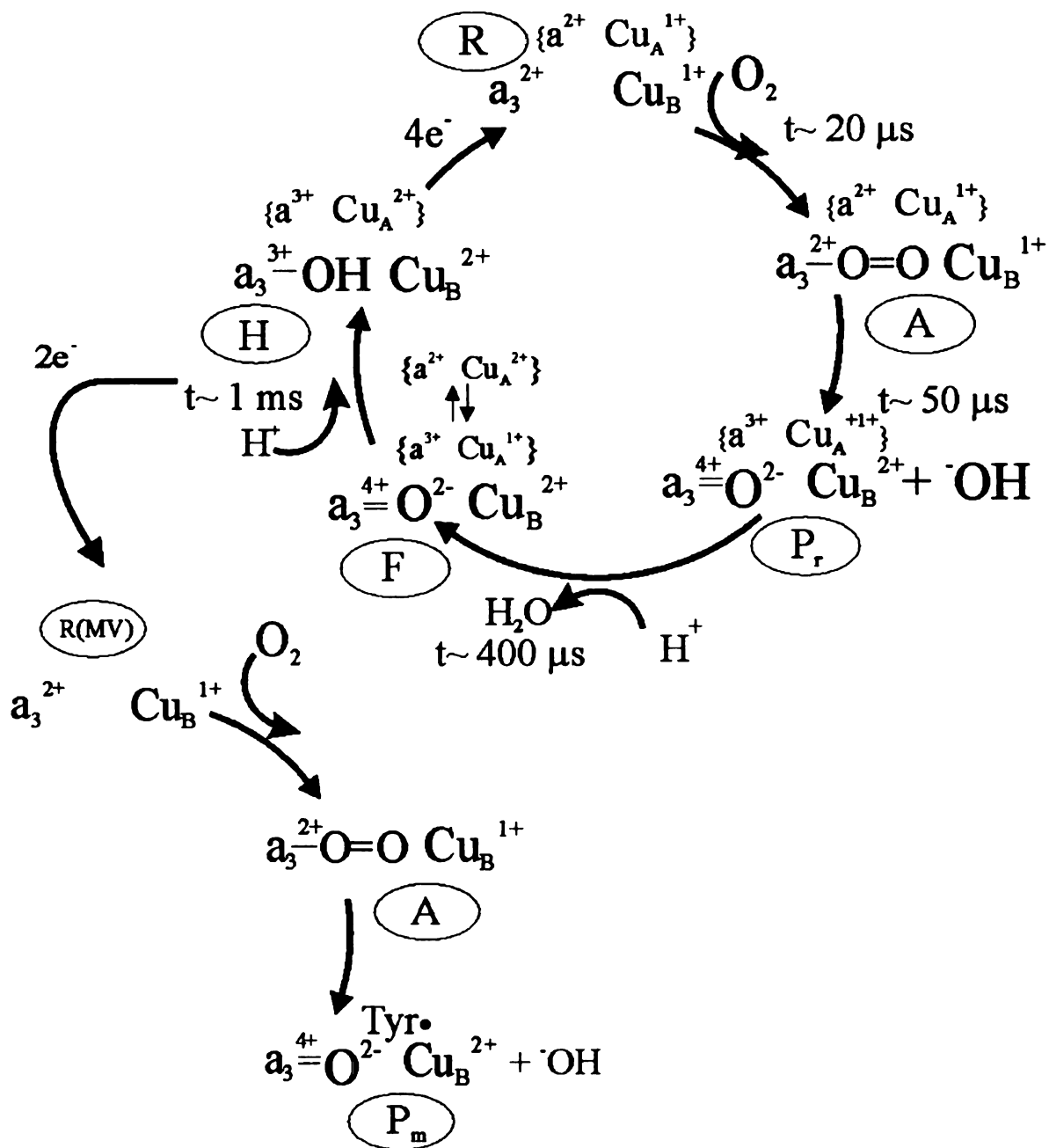
Figure 2.3. Schematic representation of the proposed intermediates that are formed during the reaction between CcO and O_2. The top catalytic cycle represents the reaction of the fully reduced CcO, while the bottom part of the figure shows the mixed-valence CcO reaction.

34

this vibration was also observed for the first intermediate in the reaction of mixed-valence CcO and was also designated also is Compound A (9,20,21). The next intermediate formed after Compound A in the mixed-valence CcO reaction is an intermediate with an optical absorption band at 607 nm in the difference spectrum relative to the resting enzyme. This same species can also be generated by the reaction between oxidized CcO and H_2O_2 and both compounds are known as "peroxy intermediates" (22). The 607-nm species, from the reaction of oxidized CcO and H_2O_2, displayed a vibration at 804 cm^{-1}, determined in an experiment in which the absorption and Raman spectra were measured simultaneously (23). This vibration shifted to 769 cm^{-1} when $H_2{}^{18}O_2$ was used for the reaction, therefore displaying an isotopic shift of 45 cm^{-1} which is typical for the $v(O-O)$ stretch of peroxide-bound iron complexes. Surprisingly this compound was found to not be a peroxy species, since the same experiment showed that the vibration was not affected by the mixed-isotope $H^{16}O^{18}OH$; thus, the 804 cm^{-1} mode of the 607-nm species was assigned to an $v(Fe^{4+}=O)$ ferryl-oxo stretching vibration. Analogously to the peroxide reaction, Raman measurements of the 607-nm species, Compound P_m, from the reaction of mixed-valence CcO and O_2, displayed an 804 cm^{-1} vibration that was also assigned to an $v(Fe^{4+}=O)$ ferryl-oxo stretching vibration (9). This experiment showed that this mode appeared at the same rate at which the 568 cm^{-1} mode from Compound A disappeared, indicating a one-step O-O cleaving mechanism by CcO. Since heme a remains oxidized during the A $\rightarrow$ P_m transition, the authors proposed that a tyrosine, Y244, becomes oxidized and provides the reaction with the 4th electron for O-O splitting, which was later verified by $^{125}I^-$ - labeling experiments (5). So, now there is a consensus that the structure of Compound P_m is

{Cu_A^{+2} a^{+3} a_3^{4+}=O Cu_B^{2+} Tyr•}, see Figure 2.3. In addition to his proposed structure, *ab initio* calculations have shown that a radical can be involved during O-O splitting in the mixed-valence reaction (24).

TRRR experiments performed by Varotsis *et al.* (25), as well as by Han *et al.* (26), on the reaction of the fully reduced CcO and O_2 showed that as Compound A disappeared a vibration at 785 cm^{-1} is detected. This mode was shown to belong to an $v(Fe^{4+}$=O) ferryl-oxo stretching vibration, with an isotopic shift of -45 cm^{-1} when $^{18}O_2$ was used. The next and last oxygen isotope-sensitive intermediate that was detected in these experiments was a weak vibration at 450 cm^{-1} and assigned to an $v(Fe^{3+}$-OH) ferric-hydroxy stretching mode, ascribed to Compound H. In contrast to these TRRR experiments, Ogura *et al.* (27) showed that, in addition to the aforementioned oxygen isotope-sensitive intermediates, there is an 804 cm^{-1} species that is immediately formed after the decay of Compound A and before the appearance of the 785 cm^{-1} mode from the ferryl-oxo compound. Since TROA spectroscopy shows that a 607-nm intermediate is first formed before the appearance of a 580-nm species (Compound F) (28-30), Kitagawa assigned the 804 cm^{-1} species to Compound P and the 785 cm^{-1} intermediate to Compound F in the reaction of fully reduced CcO (31).

It was proposed that the initial state of the enzyme controls the path by which O_2 is reduced; i.e., the mixed-valence reaction produces solely the 804 cm^{-1} species, while the fully reduced reaction bypasses the formation of the this species by oxidation of heme *a* (32). Accordingly, formation of Compound F (785 cm^{-1} species) should be responsible for 85% of the oxidation of heme *a*, while the remaining 15% should be oxidized during the decay of the 804 cm^{-1} species (P_m) in the reaction of fully reduced CcO (32).

Recently, Han and colleagues tested this hypothesis by using TRRR experiments at room temperature and showed that the 785 cm^{-1} mode is the only one detected after the decay of the ferrous-oxy Compound A (33). Unlike Ogura et al. (27), they did not observed any band that can be ascribed to the 804 cm^{-1} species, confirming their earlier results (26) and those by Varotsis et al. (25). Han et al. (33) proposed that in Ogura's case, Compound P reached detectable levels because of the differences in the experimental conditions and enzyme protocol, since Ogura's measurements were performed at 3 °C and uses a different enzyme protocol than those used by Varotsis and Han.

Adding to this controversy is the findings by Sucheta and co-workers (28) in which, according to their TROA studies of the reaction of the fully reduced CcO, a 607-nm absorbing species is formed after the decay of Compound A and that heme a oxidation occurs after the appearance of a 580-nm species (Compound F), which is in a 1-to-1 equilibrium with the 607-nm compound (28). In their view, the structure of the 607-nm intermediate is the same as P_m, i.e., a tyrosine radical is formed in the reaction of the fully reduced CcO. In contrast to this view, Morgan et al. (29) proposed that the 607-nm species does not contain a tyrosine radical since the 4th electron for O-O splitting is obtained from the oxidation of heme a and discards the formation of P_m. They claim that the electron transfer from heme a to the binuclear center, during the decay of Compound A, produces a ferryl-oxo species distinct from P_m, thus naming this compound instead as P_r, from the reaction of fully reduced CcO.

According to both of these findings, independent of the controversy of whether or not oxidation of heme a occurs, there is a 607-nm from a ferryl-oxo species that is formed before the appearance of Compound F which is also a ferryl-oxo intermediate.

Hence, there are two ferryl-oxo compounds that should be detected by TRRR spectroscopy, as was shown by Kitagawa and colleagues. Alhough there is an overall agreement on the oxygen structures of the intermediates that are formed in the reaction of fully reduced CcO, the controversy that still lingers is the inconsistency in the Raman field in unequivocally showing that there are two types of ferryl-oxo vibrations. So in this term, a detailed TRRR study has been undertaken to carefully examine the reaction of fully reduced CcO and O_2 to observe the stages of the reaction between the decay of Compound A and formation of Compound F. The work presented in this study will be aimed at resolving the only existing debate in the Raman spectroscopic studies of CcO.

2.2 Materials and methods

The TRRR measurements are based on the Greenwood Gibson flow-flash method (7). The sample preparation and experimental setup used in this study are essentially the same as reported by Proshlyakov and co-workers (9). These will be described in more details in the following two sections.

2.2.1 Sample preparation

The purification of bovine heart CcO was done, with some modifications, following the procedure used by Proshlyakov *et al.* (34). The purified enzyme was dissolved in 100 mM sodium phosphate buffer, pH 7.4, containing 0.21% Brij 35, to a concentration of 100 μM. The fully reduced carbon monoxy-bound CcO (CcO-CO) was prepared by adding cytochrome *c* to a final concentration of 2 μM followed by anaerobic preparation of the sample solution under a carbon monoxide atmosphere. Finally, 2 mM

of ascorbic acid was added to the CO-saturated sample solution to reduce cytochrome c. The solution was incubated for 2 hrs and the formation of CcO-CO was verified by measuring the optical absorption of the sample, in which CcO-CO has a Soret band at 430 nm.

2.2.2 Raman measurements

The experimental setup is shown schematically in Figure 2.4. Two 10-ns pulsed lasers with lines at 594 and 416/427 nm were used as the pump and probes, respectively. The 594-nm output was produced by a pulsed dye laser unit that contained an R590 dye and which was pumped with a high-intensity 532-nm line from an Nd:YAG pulsed laser (DCR Quanta Ray). The probe pulse at 416 nm was obtained by Raman shifting H_2 with a 355-nm line from another Nd:YAG pulsed laser. In addition, a 427 nm line was produced by a solid state XPO pulsed laser from Infinity.

Frequency rates of 10 and 25 Hz were used and a pulse generator (Stanford Scientific) controlled the delay time (t_d) between pump and probe beams from $t_d = 15$ ns to 1600 μs. The pump and probe beams were focused to diameter of about 100 μm onto a rectangular quartz flow cell with cross-section inner dimensions of 1.0 x 0.2 mm. The Raman scattering was collected at $90°$ by using a 50-mm F1.1 camera lens. This scattering was focused onto the slit of a SPEX (model 500M) single monochromator with a N_2 cooled 1024 x 256 CCD detector (SPEX model Spectrum 1). A short-pass filter was used to block the 594-nm light before entering the slit while a notch filter rejected the Rayleigh scattering. The spectral slit width was 10 cm^{-1}.

The O_2-saturated buffer and the fully reduced CcO-CO solutions were loaded into two 25-ml gas-tight syringes, which were driven by an infusion pump at a rate of

110 µL/min. The solutions were pass through an active mixer that was maintained at a

temperature of 20 °C and then flowed through the quartz cell, where at the end, the

resultant sample solution was collected and reused up to 3 times. The initial state of the

enzyme was verified by UV-vis spectroscopy before it was loaded into the syringes and

by observing the 15-ns Raman spectrum of the CO-photolyzed CcO.

The Raman measurements are reported by using difference spectra (Figure 2.5

shows an example) that consists of two sets of identical experiments in which the buffer

contained either $^{16}O_2$, $^{18}O_2$, or the mixed isotope $^{16}O^{18}O$. The Raman spectra were

processed by using ORIGIN (Microcal Software Inc.) and xdsoft (by D.P.) softwares.

2.3 Results

Figure 2.6 displays the resonance Raman difference spectra ($^{16}O_2 - {}^{18}O_2$) of the

reaction between fully reduced CcO and $^{16}O_2/{}^{18}O_2$ at 20 °C and probed at 416 nm,

produced by Proshalyakov *et al.* (68) The initial phase of the reaction from 6.25 to 100 µs

shows the formation and decay of the ferrous-oxy heme a_3 $v(Fe^{2+}-O_2)$ stretching mode at

568/543 cm^{-1}, assigned to Compound A (17,19,20,25,35,36). After the decay of

Compound A, at 100 µs, a weak band centered around 785/747 cm^{-1} starts developing

and reaches a plateau at 400 µs. This vibration is attributed to the $v(Fe^{4+}=O)$ stretching

mode of the ferryl-oxo unit of Compound F (10,25,26,36,37). After 400 µs, the 785/747

cm^{-1} band is then followed by the appearance of an intermediate that displays a vibration

at 453/422 cm^{-1} which originally was assigned by Rousseau and collaborators (26) to the

$v(Fe^{3+}-OH)$ stretching mode of heme a_3. This species is Compound H and was also
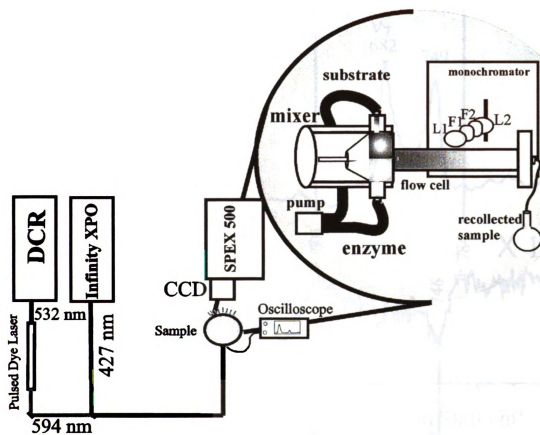
Figure 2.4. Experimental setup used for the NSTRRR measurements.
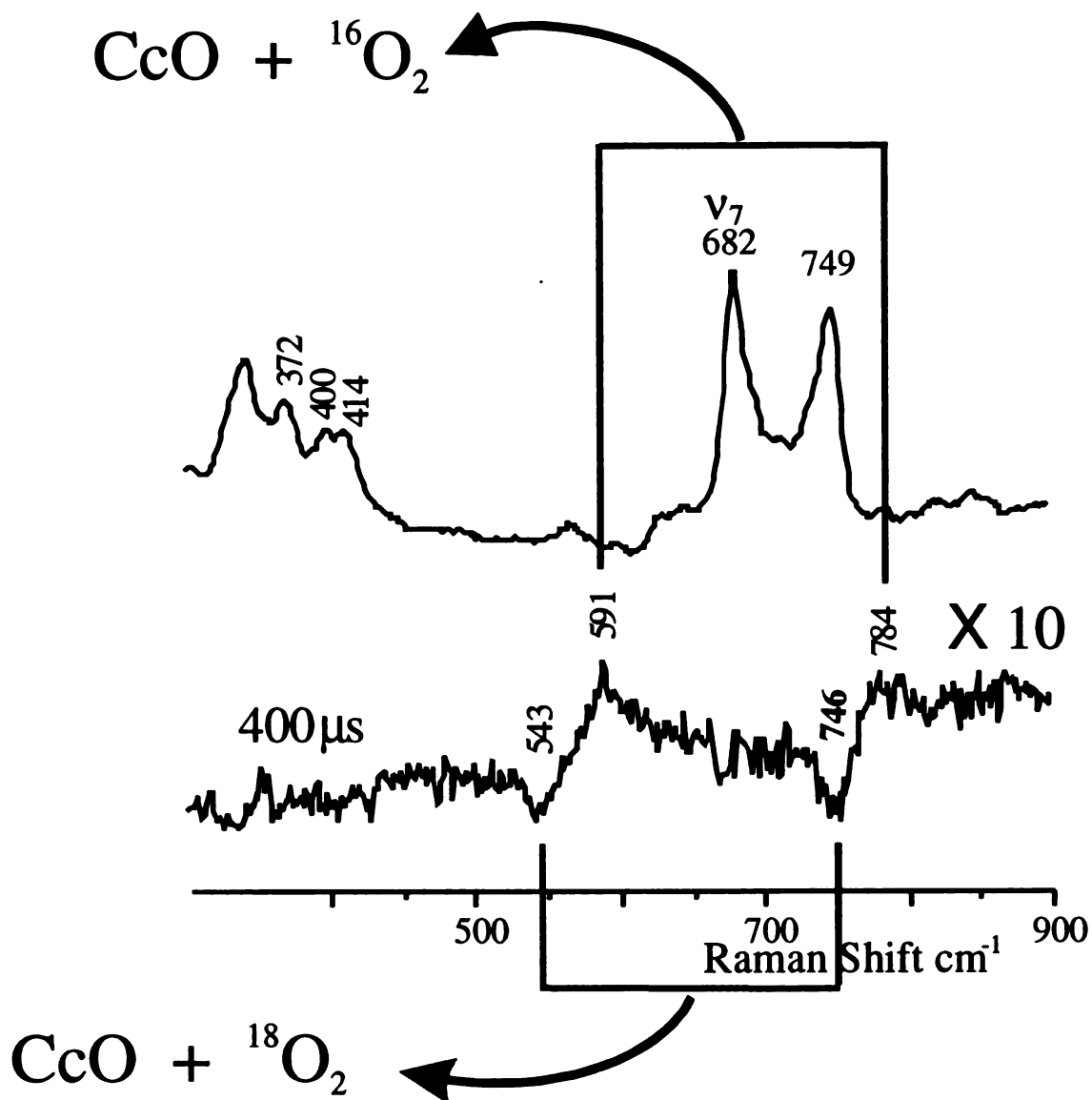
Figure 2.5. An example of an isotope difference spectrum ($^{16}O_2 - {^{18}O_2}$) of the reaction between fully reduced CcO and O_2 at $t_d = 400$ µs. In this region, the absolute spectrum contains various relatively intense Raman bands from the heme (e.g., porphyrin mode ν_7) that cancel each other in the difference spectrum. On the other hand, the oxygen isotope-sensitive intermediates have weak peaks that can be seen in the different spectrum.

observed in the past by Kitagawa and collaborators (36) as well by Babcock and colleagues (25) and most recently in Rousseau's lab (33). The presence of a band at 590 cm^{-1} that shifts to ~545 cm^{-1} when the reaction is carried out with $^{18}O_2$ is very interesting, as it has never been observed before. The intensity of this oxygen-sensitive intermediate develops concomitantly to the formation of the 786/747 cm^{-1} band of Compound F. Figure 2.7 shows a plot of the intensity of the 590/545 cm^{-1} band relative to the intensity of the porphyrin mode v_7 (which does not vary throughout the reaction) versus time. The graph shows that the intensity of the 590 cm^{-1} band reaches a maximum at 400 μs after the $P_r \rightarrow$ F transition has occurred in bovine CcO (13,38).

Further Raman measurements done at 400 μs show that the intensity of the 590/545 cm^{-1} band increases with higher probe powers (Figure 2.8). On the other hand, the intensities of the 785/748 cm^{-1} bands (Compound F) decrease, relative to the intensity of the v_7-porphyrin band, with the higher probe power. This indicates that the 590 cm^{-1} species is photoinduced and its formation derives from Compound F. Careful examination of Figure 2.8 shows that the change in the probe power causes shifts around the 800 cm^{-1} region; the ferryl-oxo peaks are centered at 785/748 cm^{-1} in the 80-μJ spectrum and move to 790/757 cm^{-1} in the 160-μJ spectrum. This shift may be caused by the decrease in the intensity of the 785/748 cm^{-1} peak with the higher probe power, which will then expose another vibrational mode in the 800 cm^{-1} region from another ferryl-oxo compound. Thus, two ferryl-oxo conformers may be present at 400 μs. In Figure 2.9, the high frequency region of the Raman spectra of the reaction between fully reduced CcO and O_2 at 400 μs is compared to that of the 10-ns photoproduct of the fully reduced CO-bound CcO. Each 400-μs spectrum was measured by using a different probe power, and
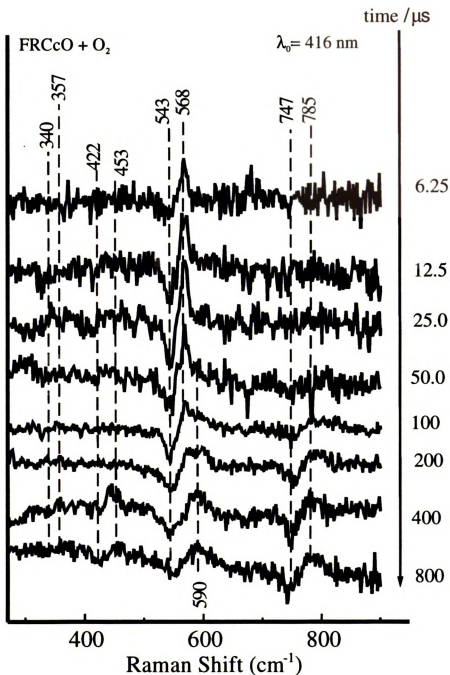
Figure 2.6. Raman difference spectra of the reaction between fully reduced CcO and
$^{16}O_2/^{18}O_2$. Various oxygen isotope-sensitive intermediates are formed during the reaction
that have peaks centered at, 598/543, 785/747, 355/340, 453/422 cm^{-1}, and a
photoinduced intermediate at 590/545 cm^{-1} (from Proshlyakov *et al.* (68)).

as the figure illustrates, the 400-µs spectrum changes with changes in 10-ns pulse probe power. The most notable changes occur in the modes associated with the oxidation state of hemes a and a_3. The bands at 1355, 1517, 1568, 1610, and 1624 cm^{-1}, in the 10-ns photoproduct spectrum are modes that denote the ferrous form of both hemes in the fully reduced state of CcO. At 400 µs, the 10-µJ spectrum in Figure 2.9 shows a decrease in the intensity of the bands from the ferrous hemes, while there is an increase in the 1644 cm^{-1} band due to the ferric and ferryl states of hemes a and a_3, respectively, at this stage (Compound F). However, the other 400-µs spectra show that there is an increase in the intensities of the modes from ferrous heme with the higher probe powers, while at the same time the 1644 cm^{-1} band diminishes.

Due to the spectral contribution of both hemes in Figure 2.9, from a first inspection, it is difficult to distinguish whether only one of the hemes or both hemes are photoreduced with the higher probe power. To clarified this point, and also to identify which of the hemes is rereduced at 400 µs, Table 2.1 shows some of the mode assignments in the high frequency region of the resonance Raman spectrum of CcO that have been made in previous studies. Figure 2.9 shows that as the probe power is increased at 400 µs, the oxidation marker v_4 at 1355 cm^{-1}, indicative of Fe^{2+}, reaches it maximum intensity at about the same level as the Fe^{3+} mode at 1368 cm^{-1}. This indicates that only one heme is rereduced. In addition, the 400-µs, 70-µJ, spectrum shows that the intensities of the vibrations from the ferrous heme such as the bands at 1355, 1610, and 1624 cm^{-1} are about half of those in the 10-ns spectrum of the fully reduced CcO. This further supports the previous observation that only one equivalent of heme is in the

45
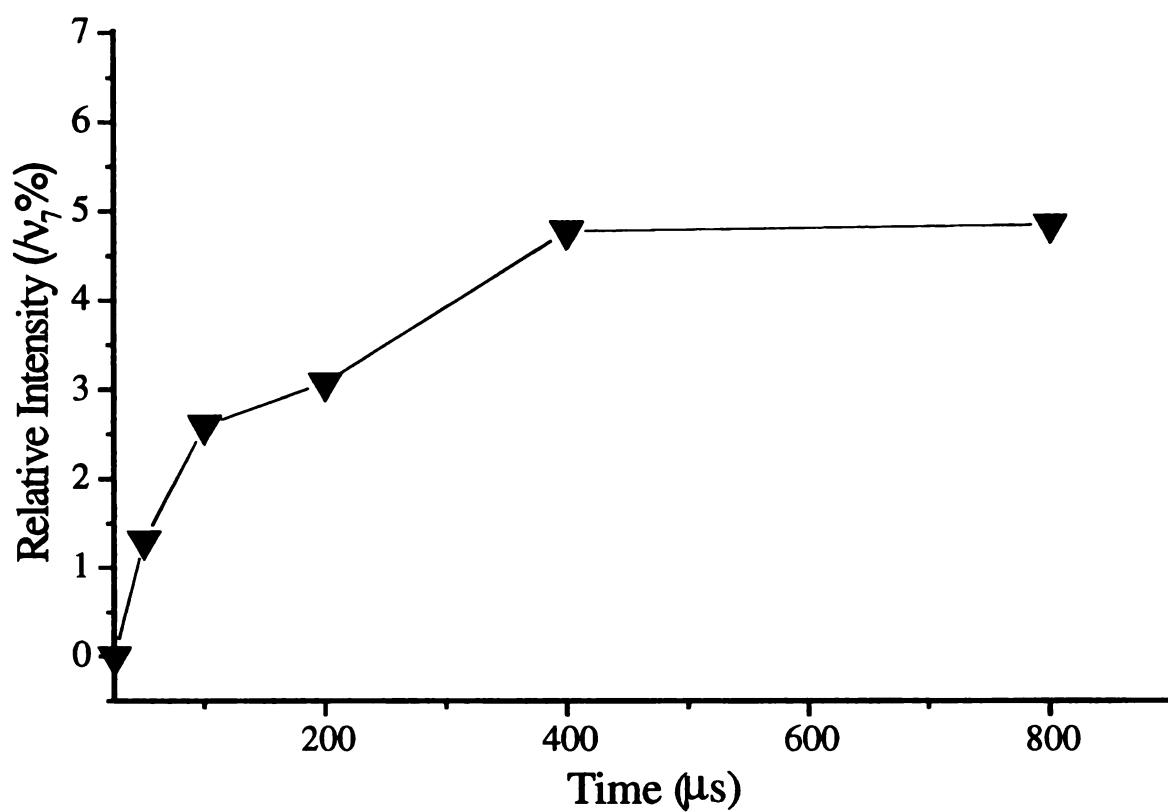
Figure 2.7. Plot of the intensity of the 590/ 543 cm^{-1} peak relative to mode v_7 versus time, from Figure 2.6.
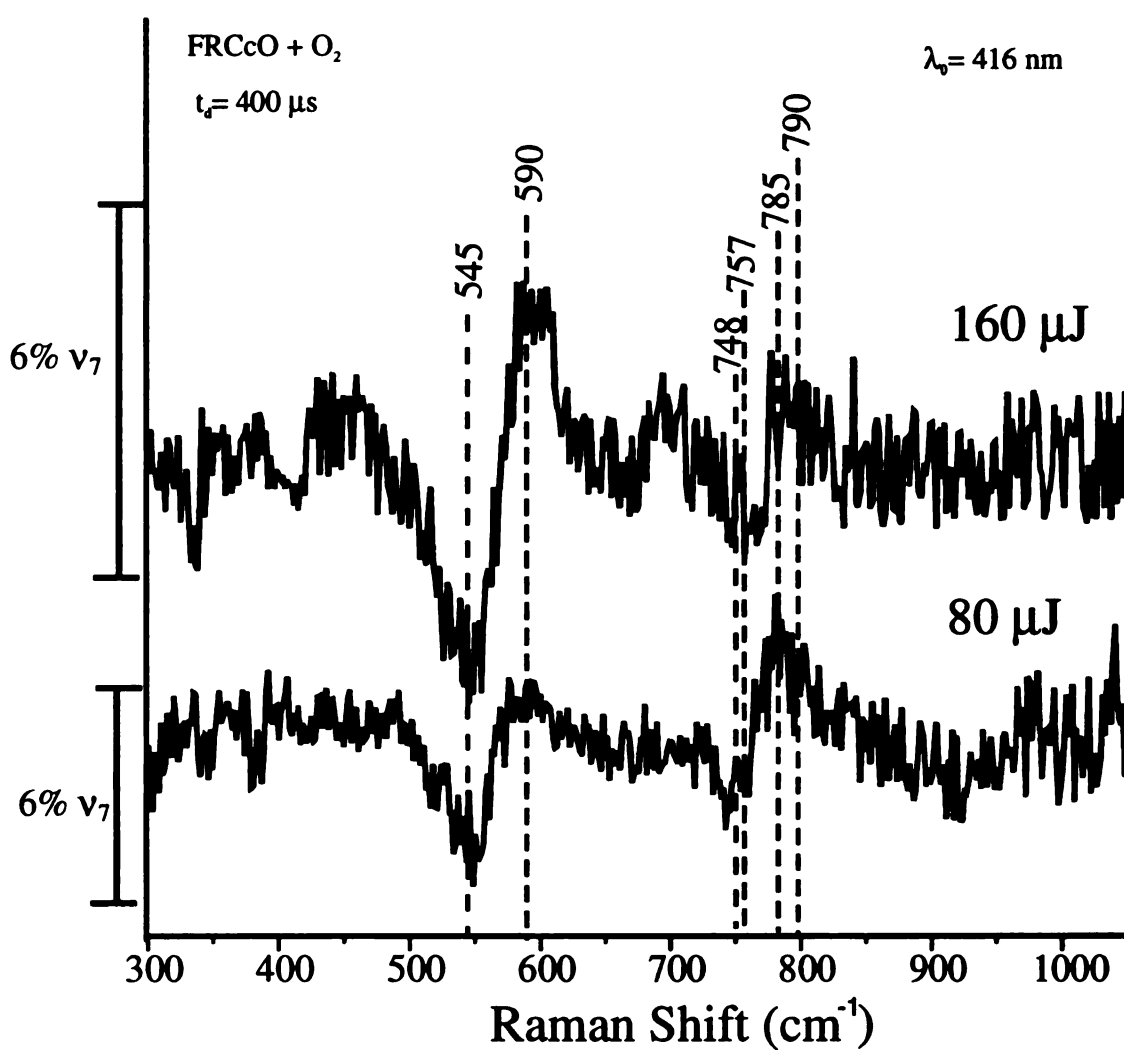
Figure 2.8. Raman difference spectra of the reaction between fully reduced CcO and O_2 at $t_d = 400$ μs. The spectra were obtained with probe intensities of 80 and 160 μJ/pulse.
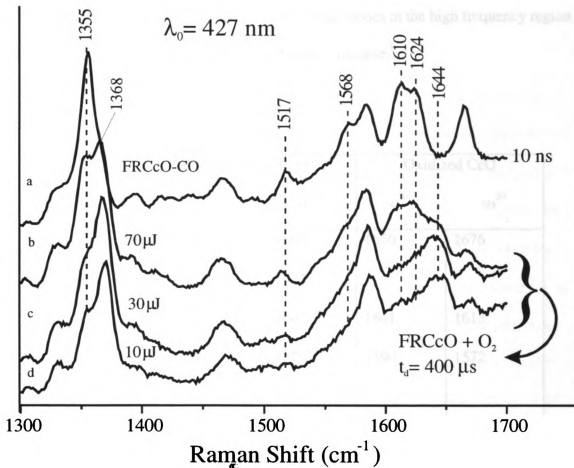
Figure 2.9. High frequency region of the Raman spectra of the reaction between CcO and O_2 at $t_d = 400$ μs, obtained with different probe intensities (b, c, and d). These are compare to the 10-ns spectrum of the photoproduct of the reduced CcO at 10 ns after CO photolysis (a).

Table 2.1. Previously assigned selected vibrational modes in the high frequency region

of the resonance Raman spectrum of cytochrome c oxidase.[¥]

Mode	Reduced CcO		Oxidized CcO	
	a^{2+}	a_3^{2+}	a^{3+}	a_3^{3+}
$\nu_{C=O}$ (formyl)	1610	1665	1650	1676
$\nu_{C=C}$ (vinyl)	1622	1622		
ν_{10}		1607	1641	1615
ν_2	1588	1579	1590	1572
ν_{38}	1568			
ν_{11}	1518			
ν_3	1491	1467	1506	1478
ν_4	1354	1356	1373	1373

[¥]obtained from references: (39-52)

reduced form under high laser intensity at 400 μs. Moreover, the 1517 cm^{-1} band, mode

ν_{11} from ferrous heme a, is about the same intensity level in both spectra. Therefore, at

400 μs only heme a is rereduced when high probe powers are used.

Spectral changes induced by various probe powers are shown in Figure 2.10.

Figure 2.10-a displays the $^{16}O_2$ - $^{18}O_2$ Raman difference spectra of the reaction between

fully reduced CcO and $^{16}O_2/^{18}O_2$ at t_d = 1600 μs. The corresponding absolute spectra of

the high frequency region are shown in Figure 2.10-b. These two figures illustrate the

spectral changes that occur due to changes in the probe power. At 1600 μs, when the

reaction is probed by using 40-μJ pulses, there is no clear indication of the formation of

the 590 cm^{-1} photoinduced intermediate, as shown in Figure 2.10-a. In this spectrum,

there might be oxygen isotope-sensitive peaks around 800 cm^{-1}, but at this power the

signal is too weak to make a conclusive assignment. The high frequency region of the

40-μJ spectrum in Figure 2.10-b shows that hemes a and a_3 are totally oxidized at this

stage, as there are no indications of modes that correspond to reduced heme. This

behavior is different from that at 400 μs where the 590 cm^{-1} species is easily formed,

even at probe powers less than 10 μJ (data not shown). At higher probe powers such as

at 80 and 160 μJ, the $^{16}O_2$ - $^{18}O_2$ Raman difference spectra in Figure 2.10-a show the

presence of the 590/546 cm^{-1} species. An isotopic shift can be seen in the 800 cm^{-1}

region and may consist of multiple peaks, although higher S/N is needed to resolve them.

The corresponding high frequency region of the Raman spectra in Figure 2.10-b now

shows the presence of reduced heme a, indicated by the increase in the signal intensities

around the 1517 and 1610 cm^{-1} regions in the 80- and 160-μJ spectra.
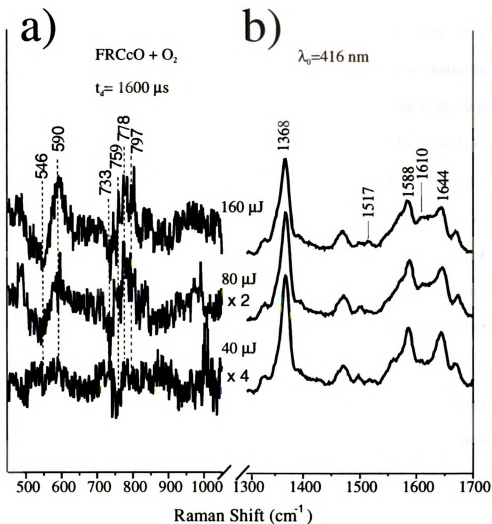
Figure 2.10. TRRR spectra of the reaction between fully reduced CcO and O_2 at $t_d = 1600$ μs. The difference spectra are shown in a) and their corresponding absolute spectra in the high frequency region are shown in b).

Until now, the resonance Raman measurements of the reaction between fully

reduced CcO and O_2, done with excitation at 416 nm (Figure 2.6), show that after 100 μs

the 568 cm^{-1} mode of Compound A decays with the detection only of the 785 cm^{-1} band

from Compound F. In Figure 2.6 there are no clear indications of an intermediate that is

formed between compounds A and F. Ogura *et al.* (27) showed that in the sequential

order of intermediates formed during the reaction of fully reduced CcO and O_2, there is

an oxygen isotope-sensitive species, other than Compound F, formed immediately after

Compound A. According to Kitagawa (31), this species should be the "P_r" intermediate,

which has been detected by optical absorption spectroscopy (28,30) and more recently by

EPR (29). Since this intermediate was not detected by using 416-nm laser excitation, a

set of Raman experiments were done by using excitation at 427 nm, from $t_d = 50$ to 400

μs in H_2O and D_2O and shown in Figure 2.11.

The spectra in Figure 11 were normalized by using the intensity of the porphyrin

mode v_7. The $^{16}O_2 - {}^{18}O_2$ difference spectrum of the reaction in H_2O at 50 μs shows the

568/543 cm^{-1} peaks from Compound A and less intense peaks in the 800 cm^{-1} region

(Figure 2.11-a). These smaller peaks are centered at 804 and 769 cm^{-1} in the difference

spectrum. Because of its early appearance, as the oxy compound decays, this mode

corresponds to "P_r". This is the first time this species has been detected by resonance

Raman spectroscopy at 50 μs and at room temperature. Proshlyakov *et al.* (23) assigned

the 804 cm^{-1} peak in their spectra to a $v(Fe^{4+}=O)$ ferryl-oxo stretching vibration.

Similarly, this assignment has been adopted for the detected 804 cm^{-1} intermediate.

Time-resolved optical absorption spectroscopic studies of the reaction between

fully reduced CcO and O_2 have shown that the formation of F is slowed by a factor ~ 4 in

D$_2$O (53). So to further increase the population level of P$_r$ by delaying the formation of

Compound F, the reaction was done in D$_2$O and measured at the longer pump-probe t$_d$ =

100 and 200 µs, figures 2.11-b and 2.11-c, respectively. At 100 µs, in Figure 2.11-b, the

804 cm^{-1} band is slightly shifted in D$_2$O to about 800 cm^{-1}. As the reaction proceeds in

D$_2$O, after 200 µs the 800 cm^{-1} peak in Figure 2.11-b now shifts to around 790 cm^{-1} in

Figure 2.11-c. The peaks in the difference spectrum at 200 µs are broader than the peaks

in the 50- and 100-µs spectra and similar to the 400-µs spectrum in Figure 2.11-d. This

may be due to the coexistence of two conformers that can be resolved into a pair of

ferryl-oxo (Fe^{4+}=^{16}O/Fe^{4+}=^{18}O) peaks centered at 804/769 and 785/749 cm^{-1} in H$_2$O at

400 µs. The appearance of another mode in the 790 cm^{-1} region, at 200 µs, indicates the

presence of Compound F. The 804/769 and 785/749 cm^{-1} peaks further increase their

intensities as the reaction reaches 400 µs in H$_2$O (Figure 2.11-d). At this stage, the

difference spectrum in Figure 2.11-d definitively shows that there are two modes in the

790 cm^{-1} region. Comparison between the ferryl-oxo peaks in D$_2$O and in H$_2$O (figures

2.11-c and 2.11-d, respectively) shows that the deuterium isotopic shifts are very small,

yet hard to determine because of the proximity of the peaks and their overlap in the

difference spectra. It is interesting to note the behavior of the photoinduced species

denoted by the peak at 590 cm^{-1} in the difference spectra in figures 2.11-c and 2.11-d. As

mentioned before, the photoinduced species is clearly produced after 100 µs, at the "F"

stage of the reaction (Figure 2.6). In Figure 2.11-a, the "P$_r$" intermediate is present at 50

µs, while the 568 cm^{-1} mode of the ferrous-oxy species is still decaying. This 568 cm^{-1}
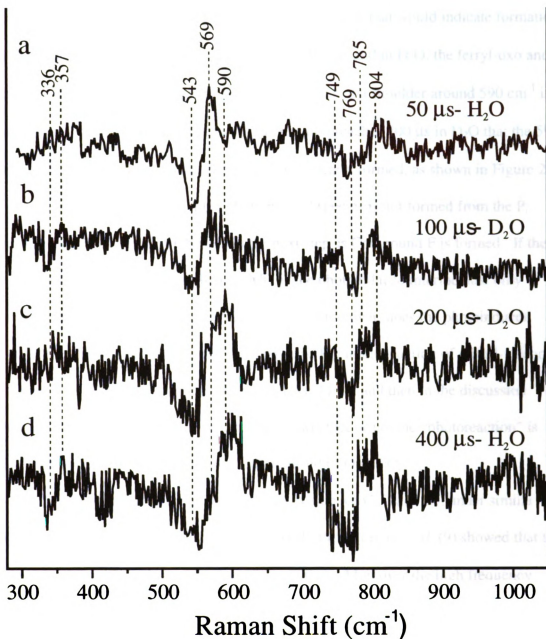
Figure 2.11. Nanosecond-TRRR spectra of the reaction between fully reduced CcO and O_2 at 20 °C and excitation done at 427 nm. The time delays between pump and probe beams were, $t_d = 50$, 100, 200, and 400 μs. Spectra b) and c) were obtained by carrying out the reaction in 80% D_2O. The laser power was ~ 40 μJ/pulse for each spectrum.

peak does not display any shoulder in the 590 cm^{-1} region that would indicate formation

of the photoinduced intermediate. Moreover, at 100 μs and in D_2O, the ferryl-oxo and

ferrous-oxy peaks are present with still no indications of a shoulder around 590 cm^{-1} in

the 568 cm^{-1} peak. Hence, it is not until the reaction reaches 200 μs in D_2O that the 590

cm^{-1} peak from the photoinduced intermediate is clearly formed, as shown in Figure 2.11-

c. In other words, it seems as if the photoinduced species is not formed from the P_r

intermediate, but instead, afterwards in the next step as Compound F is formed. If the P_r

and F compounds are both ferryl-oxos, why is the photoinduced intermediate only

formed after the reaction has passed the P_r stage. Moreover, does the photoinduced

species form during the presence of the ferryl-oxo P_m, in the reaction of mixed-valence

CcO and O_2? The latter question will be addressed first, and then in the discussion

section the former will be answered, in light of whether or not the "photoreaction" is

particular to the reaction between the fully reduced CcO and O_2.

In regards to the reaction between mixed-valence CcO and O_2, under similar

experimental conditions as was used in this work, Proshlyakov et al. (9) showed that the

590 cm^{-1} peak is never formed from t_d= 25 to 800 μs. Moreover the high frequency

region of Raman spectra show that heme a remains oxidized throughout the reaction, as

there are no bands in the 1517 and 1610 cm^{-1} region that can be attributed to reduced

heme a (Proshlyakov, personal communication). These two behaviors (absences of the

590 cm^{-1} species and reduced heme a) are contrary to what is observed in the reaction of

the fully reduced CcO, as presented in this work.

2.4 Discussion

2.4.1 Intermediates in the reaction of fully reduced CcO and O_2

The time-resolved resonance Raman measurements, using 416 nm excitation and in H_2O (Figure 2.6), clearly show the formation of compounds A, F, and H, represented by the lines at 568/543, 785/747, and 453/422, respectively. Judging by their Raman intensities in Figure 2.6, intermediate A is fully formed at about 25 μs, while F reaches it maximum level after 200 μs. This time profile for the appearance of A and F is in agreement with time-resolved optical absorption studies done on the reaction between fully reduced CcO and O_2 at room temperature (54). In this series, Compound P_r was not detected because of the combination of various factors such as: low signal intensity of P_r; low S/N ratio of the spectra; relatively fast $P_r \rightarrow F$ transition that results in the overlap of the two ferryl-oxo modes within a very short time interval; and finally, the ferryl-oxo mode is only further enhanced by excitation at about 427 nm (55). In this study, P_r was detected, with low signal intensity at 804 cm^{-1} and at 50 μs, with Raman excitation at 427 nm (Figure 2.11a). The time at which this intermediate is formed is in close agreement with the aforementioned time-resolved optical absorption studies, which showed that Compound P_r appears with a time constant $\tau = 30$-50 μs. In overall, the approximate times at which intermediates are formed in this Raman study are similar to those found by the time-resolved optical absorption studies.

Table 2.2 summarizes the most important results obtained by the various groups that historically have studied the reaction between fully reduced CcO and O_2 by using time-resolved resonance Raman spectroscopy. Each group has been labeled according to their primary investigator, D.L. Rousseau, T. Kitagawa, and G.T. Babcock. The

56

discrepancies in this work with previous ones, and the differences in the results among the labs that have studied the reaction of CcO by Raman spectroscopy, can be rationalized by understanding the behavior of P_r. According to the results obtained by excitation at 416 nm (Figure 2.6), the 568 cm^{-1} peak from the ferrous-oxy heme a_3 decays with the formation of the 785 cm^{-1} peak from F, bypassing detection of P_r. This result is similar to that observed in the past by Varotsis *et al.* (10,25), and more recently by Han *et al.* (33). Contrary to this, the P_r intermediate (804 cm^{-1}) is clearly present in the Raman spectra before the formation of F, as was originally shown by Ogura *et al.* (27). However, when P_r was detected by Raman excitation at 427 nm, its intensity was low (Figure 2.11a), at about half of the intensity of Compound F in Figure 2.11-d. In addition, the isolated 804 cm^{-1} peak is short-lived, since the 785 cm^{-1} mode appears relatively fast at room temperature. In this study formation of F was delayed by running the reaction in D_2O (figures 2.11-b and 2.11-c). The transition from 804 cm^{-1} to 785 cm^{-1} occurred in less than 100 μs, as the 801 cm^{-1} peak at 100 μs shifts to a broad 790 cm^{-1} peak at 200 μs in figures 2.11-b and 2.11-c, respectively. Since the KIE is ~ 4 (53), then roughly estimated the $P_r \rightarrow$ F transition in H_2O occurs in less than 30 μs. This means that if P_r accumulates to a level for which it can be detected by Raman spectroscopy (this point will later be discussed further), the time resolution of the experimental setup should be an order of magnitude shorter than the $P_r \rightarrow$ F transition. In the experimental setup used by this lab, the reaction is started and probed at the same point in the flow cell and the time resolution depends on the duration of the pump and probe pulses, which is about 10 ns. This type of setup was used in the past by the Babcock lab, however P_r may have

Table 2.2. Oxygen-sensitive iron-ligand modes in the reaction between fully reduced CcO and O_2 in H_2O.[†]

vibration (cm^{-1})	assignment	Rousseau[a]	Kitagawa[b]	Babcock[c]
568	$\nu(Fe^{2+}\text{-}O_2)$ "A"	Detected by the three groups. This is the most intense mode in the spectra and corresponds to Compound A.		
804	$\nu(Fe^{4+}=O)$ "P$_r$"	undetected	Detected after 200 μs at low temperature. The intensity of this mode develops to the same level as "F" in their spectra.	This is the first time this mode has been observed in this lab. It is also the first time this intermediate is detected at room temperature and at 50 μs. However, the intensity of this vibration is lower than that of Compound F.
785	$\nu(Fe^{4+}=O)$ "F"	Detected by the three groups. This mode appears after the decay of Compound A in the spectra. The intensity of this mode is relatively low in comparison to "A".		
453	$\nu(Fe^{3+}\text{-}OH)$ "H"	Observed by the three groups. This vibration appears after the formation of "A" and "F" and has a very low intensity because of oxygen exchange surrounding water molecules.		

[a] obtained from references: (12,18,26,33,56)

[b] obtained from references: (19,27,36,37,48-50)

[c] obtained from references: (10,17,25)

[†] This table does not include the 355 cm^{-1} mode, which has been detected by the three groups but its assignment is unclear. It appears after the decay of A and diminishes before the reaction reaches the H stage.

passed undetected because of low S/N, in addition to the low level of P_r that is formed during the reaction. Now in this case, while preserving the use of the 10-ns pulse lasers, substantial changes were made by Proshlyakov *et al.* (9, 57) to the setup to improve the S/N. On the other hand, the time resolution might have been the reason that Rousseau's lab did not detect P_r. In their most recent study (33), their spectrum at 65 μs shows the ferrous-oxy species decaying while a band is formed at 785 cm^{-1}, which corresponds to the fast formation of Compound F; in their case, they used CW lasers. Thus, the time resolution of their setup depends on the distance between the pump and probe beams (~15 μs when both beams overlap) as well as on the dynamics of the flow of the sample volume as it moves from the pump to the probe point within the cell. This may indicate that their time resolution is close to the 30 μs interval for which the P_r- to- F transition occurs at room temperature. Therefore in their case, P_r would be difficult to observe since this compound is not populated under their experimental conditions and may overlap with Compound F within their time resolution (33). In this regard, they reported a broad band centered at 786 cm^{-1} at t_d= 65 μs, which may indicate the presence of P_r. Similarly, Kitagawa's lab used CW lasers and their time resolution is in the same order as Rousseau's setup. However, they carried out the reaction at low temperature (~3 °C), so that the intermediates were formed slowly. This permitted them to unequivocally observe the formation of the 804 cm^{-1} peak followed by the formation of the 785 cm^{-1} peak from F.

2.4.2 The structure and level of P_r

In a detailed O_2-isotopic Raman spectroscopic study, it was shown that the 804 cm^{-1} vibration of Compound P_r is sensitive to only one oxygen atom and therefore its assignment to an $v(Fe^{4+}=O)$ stretching mode (36). This vibration is similar to that from the ferryl-oxo P_m produced in the reaction of mixed-valence CcO and O_2 (9). The optical properties of these two species are also identical with an absorption peak at 607 nm in the difference spectra (28,29). In addition, the deuterium isotope effects for the formations of P_r and P_m are about the same (~ 1.5), as it was demonstrated these effects were associated to an internal proton/hydrogen transfer (15). The only difference between the two P species, is the presence of an extra charge in the binuclear center in P_r. This extra electron derives from the oxidation of heme a during the reaction of the fully reduced CcO and O_2 (18). On the other hand, the binuclear center of P_m instead is neutral containing a tyrosyl radical that is crossed-link to a histidine that is bound to Cu_B (5). Thus, it is expected that the binuclear center in the P_m state is

$$[Fe^{4+}=O \ HO-Cu_B^{2+} \ Y-O\bullet] \ (P_m)$$

and the structure of the binuclear center in Compound A is,

$$[Fe^{2+}-O_2 \ Cu_B^{1+} \ Y-OH] \ (A)$$
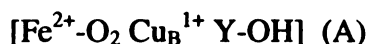
Comparing these two structures, the four electrons that are used for O-O splitting in the mixed-valence CcO are as follow: 2e- from the Fe^{4+}/Fe^{2+}, 1e- from Cu_B^{2+}/Cu_B^{1+} and 1e- from $Y\bullet/Y$. In the case of the fully reduced CcO, O-O splitting is more complex to describe because of the initial presence of two extra reducing equivalents (1e- from Fe^{3+}/Fe^{2+} in heme a and 1e- from Cu_A^{2+}/Cu_A^{1+}). In addition, because P_r is produced transiently in a very short time, its structure determination by experimental means at

60

room temperature has been a challenge. However, in a recent EPR study done by trapping P_r at low temperatures, it was determined that the copper in the binuclear center is in its cupric form (Cu_B^{2+}) (29). With this information, and from the optical absorption and Raman studies, the four electrons involved in the formation of "P_r" are: 2e- from the Fe^{4+}/Fe^{2+} (heme a_3), 1e- from Cu_B^{2+}/Cu_B^{1+} and 1e- from Fe^{3+}/Fe^{2+} (heme a). Thus, the mechanism is different from that of the formation of P_m because the reaction can proceed without the need to oxidize the tyrosine. To finally propose a model for the structure of "P_r", the location of the extra charge that originates from heme a needs to be determined. Due to the similarity in the ferryl-oxo ($Fe^{4+}=O$) vibrations of P_m and P_r, the extra charge in P_r should reside far from the ferryl-oxo unit; otherwise the vibration of the ferryl-oxo unit should be affected (58). The tyrosine (Y244) is a good candidate as the site that bears this extra e-,

$$[Fe^{4+}=O \; HO-Cu_B^{2+} \; Y-O^-] \; (P_r)$$

The proposed structures of P_m and P_r invoke the utilization of the hydrogen/proton from the tyrosine for O-O splitting. This would be in agreement with studies that have shown that the rate-limiting steps in forming P_r and P_m are hydrogen/proton dependent and exhibit the same deuterium isotope effects (15). However, the structures of these two compounds would suggest different transition states and therefore different rates of formations, as has been found experimentally (32).

Two different schemes are proposed for the formation of P_r and P_m, as shown in Figure 2.12. These schemes are similar to those proposed by Brzezinski and collaborators (15), with the exception of a few differences. In the case for the reaction of the mixed-valence CcO, Compound A is in equilibrium with a true peroxy intermediate

61

in the transition state, in which there has been an H abstraction from the tyrosine (Figure 2.12-a). In this case, the abstraction would be assisted by the formation of Cu_B^{1+}, i.e., concerted H^+ and e- transfers but through different paths. This transition state structure is different from what was proposed by Karpefors *et al.* (15), in which they suggested that Cu_B is in the cupric state. Similar to the P_m scheme, in the fully reduced CcO reaction, Compound A is in equilibrium with the low populated peroxy intermediate but the electron donor would be heme a instead of Cu_B^{1+} (Figure 2.12-b). Formation of the transition state structure involves the deprotonation of the tyrosine. The rate-limiting step in both reaction schemes would involve the protonation of the "undetected" peroxy transition-state intermediate. According to the schemes, this would be achieved differently and the rates of formation of P_r and P_m should reflect that, as was mentioned before. To test the feasibility of these reaction pathways, the relative activation energies (E_a) will be deduced as follows.

Lets assume that the ΔG^* in the reaction of MVCcO and O_2 is the same as the energy involved in tyrosine radical formation, $Y \rightarrow Y\bullet$, ~0.97 V at pH 5.0 (59). The ΔG^* in the reaction of FRCcO, is the $Y \rightarrow Y^-$ conversion, a thermodynamically unfavorable step because of the high pKa of tyrosine (~10). Assuming that this deprotonation can occur by intrinsically generating a tyrosyl radical, $Y \rightarrow Y\bullet \rightarrow Y^-$. The reducing potential of $Y\bullet$ ($Y\bullet$ /Y^-) is 0.68 V, so the ΔG^* for $Y \rightarrow Y^-$ conversion should be 1/3 of that for $Y \rightarrow Y\bullet$. This means that formation of P_r by tyrosine deprotonation would be kinetically competent, and even more favorable than formation of P_m. However,
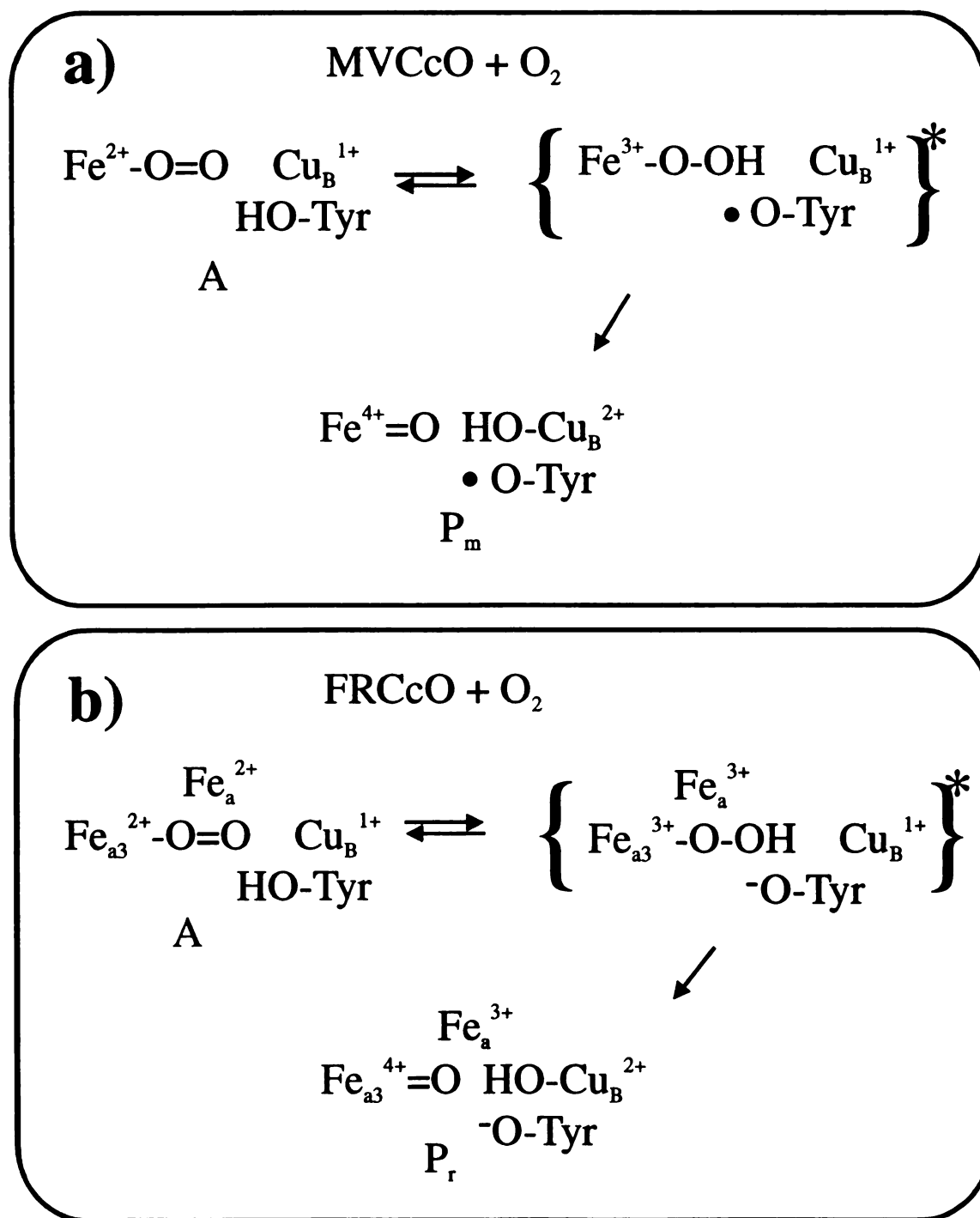
Figure 2.12. Proposed O-O splitting mechanisms in the reaction between mixed-valence CcO and O_2 a), and in the reaction between the fully reduced CcO and O_2 b).

according to Rich *et al.* (60) the extra charge in the binuclear center would have its cost, as it would decrease the driving force for the creation of P_r. The evaluation of this effect is not straightforward, and might be as the same magnitude as the energy required to lower the pKa of the tyrosine (from 10 to ~7). This ΔpKa may even be lower than expected because it has been shown that the crossed-link histidine may decrease the acid dissociation constant of the tyrosine (6).

The extra charge in the P_r state drives the translocation of protons within the enzyme that results in the addition of a proton to the binuclear site during the $P_r \rightarrow F$ transition (32). The final proton acceptor is yet unknown, but it should be very close to the ferryl-oxo unit where it would be responsible for the changes in its Raman (804 $\rightarrow$ 785 cm^{-1}) and optical properties (607 $\rightarrow$ 580 nm) as P_r converts to F (29). Morgan *et al.* (29) proposed that the proton acceptor is the $^-$OH group in Cu_B where it is finally converted to H_2O. As the A $\rightarrow$ P_r and $P_r \rightarrow$ F transitions occur, P_r accumulates to a certain level during the reaction between fully reduced CcO and O_2. This point has been the source of controversy among research groups in the optical absorption and Raman spectroscopy fields as there is no consensus on the amount of P_r that can be produced. Stated more specifically, there is a debate on whether or not P_m can also be formed during the reaction of the fully reduced CcO in a branching-type mechanism (section 1.3). In this mechanism, Compound A decays both to P_r (as heme *a* oxidizes) and P_m (through the formation of the tyrosine radical). In the next paragraph, this will be discussed in terms of the Raman results obtained in this work.

In the reaction of mixed-valence CcO and O_2, the intensity of the 804 cm^{-1} peak reaches a maximum with about 5% of the intensity of the reference peak, v_7 (9). In this

work, the intensity of the 804 cm^{-1} peak of P$_r$ reaches a maximum of about 2% of v$_7$ before the appearance of F (figures 2.11-a and 2.11-b). Thus, assuming that the P$_r$ and P$_m$ structures have the same Raman cross-sections, the maximum amount of P$_r$ produced at most is about 40% before the P$_r$ → F transition. The 804 cm^{-1} peak that appears before the P$_r$ → F transition corresponds to P$_r$ because, according to the Raman data, heme a is oxidized during the formation of P$_r$. This is indicated by the changes in the Raman bands associated with heme a, as the reaction crosses the P$_r$ stage (although changes are observed because of the oxidation heme a, these cannot be quantified with the Raman data). After the appearance of F (Figure 2.11-d), there are clearly two ferryl-oxo modes at ~785 and ~804 cm^{-1} and the question is if the latter is from either P$_r$ or P$_m$. Alternatively, the 804 cm^{-1} band at the F stage may correspond to another ferryl-oxo conformer, different from that of P$_r$ and P$_m$, in equilibrium with the 785 cm^{-1} from Compound F. Unfortunately, proof cannot be provided for the support of any of these proposals and further studies should be undertaken to resolve this issue.

2.4.3 The photoinduced species

More than two decades ago, as the field of resonance Raman spectroscopy bloomed with its application to heme proteins, it became apparent that sorting out the mode assignments for hemes a and a_3 in CcO was problematic due to the phenomenon of photoreduction. Initially this was first observed by Adar and Yonetani (61) and later confirmed by other groups (62,63). In their experiments, oxidized CcO would be photoreduced under CW laser excitation during the Raman measurements; to circumvent this problem, various methods were developed to avoid the long laser exposures

(40,64,65) and. The photoreduction process is characterized by the reduction of heme a

and a_3, and possibly Cu_B and Cu_A, during the Raman scattering of fully oxidized CcO. In

a detailed study of this process, Ogura *et al.* (48) showed that of all the possible

intermediates that can be formed because of the photoreduction, $a^{2+} a_3^{3+}$ is the major

contributor to the Raman spectra during the measurements of oxidized CcO. This

confirmed the earlier observations made by Babcock and co-workers (40). Later,

Varotsis and Babcock (66) used nanosecond-TRRR to demonstrate that retardation of the

oxidation of heme a during the reaction of fully reduced CcO and O_2 was a function of

the intensity of the 10-ns pulsed-laser probe. In their view, this was caused by the

photolability of the ferrous-oxy Compound A that forms a 5-coordinate ferrous heme a_3

under high laser powers.

In this study, it is shown that during the reaction of fully reduced CcO and O_2, a

590 cm^{-1} species is formed concomitantly with the photoreduction of heme a. However,

this is the first time that an oxygen isotope-sensitive species is detected during the

photoreduction of CcO. This species is clearly formed after the decay of Compound A

and correlates with the formation of Compound F, 200 μs after initiation of the reaction

(see Figure 2.6). Moreover, as shown in Figure 2.8, this photoinduced species is formed

from F, since the intensity of this species increases while that of the ferryl-oxo

Compound F decreases. The assignment of the 590 cm^{-1} species has been problematic

because although the vibration is close to that of the ferrous-oxy Compound A

(568 cm^{-1}), its isotopic shift is about -45 cm^{-1} with $^{18}O_2$, typical of oxo ferryl compounds

that have vibrations in the 700 to 800 cm^{-1} region. To further complicate the assignment,

Figure 2.13 shows that this species is not sensitive to the mixed-isotope $^{16}O^{18}O$, which

66

therefore means that the structure should be Fe-O-X; where the oxidation of the iron and X need to be determined.

The re-reduction of heme a at the F stage with the high pulsed-laser intensities is interesting in that this occurs while CcO is interrogated within the duration of the 10-ns pulse probe. Since the photoreduction occurs at the same time the photoinduced species is formed, the binuclear center is a good candidate as the reducing source (this is schematically shown in Figure 2.14). Thus, the electron transfer can be from heme a_3 to heme a and form a reduced-oxidized pair, similar to the intermediate formed during the photoreduction of oxidized CcO, as mentioned before. The only difference is that the detected photoinduced species contains an oxygen derivative, as has been proven in this work.

The notion that heme a can be reduced by heme a_3 under high laser intensities during the duration of the probe pulse is a hard one to dwell on, since this electron transfer rate should be ~10^9 s^{-1}, 5 orders of magnitude higher than the forward rate during the A $\rightarrow$ P$_r$ transition (3×10^4 s^{-1}). However, since the A $\rightarrow$ P$_r$ transition is proton dependent (KIE ~ 1.5) and assuming an edge-to-edge electron transfer between heme a and a_3 (distance is 7 Å), it is reasonable to assume that the true electron transfer rate between both hemes can be faster than the microsecond interval (67). The fact that the A-to-P$_r$ conversion is proton dependent has also been demonstrated in this Raman experiment in which the relative intensities of the 568 and 804 cm^{-1} peaks (A and P$_r$), are the same in the 50-μs-in-H$_2$O and the 100-μs-in-D$_2$O spectra (Figure 2.11). In contrast, the formation of the photoinduced species is not affected by D$_2$O, as it still can be formed
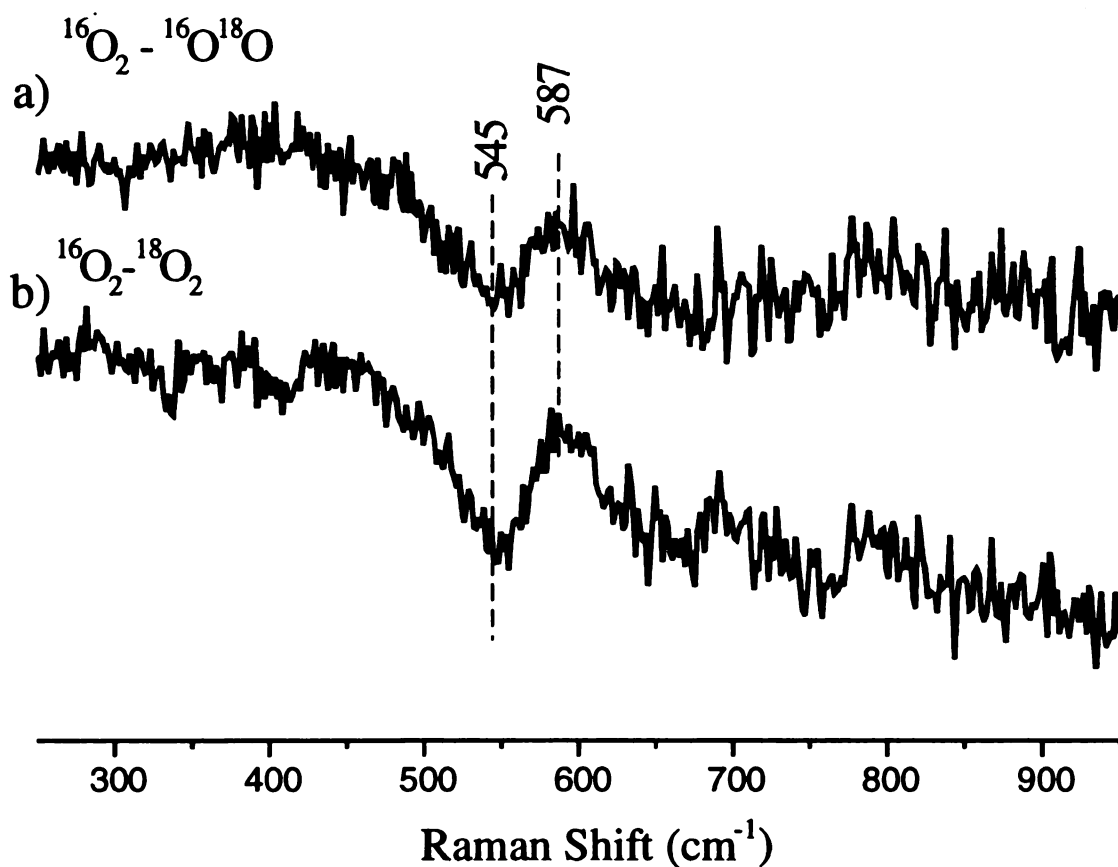
Figure 2.13. Nanosecond-TRRR spectra of the reaction between fully reduced CcO and O_2 at a pump-probe $t_d = 400$ μs. The $^{16}O_2$ - $^{16}O^{18}O$ difference spectrum is shown in a), while the $^{16}O_2$ - $^{18}O_2$ difference spectrum is shown in b). Comparison of the two spectra demonstrates that the negative peak at 545 cm^{-1} from the photoinduced species is not sensitive to the mixed isotope ($^{16}O^{18}O$).

$$\left\{ \, a_3{}^{4+}{=}O^{2\text{-}}\ Cu_B{}^{2+} \right\}^*$$

$$\{a^{3+}\ Cu_A{}^{1+}\}$$
$$a_3{}^{4+}{=}O^{2\text{-}}\ Cu_B{}^{2+}$$

$$\left\{ \begin{array}{l} \text{heme } \text{a is rereduced} \\ \text{while } a_3 \text{ forms a species} \\ \text{containing an oxo unit} \end{array} \right\}$$
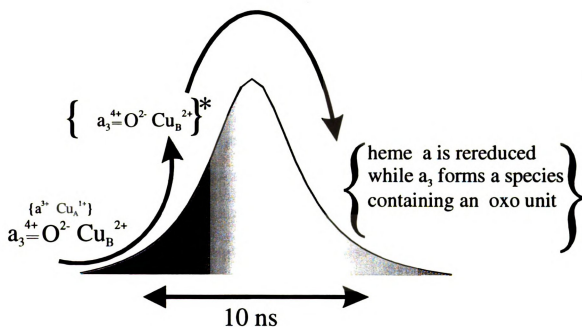
10 ns

Figure 2.14. Schematic representation of the proposed process that occurs during the duration of the probe pulse for the formation of the photoinduced intermediate.

within the duration of the 10-ns probe illumination (compare figures 2.11-c and 2.11-d). Moreover, the 590-cm^{-1} vibration of the photoinduced species is unperturbed in D_2O, as it has the same frequency as in H_2O. Thus, the back electron transfer from heme a_3 to heme a during the formation of the photoinduced species can be faster than the microsecond interval because the process is uncoupled to proton transfer.

The reaction of the mixed-valence CcO and O_2 does not produce the photoinduced species under pulsed-laser illumination (9); this is in contrast to the reaction of the fully reduced CcO that has just been discussed. In addition, during the reaction of the mixed-valence CcO, after the formation of Compound A, heme a remains oxidized at the P_m state (Proshlyakov, personal communication). From this observation, it can be concluded that heme a remains oxidized because the photoinduced intermediate doesn't form from P_m. Similarly, it was shown that there is no evidence of the formation of the 590 cm^{-1} peak from the photoinduced intermediate during the presence of the 804 cm^{-1} from P_r (figures 2.11-a and 2.11-b). The 590 cm^{-1} mode appears after P_r, during the formation of "F". Thus, "P_r" and "P_m" may have very similar structures, which are not favorable for the formation of the photoinduced compound. Hence, the binuclear center undergoes a structural rearrangement as the enzyme changes from the "P_r" to the "F" state, which permits the formation of the photoinduced intermediate. This structural change may result in the movement of Cu_B closer to the iron of a_3, where it would affect the Raman and optical properties of the heme and permit the formation of the photoinduced compound. The proximity of Cu_B to the heme a_3 iron in the F state, may also be responsible for the changes that are observed in the EPR spectrum of Cu_B during the $P_r \rightarrow$ F conversion (29).

In this study, formation of the photoinduced species was followed up to 1600 μs after initiation of the reaction between fully reduced CcO and O_2. There is a decrease in the intensity of the 590 cm^{-1} mode from the photoinduced species, such that the vibration is only observed with higher probe powers (Figure 2.10a). This stage of the reaction corresponds to the F-to-H transition and the decreased intensity of the vibration may be due to the appearance of another undetected mode, due to oxygen exchangeability with the surrounding water molecules. This would be similar to the ferric-hydroxy Compound H, where the Raman intensity is decreased due to oxygen exchangeability (33). If a photoinduced intermediate were formed from H, then its detection would be affected by the oxygen exchange because these experiments were performed with $H_2^{16}O$.

The X-ray crystal structure of CcO shows that Cu_B moves closer to the iron of heme a_3 during the oxidation of the binuclear center: 5.1 Å in the fully reduced state (R) and 4.9 Å in the oxidized form (4). Therefore, although undetected, there should be a photoinduced intermediate at the H stage, since the structural changes would permit this, as was discussed for Compound F. This intermediate may then reduce heme a during the laser exposure and would explain the initial observations that were made over two decades ago about the phenomenon of the photoreduction of oxidized CcO.

c

2.5 Literature Cited

1. Tsukihara, T., Aoyama, H., Yamashita, E., Tomizaki, T., Yamaguchi, H., Shinzawaitoh, K., Nakashima, R., Yaono, R., and Yoshikawa, S. (1995) *Science* **269**, 1069-1074.

2. Tsukihara, T., Aoyama, H., Yamashita, E., Tomizaki, T., Yamaguchi, H., Shinzawaltoh, K., Nakashima, R., Yaono, R., and Yoshikawa, S. (1996) *Science* **272**, 1136-1144.

3. Iwata, S., Ostermeier, C., Ludwig, B., and Michel, H. (1995) *Nature* **376**, 660-669.

4. Yoshikawa, S., Shinzawa-Itoh, K., Nakashima, R., Yaono, R., Yamashita, E., Inoue, N., Yao, M., Fei, M. J., Libeu, C. P., Mizushima, T., Yamaguchi, H., Tomizaki, T., and Tsukihara, T. (1998) *Science* **280**, 1723-1729.

5. Proshlyakov, D. A., Pressler, M. A., DeMaso, C., Leykam, J. F., DeWitt, D. L., and Babcock, G. T. (2000) *Science* **290**, 1588-1591.

6. McCauley, K. M., Vrtis, J. M., Dupont, J., and van der Donk, W. A. (2000) *J. Am. Chem. Soc.* **122**, 2403-2404.

7. Greenwood, C., and Gibson, Q. H. (1967) *J Biol Chem* **242**, 1782-1787.

8. Chance, B., Saronio, C., and Leigh, J. S., Jr. (1975) *J Biol Chem* **250**, 9226-9237.

9. Proshlyakov, D. A., Pressler, M. A., and Babcock, G. T. (1998) *Proc. Natl. Acad. Sci. U. S. A.* **95**, 8020-8025.

10. Varotsis, C., and Babcock, G. T. (1990) *Biochemistry* **29**, 7357-7362.

11. Babcock, G. T., and Wikstrom, M. (1992) *Nature* **356**, 301-309.

12. Han, S. H., Ching, Y. C., and Rousseau, D. L. (1990) *Biophys. J.* **57**, A392-A392.

13. Oliveberg, M., Brzezinski, P., and Malmstrom, B. G. (1989) *Biochem. Biophys. Acta* **977**, 322-328.

14. Hallen, S., and Nilsson, T. (1992) *Biochemistry* **31**, 11853-11859.

15. Karpefors, M., Adelroth, P., Namslauer, A., Zhen, Y. J., and Brzezinski, P. (2000) *Biochemistry* **39**, 14664-14669.

16. Babcock, G. T., Jean, J. M., Johnston, L. N., Palmer, G., and Woodruff, W. H. (1984) *J. Am. Chem. Soc.* **106**, 8305-8306.

17. Varotsis, C., Woodruff, W. H., and Babcock, G. T. (1989) *J. Am. Chem. Soc.* **111**, 6439-6440.

18. Han, S., Ching, Y. C., and Rousseau, D. L. (1990) *Proc. Natl. Acad. Sci. U. S. A.* **87**, 2491-2495.

19. Ogura, T., Takahashi, S., Shinzawaitoh, K., Yoshikawa, S., and Kitagawa, T. (1990) *J. Am. Chem. Soc.* **112**, 5630-5631.

20. Varotsis, C., Woodruff, W. H., and Babcock, G. T. (1990) *J. Biol. Chem.* **265**, 11131-11136.

21. Han, S. H., Ching, Y. C., and Rousseau, D. L. (1990) *Biochemistry* **29**, 1380-1384.

22. Wikstrom, M., and Morgan, J. E. (1992) *J Biol Chem* **267**, 10266-10273.

23. Proshlyakov, D. A., Ogura, T., Shinzawaitoh, K., Yoshikawa, S., Appelman, E. H., and Kitagawa, T. (1994) *J. Biol. Chem.* **269**, 29385-29388.

24. Blomberg, M. R. A., Siegbahn, P. E. M., Babcock, G. T., and Wikstrom, M. (2000) *J. Inorg. Biochem.* **80**, 261-269.

25. Varotsis, C., Zhang, Y., Appelman, E. H., and Babcock, G. T. (1993) *Proc. Natl. Acad. Sci. U. S. A.* **90**, 237-241.

26. Han, S. W., Ching, Y. C., and Rousseau, D. L. (1990) *Nature* **348**, 89-90.

27. Ogura, T., Hirota, S., Proshlyakov, D. A., Shinzawaltoh, K., Yoshikawa, S., and Kitagawa, T. (1996) *J. Am. Chem. Soc.* **118**, 5443-5449.

28. Sucheta, A., Szundi, I., and Einarsdottir, O. (1998) *Biochemistry* **37**, 17905-17914.

29. Morgan, J. E., Verkhovsky, M. I., Palmer, G., and Wikstrom, M. (2001) *Biochemistry* **40**, 6882-6892.

30. Morgan, J. E., Verkhovsky, M. I., and Wikstrom, M. (1996) *Biochemistry* **35**, 12235-12240.

31. Kitagawa, T. (2000) *J. Inorg. Biochem.* **82**, 9-18.

32. FergusonMiller, S., and Babcock, G. T. (1996) *Chem. Rev.* **96**, 2889-2907.

33. Han, S., Takahashi, S., and Rousseau, D. L. (2000) *J. Biol. Chem.* **275**, 1910-1919.

34. Proshlyakov, D. A., Ogura, T., Shinzawaltoh, K., Yoshikawa, S., and Kitagawa, T. (1996) *Biochemistry* **35**, 76-82.

35. Han, S. H., Ching, Y. C., and Rousseau, D. L. (1990) *J. Am. Chem. Soc.* **112**, 9445-9451.

36. Ogura, T., Takahashi, S., Hirota, S., Shinzawaitoh, K., Yoshikawa, S., Appelman, E. H., and Kitagawa, T. (1993) *J. Am. Chem. Soc.* **115**, 8527-8536.

37. Ogura, T., Takahashi, S., Shinzawaitoh, K., Yoshikawa, S., and Kitagawa, T. (1990) *J. Biol. Chem.* **265**, 14721-14723.

38. Verkhovsky, M. I., Morgan, J. E., and Wikstrom, M. (1994) *Biochemistry* **33**, 3079-3086.

39. Callahan, P. M., and Babcock, G. T. (1981) *Biochemistry* **20**, 952-958.

40. Babcock, G. T., Callahan, P. M., Ondrias, M. R., and Salmeen, I. (1981) *Biochemistry* **20**, 959-966.

41. Woodruff, W. H. (1993) *J. Bioenerg. Biomembr.* **25**, 177-188.

42. Choi, S., Lee, J. J., Wei, Y. H., and Spiro, T. G. (1983) *J. Am. Chem. Soc.* **105**, 3692-3707.

43. Vansteelandtfrentrup, J., Salmeen, I., and Babcock, G. T. (1981) *J. Am. Chem. Soc.* **103**, 5981-5982.

44. Kitagawa, T., Kyogoku, Y., and Orii, Y. (1977) *Arch. Biochem. Biophys.* **181**, 228-235.

45. Willems, D. L., and Bocian, D. F. (1984) *J. Am. Chem. Soc.* **106**, 880-890.

46. Willems, D. L., and Bocian, D. F. (1985) *J. Phys. Chem.* **89**, 234-239.

47. Ching, Y. C., Argade, P. V., and Rousseau, D. L. (1985) *Biochemistry* **24**, 4938-4946.

48. Ogura, T., Yoshikawa, S., and Kitagawa, T. (1985) *Biochemistry* **24**, 7746-7752.

49. Ogura, T., Yoshikawa, S., and Kitagawa, T. (1985) *Biochim. Biophys. Acta* **832**, 220-223.

74

50. Ogura, T., Yoshikawa, S., and Kitagawa, T. (1989) *Biochemistry* **28**, 8022-8027.

51. Tsubaki, M., Nagai, K., and Kitagawa, T. (1980) *Biochemistry* **19**, 379-385.

52. Argade, P. V., Ching, Y. C., and Rousseau, D. L. (1986) *Biophys. J.* **50**, 613-620.

53. Karpefors, M., Adelroth, P., and Brzezinski, P. (2000) *Biochemistry* **39**, 5045-5050.

54. Sucheta, A., Georgiadis, K. E., and Einarsdottir, O. (1997) *Biochemistry* **36**, 554-565.

55. Kim, Y., Shinzawa-Itoh, K., Yoshikawa, S., and Kitagawa, T. (2001) *J. Am. Chem. Soc.* **123**, 757-758.

56. Han, S., Ching, Y. C., and Rousseau, D. L. (1990) *Proc. Natl. Acad. Sci. U. S. A.* **87**, 8408-8412.

57. Proshlyakov, D. A., Pressler, M. A., and Babcock, G. T. (1999) *J. Inorg. Biochem.* **74**, 267-267.

58. Oertling, W. A., Kean, R. T., Wever, R., and Babcock, G. T. (1990) *Inorg. Chem.* **29**, 2633-2645.

59. Tommos, C., and Babcock, G. T. (2000) *Biochim. Biophys. Acta* **1458**, 199-219..

60. Rich, P. R., Meunier, B., Mitchell, R., and Moody, A. J. (1996) *Biochim. Biophys. Acta-Bioenerg.* **1275**, 91-95.

61. Adar, F., and Yonetani, T. (1978) *Biochim. Biophys. Acta* **502**, 80-86..

62. Kitagawa, T., and Orii, Y. (1978) *J. Biochem. (Tokyo)* **84**, 1245-1252..

63. Salmeen, I., Rimai, L., and Babcock, G. (1978) *Biochemistry* **17**, 800-806.

64. Babcock, G. T., and Salmeen, I. (1979) *Biochemistry* **18**, 2493-2498.

65. Ondrias, M. R., and Babcock, G. T. (1980) *Biochem. Biophys. Res. Commun.* **93**, 29-35.

66. Varotsis, C. A., and Babcock, G. T. (1995) *J. Am. Chem. Soc.* **117**, 11260-11269.

67. Page, C. C., Moser, C. C., Chen, X., and Dutton, P. L. (1999) *Nature* **402**, 47-52.

68. Proshlyakov, D. A., Pressler, M. A., and Babcock, G. T. Unpublished results.

CHAPTER III: Prostaglandin H Synthase

3.1 Introduction

Prostaglandin H synthase (PGHS) is the enzyme that catalyzes the conversion of arachidonic acid into prostaglandin H_2 (PGH_2), which is the precursor of prostaglandins, prostacyclins and thromboxanes (1-4). The biological importance of this enzyme, from a pharmaceutical point of view, is highlighted by the fact that it is the target of nonsteroidal anti-inflammatory drugs (5). The production of PGH_2 is mediated by the formation of the endoperoxide, hydroperoxide prostaglandin G_2 (PGG_2). Figure 3.1 is a schematic representation of the formation of PGH_2 from arachidonic acid (3). Thus, PGHS has two functions: a cyclooxygenase activity, by which it inserts 2 O_2 into arachidonic acid to form PGG_2; and a peroxidase activity, by which it reduces the hydroperoxide to an alcohol, PGH_2. The final product, PGH_2, is then used for the formation of the prostaglandins, prostacyclins, and thromboxanes.

The proposed mechanisms of these reactions are shown in Figure 3.2 (1,6). The conversion of PGG_2 to PGH_2 is catalyzed by the heme active site; this results in the formation of a ferryl-oxo heme intermediate that contains a porphyrin π-cation radical (7-9). This heme intermediate oxidizes a nearby tyrosine, Tyr385, to a radical-containing amino acid (9,10). This tyrosine radical is then involved in the O_2 insertion into arachidonic acid that results in the formation of PGG_2. The peroxidase part of the reaction is carried out by the heme active site, while the cyclooxygenase reaction is performed by Tyr385. Both of these reactions are coupled: the tyrosine radical formation is dependent on the heme radical, while this in turn is produced by the reaction of the hydroperoxide, formed in the cyclooxygenase cycle.

76
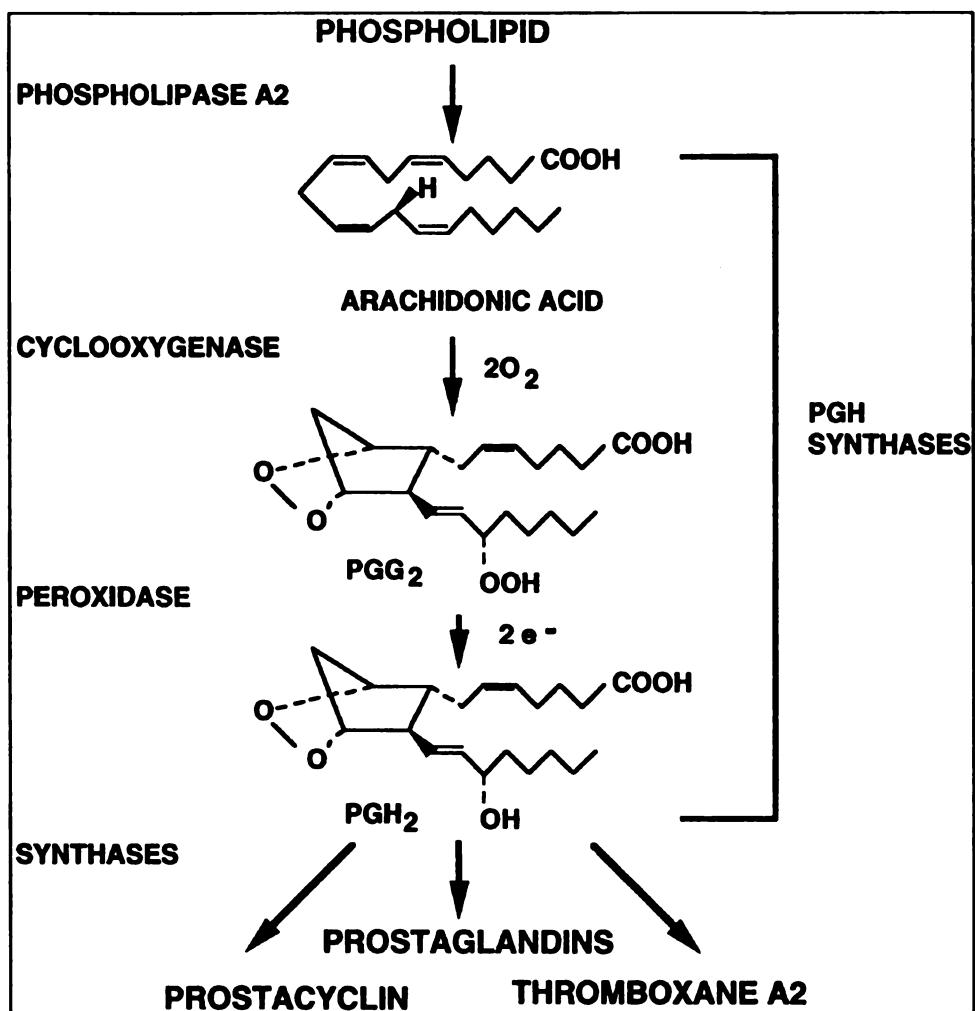
Figure 3.1. The cyclooxygenase and peroxidase reactions of PGHS (obtained from Smith *et al.* (3)).
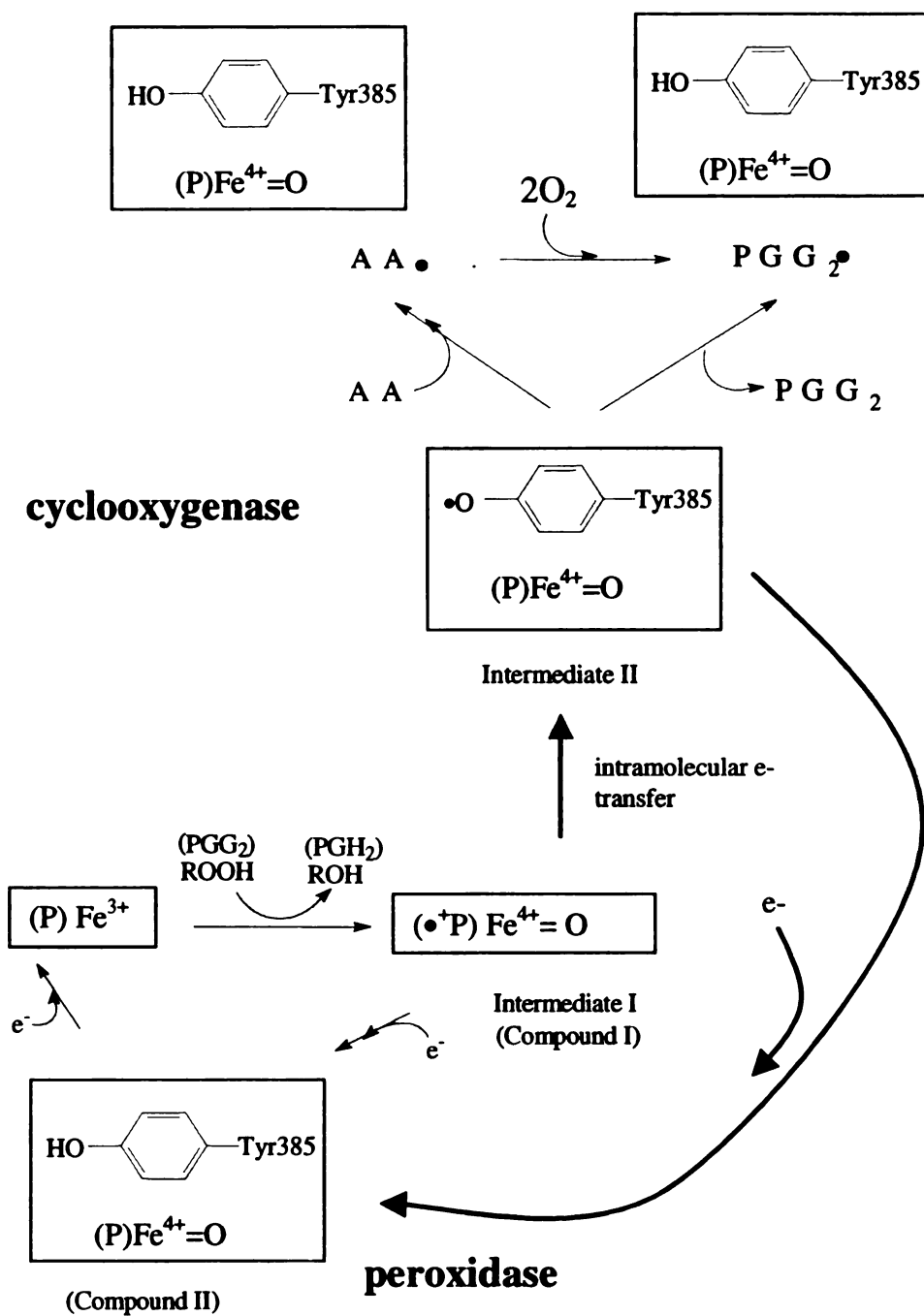
Figure 3.2. Schematic representation of the peroxidase and cyclooxygenase reactions in PGHS. The scheme shows the coupling of these two reactions (adapted from (3)).

78

There are two known forms of PGHS, PGHS-1 and PGHS-2, also known as

COX-1 and COX-2, respectively (2), which have a 60% homology between them and

catalyze the same reactions. COX-2 is best known because it is the target of various

commercial drugs such as Vioxx and Celebrex, used for the treatment of arthritis.

However, of the two isoenzymes, PGHS-1 is easier to obtain from tissue (e.g., from

sheep seminal vesicle microsomes) and most of the studies have been done on this form

of PGHS.

Similar to peroxidases, PGHS can reduce H_2O_2 to H_2O and general peroxide

(ROOH) to alcohol (ROH). Figure 3.3 shows the proposed mechanism by which PGHS-

1 reduces ROOH to ROH (6,11,12). PGHS-1 in its resting state (oxidized) reacts with

peroxide (ROOH) to form an undetected peroxy-bound heme intermediate (peroxy),

which does not accumulate because of the fast O-O splitting that results in the formation

of a ferryl-oxo intermediate. It is proposed (5) that this ferryl-oxo heme intermediate

contains a porphyrin π-cation radical and would be structurally similar to compound I of

heme peroxidases, such as horseradish peroxidase (HRP). The π-cation porphyrin in

PGHS-1 then oxidizes Tyr385 to a radical-containing amino acid, which will be involved

in the cyclooxygenase reaction. This PGHS-1 intermediate is termed Intermediate II, and

would be different from that of the reaction of peroxidases in that the heme is instead

reduced by a substrate and therefore the protein never bears a radical. In the next step,

the radical (Tyr385) is reduced by arachidonic acid and at this stage the protein would be

similar to the second intermediate in peroxidases, so it is labeled as Compound II. This

intermediate is then reduced by an external source, unidentified until now, to its oxidized

resting state.
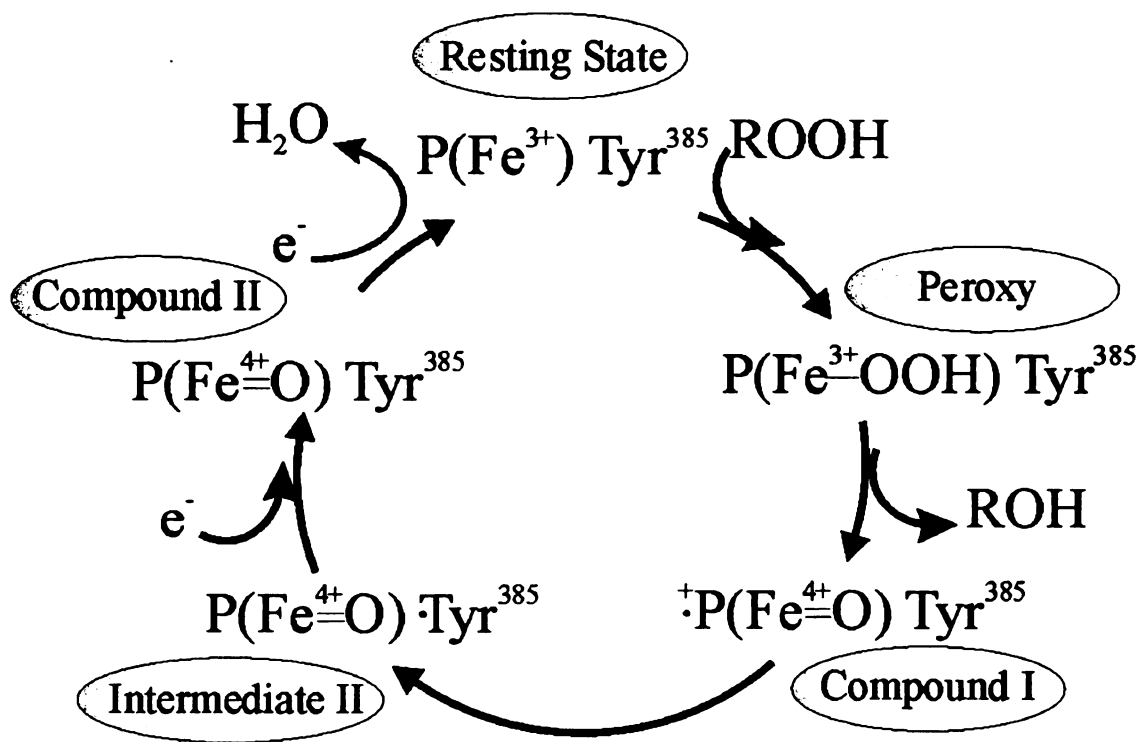
Figure 3.3. Representation of the proposed intermediates that are formed during the reaction between PGHS and a hydroperoxide (adapted from Seibold *et al.* (14)).

PGHS-1 is a homodimer of 70-kDa/subunit, each containing a heme (Fe protoporphyrin–IX) (13). This prosthetic group is needed for the cyclooxygenase and peroxidase activities. When isolated, PGHS-1 is obtained as a 50% holoenzyme: 50% apoenzyme mixture (14). Resonance Raman (RR) spectroscopy and electron paramagnetic resonance (EPR) studies done on heme reconstituted resting PGHS-1 have shown that the heme-bound iron ion is in a ferric six-coordinate state with a mixture of high- and low- spin states (15). Further studies indicated that native heme unreconstituted PHGS-1 in a heme-to-protein ratio of 1-to-4 (0.25 heme/monomer) is ferric, six-coordinate, high-spin state and when reconstituted shows the presence of both high and low spin states (16). The same studies also showed that the ferrous form is a mixture of ferrous, five-coordinate, high-spin state and six-coordinate low-spin state. In addition, they published the low frequency region of the Raman spectrum of the ferrous, five-coordinate state; however, they did not detect an v(Fe-N$_{his}$) mode for PGHS-1.

The heme in PGHS-1 is bound to the protein through a histidine, as first demonstrated by EPR studies (15), and then further confirmed by X-ray crystallography (17). However, its detection, until know, by resonance Raman spectroscopy has not been possible. Moreover, the basicity of its *trans*-ligand is not known, although it is expected to be the same as in other peroxidases. Yet, the heme intermediate that is formed during the peroxidases reaction of PGHS-1, Compound I, is unique in that it oxidizes an amino acid residue instead of oxidizing a substrate, as like other peroxidases.

An indication of the strength of the Fe-N$_{his}$ bond in PGHS-1 can give us more insight on how the protein can control the reactivity of its intermediates. In this regards,

a detailed resonance Raman spectroscopic study on PGHS-1 has been performed and will be reported in this chapter. The goal is to clarify the true nature of the resting state of PGHS-1, i.e., coordination and spin state, as there are conflicting reports on this aspect. The other objective of this study is to detect the $v(Fe-N_{his})$ stretching mode and its value. These results and its implications will then be discussed in comparison to other well known peroxidases.

3.2 Materials and methods

3.2.1 Sample preparation for PGHS-1

Heme-reconstituted PGHS was isolated by Dr. Steve Seibold, as reported in the literature (14). The purified enzyme was dissolved in 50 mM sodium phosphate buffer, pH 7.0, at a final concentration of 15-40 μM (heme). The ferrous enzyme was prepared by adding sodium dithionite to the oxidized sample under an argon atmosphere. The ferrous CO-bound PGHS-1 was prepared by adding CO to the ferrous enzyme. Normal abundance and isotopically enriched CO, $^{13}C^{16}O$, were used for the Raman experiments. The integrity of the samples was monitored by observing the Raman spectra during the measurements and by UV-vis spectroscopy before and after the Raman scattering.

3.2.2 Resonance Raman measurements

The Raman spectra of native, oxidized PGHS-1 and carbon monoxy-bound ferrous PGHS-1 were obtained by excitation at 413.1 nm from a Kr^+ laser (Coherent K-90). The excitation at 434 nm was used for ferrous PGHS-1 and produced by a stilbene dye laser (Coherent CR599), which was pumped by an Ar^+ laser (Coherent Innova 200).

The laser power was 10 mW at the sample, which was contained in a spinning cell at a temperature between 5 and 15°C. The Raman scattering was focused on to the entrance slit of a spectrometer (Spex 1877 Triplemate) and detected with a liquid N_2 cooled CCD detector (EG&G OMA 4, Model 1530-CUV-1024S).

3.3 Results

Figure 3.4 shows the high frequency region (1350-1650 cm^{-1}) of the Raman spectrum of ferric PGHS-1. The strong band at 1370 cm^{-1} is the vibrational mode, v_4, which is known as the oxidation state marker mode. This mode has substantial contribution from the pyrrole C_a-N coordinate in the heme (18). The v_4 mode at 1370 cm^{-1} has a frequency characteristic of ferric heme proteins. The band has no shoulder in the 1355-1360 cm^{-1} region that would indicate the presence of ferrous PGHS-1. The band at 1480 cm^{-1} is v_3 and is indicative of a high-spin Fe^{3+} state. This band has no shoulder in the 1494-1505 cm^{-1} region, which would show the presence of low-spin PGHS-1. The heme skeletal mode, v_2, at 1556 cm^{-1} also confirms the high-spin state of PGHS-1. In addition, it indicates a six-coordinate iron (III); values of v_2 for five-coordinate Fe^{3+} hemes are found near 1570 cm^{-1} (18). The 1623 cm^{-1} band corresponds to the symmetric v(C=C) stretch of the peripheral vinyls (19). The core-size marker, v_{10}, is expected to be at ~1615 cm^{-1} for six-coordinate high-spin hemes, however, the intensity of this mode is small and the band is usually masked by the vinyl modes, when the heme iron is ferric high-spin (18). Table 3.1 compares the frequencies for the Raman bands of PGHS-1 with those of the well-characterized horse heart myoglobin (HHMb).
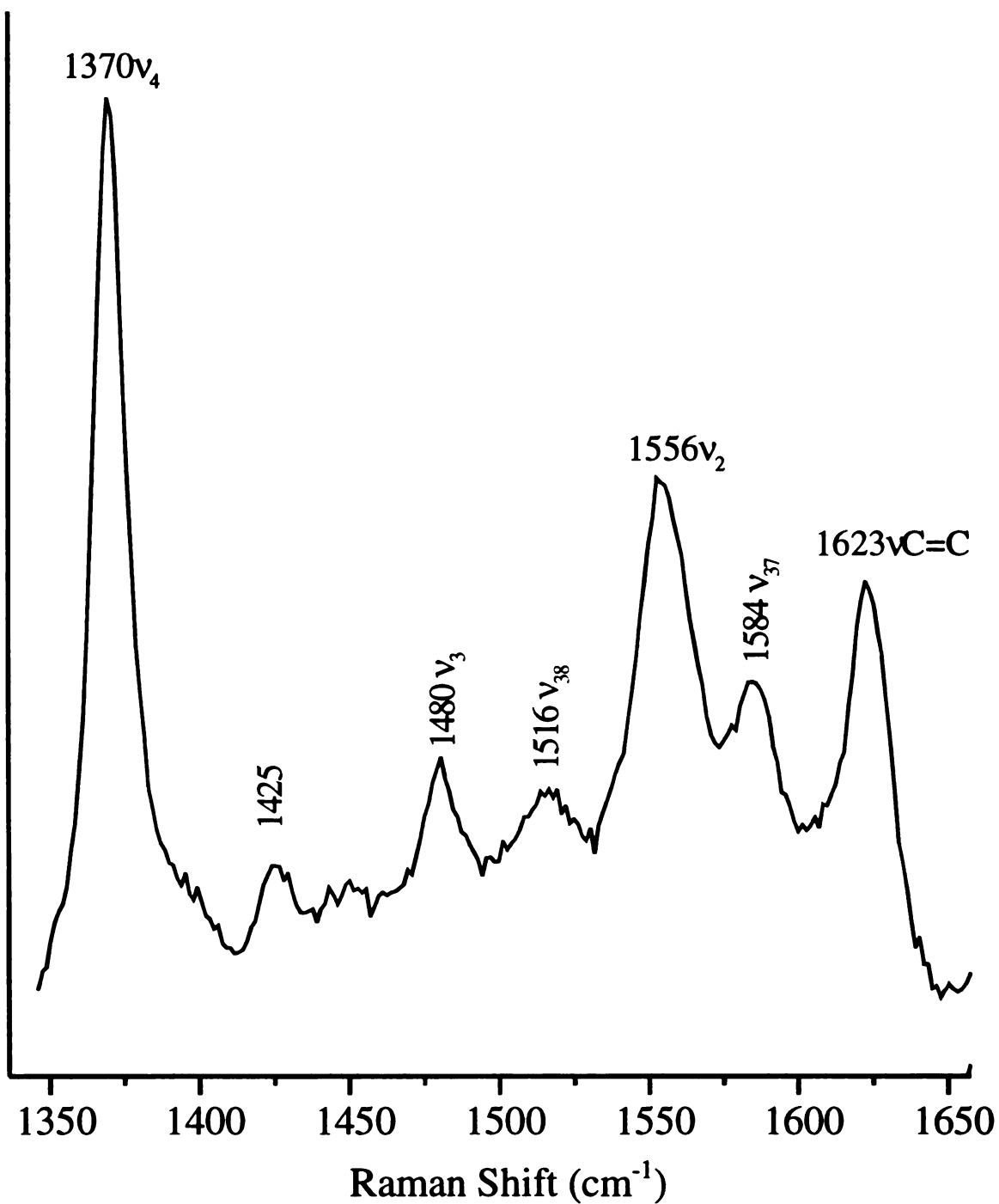
Figure 3.4. High frequency region of the resonance Raman spectrum of oxidized resting PGHS-1.

Table 3.1. Selected core size markers in the high frequency region of PGHS-1 in comparison to horse heart myoglobin (HHMb).

Mode	HHMb(H_2O) (Fe^{3+} 6-c hs)[a]	PGHS-1
$\nu(C=C)_{vinyls}$	1618	1623
ν_{10}	1608	
ν_{37}	1583	1584
ν_2	1563	1556
ν_{19}	1552	
ν_{11}	1543	
ν_{38}	1514	1516
ν_3	1481	1480
ν_{28}	1451	
ν_4	1373	1370

[a]from reference:(19)

abbreviations:

6-c: 6-coordinate, hs- high spin

85

Figure 3.5 displays the high frequency region of the Raman spectrum of dithionite reduced (ferrous high-spin) PGHS-1. The oxidation marker v_4 at 1358 cm^{-1} confirms the ferrous state of the enzyme. In addition, the heme is high-spin as indicated by the core-size markers v_2 and v_3, at 1561 cm^{-1} and 1469 cm^{-1}, respectively (18). Additional confirmation of the spin state is supported by v_{10} at 1605 cm^{-1}. The core size marker bands v_{37} and v_{38} are at 1583 cm^{-1} and 1523 cm^{-1}, respectively. The 1620 cm^{-1} band, in the oxidized spectrum, has downshifted 3 cm^{-1} in the ferrous spectrum. Frequencies from the ferrous PGHS Raman spectra are summarized in Table 3.2.

The low frequency region of the Raman spectra of oxidized (met-aquo), ferrous and CO-bound ferrous PGHS-1 is shown in Figure 3.6. The strong band at 672 cm^{-1}, for all forms, is v_7, which is a mode that involves symmetric pyrrole deformation (18). The band at 375 cm^{-1} is the out-of-plane bending mode of the propionate groups (C C_cC_d – propionates) (19-21). The band at 345 cm^{-1} is v_8, which is a combination of the metal-pyrrole stretch and in-plane substituent bend (21). The two peaks in the CO-bound ferrous spectrum, at 504 and 531 cm^{-1}, correspond to the v(Fe-CO) mode, which will be discussed later.

The small band in the ferrous spectrum at around 216 cm^{-1} is in the region where the Fe-N_{his} stretch is expected to be observed for heme proteins with a proximal histidine (22), see Chapter I. The displacement of the iron from the heme plane appears necessary in conferring Raman activity to the v(Fe-N_{his}) mode(23). With the exception of a few cases, this vibration is not observed for the ferrous low spin or ferric forms in heme proteins or model compounds (mono- and bis imidazole hemes). Since the other spectra do not show any band in this region, the peak at 216 cm^{-1} is assigned to the v(Fe-N_{his})
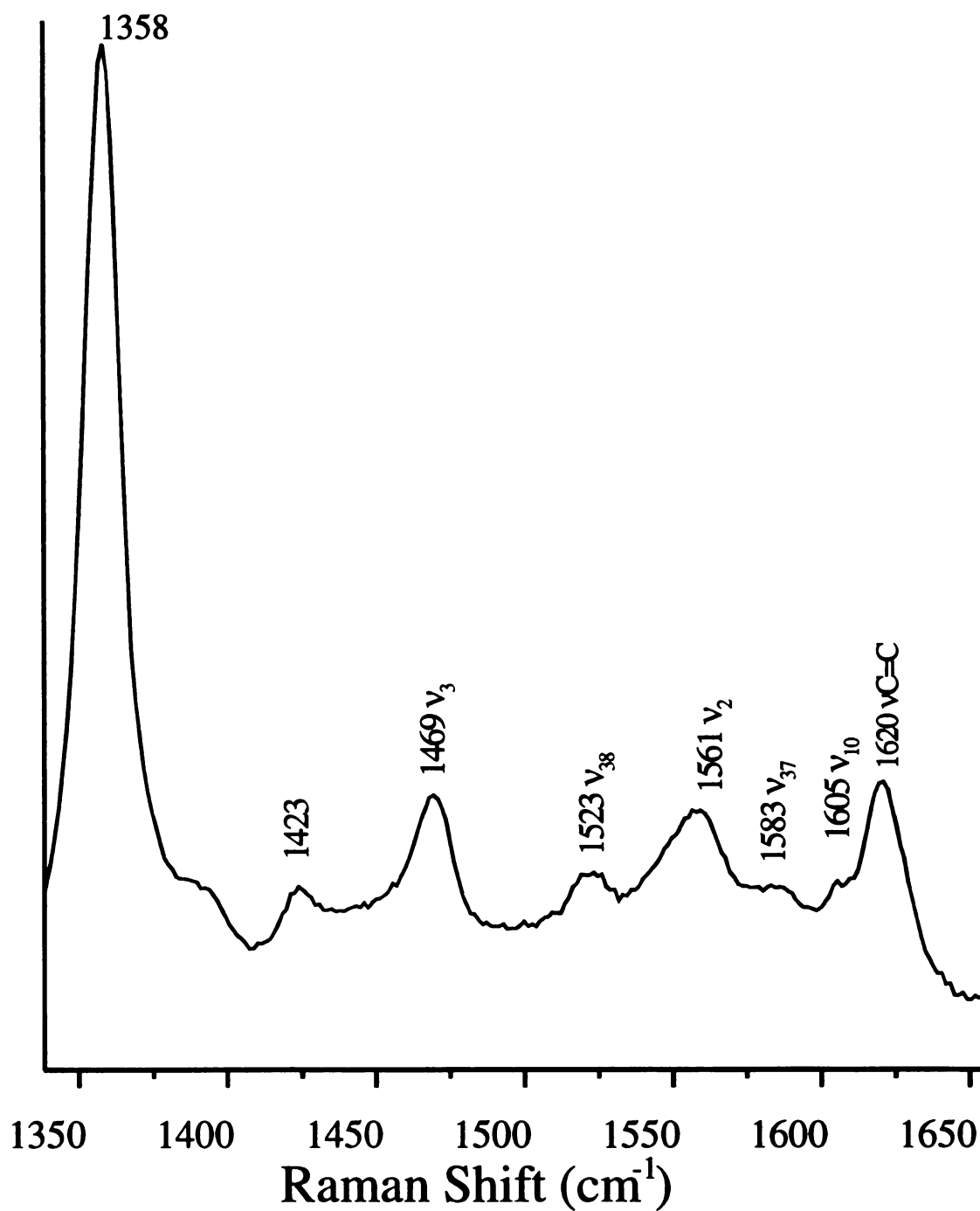
Figure 3.5. High frequency region of the resonance Raman spectrum of the dithionite-reduced (ferrous) PGHS-1.

Table 3.2. Selected core size markers in the high frequency region of PGHS-1 and horse heart myoglobin.

Mode	HHMb (Fe^{2+} 5-c hs)[a]	PGHS-1
$\nu(C=C)_{vinyls}$	1617	1620
ν_{10}	1605	1605
ν_{37}	1583	1583
ν_2	1565	1561
ν_{19}	1552	1555
ν_{11}	1563	
ν_{38}	1522	1523
ν_3	1470	1469
ν_{28}	1446	
ν_4	1355	1358

[a]from reference: (24)

abbreviations:

5-c: 5-coordinate, hs: high spin

stretching mode of PGHS-1. This mode in PGHS-1 is not as intense as those from other heme proteins, were normally the intensity of this vibration is the highest in comparison to other modes in the region below 600 cm^{-1} of the resonance Raman spectrum. In addition, the band appears broader, at least as twice as broad as the v(Fe-N$_{his}$) stretching modes from other proteins. A closer inspection of this band reveals the presence of two peaks centered at 206 and 222 cm^{-1} that are not well resolved in the Raman spectrum.

The low frequency region of the resonance Raman spectra of normal abundance and isotopic CO-bound ferrous PGHS-1 is shown in Figure 3.7. The peaks at 502 and 529 cm^{-1} in the $^{12}C^{16}O$-bound ferrous heme spectrum shift to 497 and 523 cm^{-1} in the $^{13}C^{16}O$-bound ferrous heme spectrum. A shift of ~ 6 cm^{-1} is expected for the v(Fe-CO) stretching mode when $^{12}C^{16}O$ is substituted for $^{13}C^{16}O$ in a heme protein (25). Therefore, the peaks at 502 and 529 cm^{-1} are assigned to the v(Fe-CO) stretching modes of CO-bound ferrous PGHS-1. These two modes indicate two Fe-CO conformers in PGHS-1, which is a similar behavior exhibited by other CO-bound peroxidases (26,27). The intensity of the 502 cm^{-1} mode is smaller than the 529 cm^{-1} peak, although they seem to have the same level in the spectrum in Figure 3.7. However, there is a porphyrin mode at 492 cm^{-1} in the oxidized and ferrous PGHS-1 spectra in Figure 3.6 that may sit under the 502 cm^{-1} peak in the CO-bound ferrous PGHS-1 spectrum. To have an indication of how weak is the 502 cm^{-1} mode of one of the Fe-CO conformer in PGHS-1, higher laser power was used to photolyzed the CO-bound PGHS-1, shown in (Figure 3.8).
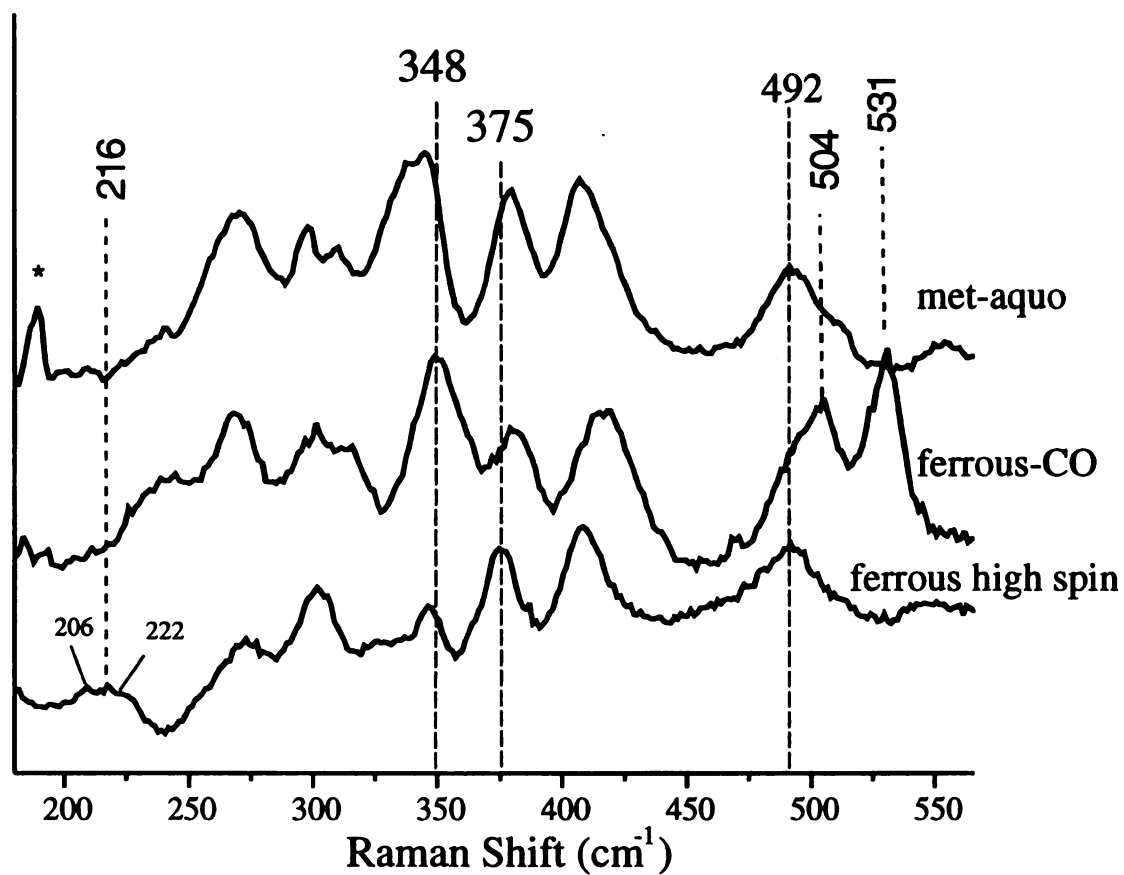
Figure 3.6. Low frequency region of the resonance Raman spectra of ferric-(met-aquo), ferrous-CO, and ferrous high spin PGHS-1.

Figure 3.8 shows that there are changes in the spectrum of PGHS-1-CO as the laser power increases from 1 to 6 mW. In regards to the peaks from the two Fe-CO conformers at 502 and 529 cm^{-1} in the 1-mW spectrum, only the former shifts to 493 cm^{-1} in the 6-mW spectrum. Both peaks have decreased in the 6-mW spectrum because of the photolysis, yet the reason for only one shift is the lower intensity of the 502 cm^{-1} mode, which in addition, is on top of the aforementioned porphyrin mode at 492 cm^{-1}. This indicates that the Fe-CO conformer that is denoted by the peak at 529 cm^{-1} is the major conformer in CO-bound PGHS-1.

The Raman difference spectrum of $^{12}C^{16}O$- and $^{13}C^{16}O$-bound ferrous PGHS-1, from the 1300 to 2000 cm^{-1} region, is shown in the inset of Figure 3.7 as a ($^{12}C^{16}O$-$^{13}C^{16}O$) difference spectrum. The positive peak at 1952 cm^{-1} in this difference spectrum shits to 1909 cm^{-1}, indicated by the negative peak. This shift is typical for the v(C=O) stretching mode of heme proteins (28,29), thus the 1952 cm^{-1} is assigned to the v(C=O) stretching mode of CO-bound ferrous PGHS-1. The 1952 cm^{-1} mode is assigned to the Fe-CO conformer that has a vibration at 529 cm^{-1}. A second v(C=O) stretching mode was not detected in the high region of the Raman spectrum of CO-bound PGHS-1 that would correspond to the 502 cm^{-1} peak in Figure 3.7. The reason for this, in addition to the low population of the Fe-CO conformer denoted by the 502 cm^{-1} peak, is the low intensity of the v(C=O) stretching mode and the low S/N ratio of the spectrum in the high frequency region. This low S/N in the high frequency region is due to the intense fluorescent background of PGHS-1, which has been a problem in other Raman spectroscopic studies (16).
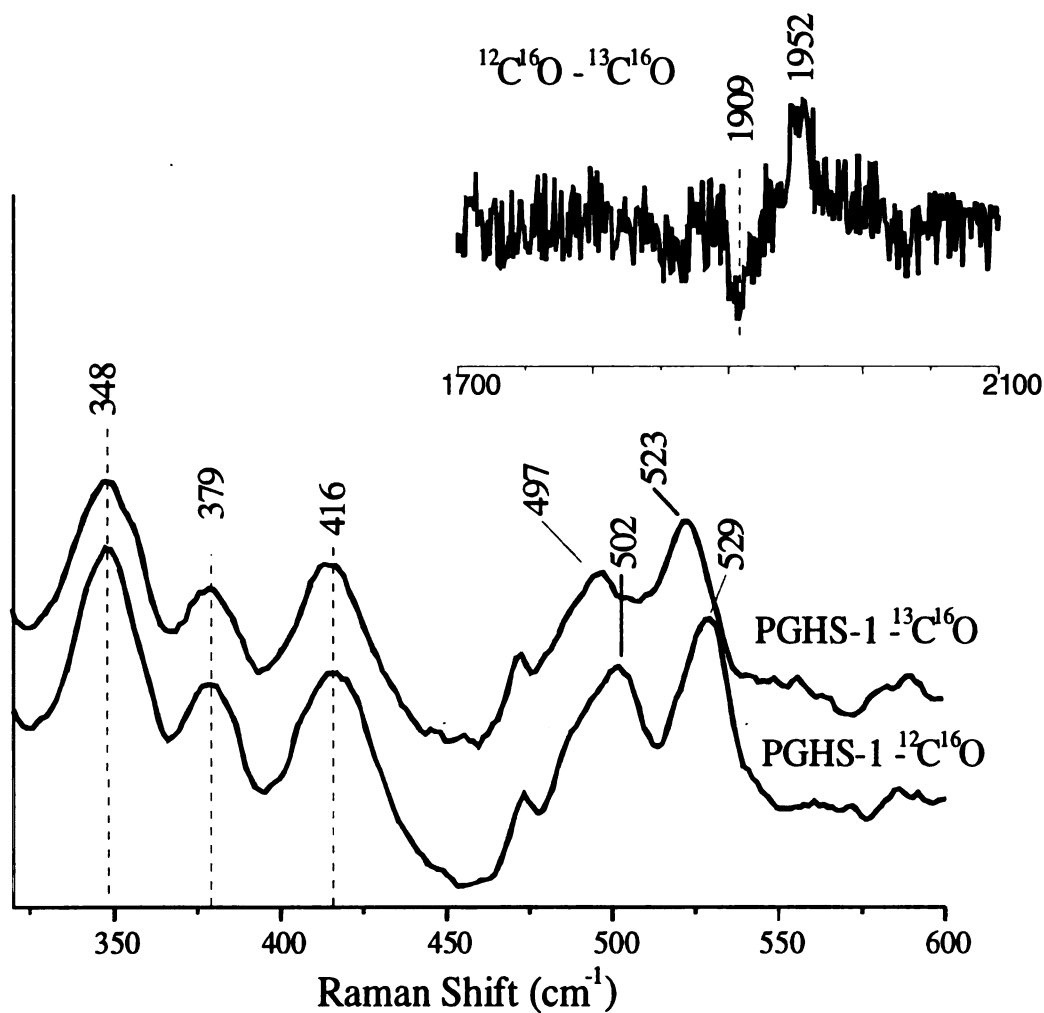
Figure 3.7. High frequency region of the resonance Raman spectra of normal abundance and isotopic CO-bound PGHS-1. The 1700 to 2100 cm^{-1} region, shown in the inset, shows the $^{12}C^{16}O$ - $^{13}C^{16}O$ difference spectrum of CO-bound PGHS-1.

92
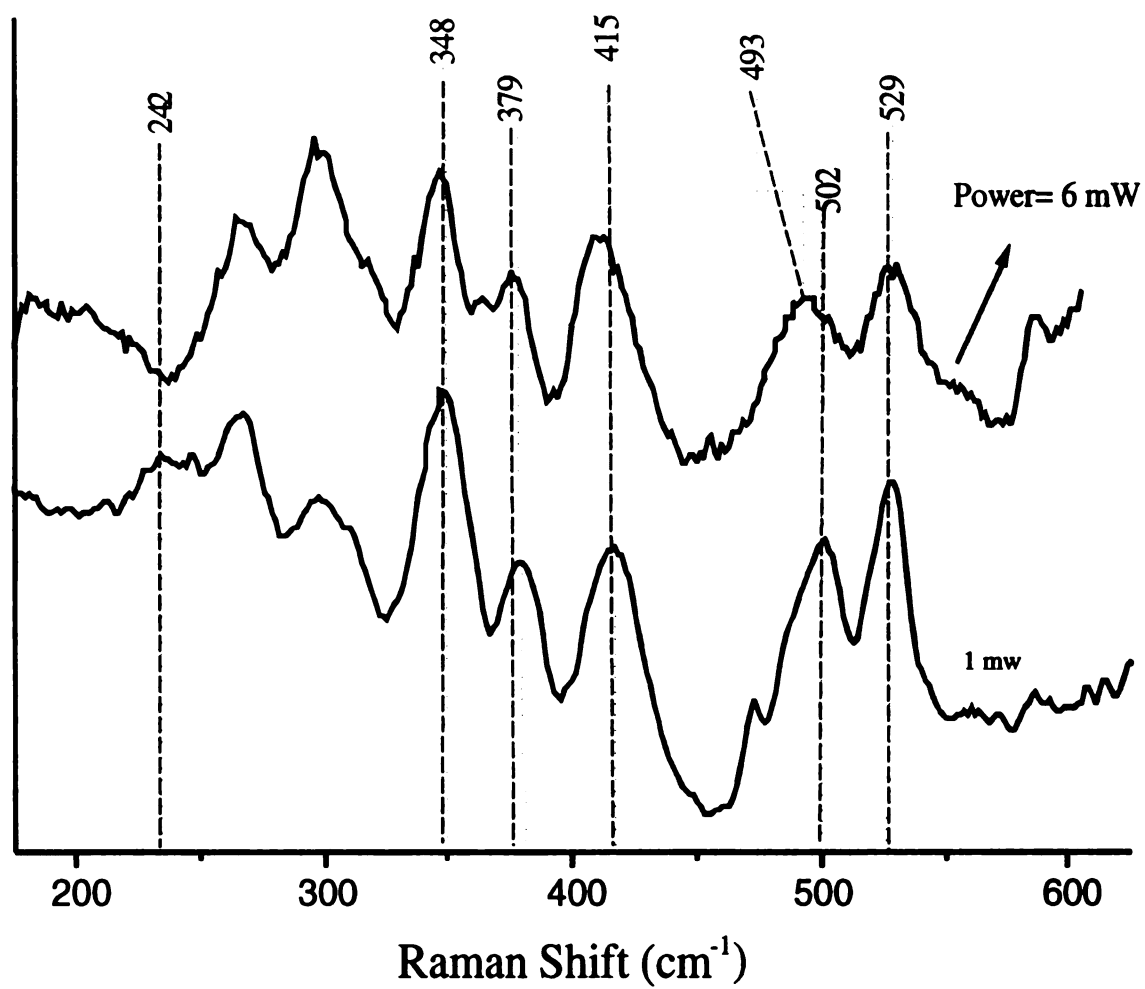
Figure 3.8. Low frequency region of the Raman spectra of CO-bound PGHS-1 at two different laser power, 1 and 6 mW.

3.4 Discussion

The earlier reports on the coordination and spin state of the heme iron in oxidized PGHS-1, were conflicting indicating mixtures of 5- and 6-coordinate and high- and low-spin states for resting PGHS-1 (15). Gaspard and co-workers showed that the Raman spectrum of PGHS-1 is affected by the heme reconstitution procedure (16). In this study, Dr. Steve Seibold carefully performed the heme reconstitution procedure to assure a heme-to-protein ratio of less than 1, in order to avoid non-specific heme binding by the enzyme. This non-specific heme binding results in the formation of various heme conformers that will contribute to the Raman spectrum of the native PGHS-1. The most important mode assignments of the Raman spectrum of oxidized PGHS-1 are compared to oxidized horse heart myoglobin in Table 3.1. The comparison shows that PGHS-1 in its native resting state, is ferric six-coordinate, high-spin, like oxidized horse heart myoglobin. The Raman spectrum did not show any indications of either a 5-coordinate heme, or a mixture of spin states (see Figure 3.4), in agreement with Gaspard and co-workers (16). This is different from the oxidized state of plant peroxidases, which tend to be either ferric 5-coordinate high-spin or in a mixture of ferric 5-coordinate and 6-coordinate high-spin states, as shown in Table 3.3. This table shows that the 6-coordinate state of PGHS-1 is similar to the oxygen-carrier (HHMb) and different from the 5-coordinate state of the peroxidases. The basis for this difference will be discussed towards the end of this section.

94

Table 3.3. Resonance Raman frequency of v_3 for PGHS-1, horse heart myoglobin and various plant peroxidases.[†]

Protein	Resonance Raman v_3 (cm^{-1})	
	6-c hS	5-c hS
CcP		1493
CcP (MI)		1493
APX	1485	<u>1494</u>[‡]
CIP/ARP		1493
HRP-C	1491	<u>1499</u>[‡]
BP1		1492
HHMb (metaquo)	1481	
PGHS-1	1480	

[†]values for the plant peroxidases obtained from:(30)

[‡]the underline denotes the major coordination state conformer

abbreviations:

cytochrome c peroxidase-CcP, cystolic ascorbate peroxidase-APX, *Coprinus cinereus* peroxidase-CIP, *Arthromyces ramosus* peroxidase-ARP, horseradish peroxidase isoenzyme C-HRP-C, barley peroxidase-BP1.

The dithionite-reduced, heme-reconstituted PGHS-1 is ferrous high spin, as indicated by the Raman data and by the comparison of some of the modes between ferrous PGHS-1 and ferrous horse heart myoglobin in Table 3.2. The high frequency region of the spectrum of the reduced enzyme does not indicate formation of low-spin heme in the reconstituted enzyme; this is contrary to the claims of Gaspard and co-workers (16).

The coordination and spin state of the heme iron in the dithionite-reduced PGHS-1 is similar to that of ferrous peroxidases; however, the low frequency region shows differences between these two enzymes. This specifically consists in the much lower $v(Fe-N_{his})$ frequency in PGHS-1 than that of peroxidases. Various $v(Fe-N_{his})$ stretching modes for different proteins are listed and compared to PGHS-1 in Table 3.4. This table shows that the peroxidases have 20 cm^{-1} higher frequency in the $v(Fe-N_{his})$ mode than that of PGHS-1. In fact, PGHS-1 is more like the oxygen-carrier horse heart myoglobin and the cytochrome c peroxidases (CcP) aspartate→asparagine mutant (D235N), which have an $v(Fe-N_{his})$ stretching mode at 205 cm^{-1} (31). Figure 3.9 shows the X-ray crystallographic structure of the heme site of CcP, solved by Wang and co-workers (32). The residues Asp235, His175, Arg48, and His52, are highly conserved in plant peroxidases (30). The distal site of CcP is mainly composed by the His52-Arg48 couple, while the proximal site is characterized by the strong hydrogen bonding between the proximal histidine (His175) and Asp235. This strong hydrogen bonding imparts an anionic character to the imidazole ring of the proximal histidine, i.e. a hisitidinate or imidazolate residue. The imidazolate character of the proximal histidine in peroxidases makes it a stronger ligand that results in a stronger $Fe-N_{his}$ bond than that of myoglobins

96

and hemoglobins, which lack the strong hydrogen bonding between their proximal

histidine and a nearby residue (22). This effect is clearly demonstrated in heme model

compounds, where the v(Fe-N$_{his}$) stretching mode is affected by the charge of the

proximal imidazole (22). Table 3.3 lists the v(Fe-N$_{his}$) stretching modes of Fe^{2+}(OEP)-

2MeIm and Fe^{2+}(OEP)-2MeIm$^-$. When the compound contains the imidazolate ligand,

the vibration is at 233 cm^{-1}, on the other hand, when neutral, the mode shifts to 208 cm^{-1}.

This is the basis for the 20 cm^{-1} difference in the v(Fe-N$_{his}$) stretching modes between

peroxidases and oxygen-carriers. The loss of the strong hydrogen bonding between the

proximal ligand and a nearby residue results in an v(Fe-N$_{his}$) shift from 240 cm^{-1}, in wild

type CcP, to 205 cm^{-1} in the CcP (D235N) mutant. This means that PGHS-1, with v(Fe-

N$_{his}$) modes at 206 and 222 cm^{-1}, lacks this strong hydrogen bonding between the

proximal histidine and a nearby residue and therefore has a weaker proximal ligand than

those from peroxidases. Further indications of a weak proximal ligand in PGHS-1 is

given by the v(Fe-CO) and v(C=O) stretching mode correlation. The values of the v(Fe-

CO) and v(C=O) stretching modes at 529 and 1952 cm^{-1}, respectively, puts PGHS-1 in

the group of heme proteins and model compounds with weak proximal ligands in the

correlation curve shown in Chapter I, Figure 1.5. In addition, Hans *et al.* (33) showed

that PGHS-1 forms 5-coordinate NO-bound heme when reacted with nitrogen oxide (NO)

instead of a 6-coordinate NO-bound complex, which is formed with heme proteins that

have an v(Fe-N$_{his}$) stretching mode greater than 210 cm^{-1}. This is further evidence of the

weak proximal ligand in PGHS-1. The X-ray crystallographic structure of PGHS-1,

reported by Seibold *et al.* (14) shows that the residue position next to the proximal

histidine, which is normally occupied by an aspartate in peroxidases, is occupied by a

water molecule. The missing aspartate in PGHS-1 imparts a more neutral imidazole character on the histidine, which results in a weaker $Fe-N_{his}$ bond, as in hemoglobins and myoglobins.

Various studies done on mutated peroxidases, which lack the strong hydrogen bonding between the proximal ligand and the aspartate, show similarities with PGHS-1. In CcP, when Asp235 is mutated to an asparagine, the protein is not only affected by the changes in the $Fe-N_{his}$ bond, but it also changes from a ferric 5-coordinate heme to a six-coordinate heme complex (34,35). This was also observed in study done by Newmyer *et al.* (36) on mutated HRP. In this work, the proximal histidine was substituted by an alanine residue and then free imidazole was added to form a heme protein with a weak proximal ligand. This substitution resulted in a lower $v(Fe-N_{his})$ mode and the formation of a six-coordinate ferric heme, different from the ferric 5-coordinate complex of the resting wild type enzyme. In addition, it was shown in this same study that the rate of the reaction between the mutant HRP with the unencumbered proximal imidazole and H_2O_2 is $1 \times 10^4 \, M^{-1}s^{-1}$, 3 orders of magnitude slower than the reaction of the wild-type enzyme. The authors explained that the strong hydrogen bonding in the wild type HRP tethers the heme iron in such manner that it does not bind to any of the surrounding water molecules. Therefore, the peroxidases in their resting state tend to be ferric 5-coordinate. The disrupted interaction between the proximal histidine and the nearby aspartate in resting-state peroxidases results in the binding of a water molecules that are normally located in the heme distal site to the heme iron, which otherwise would normally be tethered. Thus, this affects the peroxidase reaction because the binding affinity of H_2O_2 is comparable to

that of water; this problem is circumvented in normal peroxidase for which water does not bind to the tethered heme iron.

The rate of reaction between PGHS-1 and H_2O_2 is ~ $1 \times 10^4 \, M^{-1}s^{-1}$, similar to the rate of the HRP mutant (36). The reason for this can be explained by using similar arguments used by Newmyer et al. (36). As mentioned before, PGHS-1 is ferric six-coordinate, which means that a water molecule is coordinated to the heme iron. This indeed affects the reaction of PGHS-1 and H_2O_2, however, since the physiological substrate is an organic peroxide (PGG_2), the rate is 3 orders of magnitude faster because of the greater binding affinity of the organic peroxides. Various studies have shown that PGHS-1 self-inactivates after prolonged cyclooxygenase reaction (7,37-39). It is believed that this suicide inactivation is caused by radical migration from Tyr385. This would imply that the water-bound PGHS-1 does not spontaneously react with intracellular sporadic H_2O_2, which would result in the formation of Compound I, which in turn oxidizes Tyr385. Thus, inadvertent formation of a radical is avoided by protecting the heme iron with a water-bound heme in PGHS-1. Although we may understand the differences in the coordination of the heme iron between PGHS-1 and peroxidases, the consequences of a weaker proximal histidine will be next discussed in terms of the O-O bond cleavage during the peroxidase reaction of PGHS-1.

Dawson proposed a mechanism by which peroxidases split the O-O bond (40). This is known as the "push-pull" mechanism, in which the strong imidazolate provides an electronic push to the H_2O_2-bound heme iron, while the His-Arg couple provides the pull. These distal and proximal arrangements of peroxidases would result in a more effective way of O-O cleavage by a heme protein that can otherwise act as an oxygen-carrier such

as myoglobin. However, lately, there have been reports of heme proteins that can act as peroxidases, but have weakened Fe-N_{his} bond (36,41). Thus, now there is a consensus, that the imidazolate character of peroxidases imparts stability to the ferryl-oxo intermediates that are formed during the reaction (41). The anionic charge of the proximal histidine in peroxidases stabilizes better, than neutral histidine, the higher oxidation states of the heme iron. This means that Compound I in PGHS-1 is less stable than that of peroxidases. Evidence of this, comes from the E^o (Fe^{3+}/Fe^{2+}) reducing potentials. PGHS-1 has a E^o (Fe^{3+}/Fe^{2+}) reducing potential of -50 mV, similarly close to that of myoglobin (50 mV), while peroxidases have values ~ -250 mV (15). According to these values, it is expected that the ferryl-oxo intermediates in peroxidases are less oxidizing than the oxo ferryl heme intermediates in PGHS-1. The significance of this is shown in Figure 3.10. The more oxidizing Compound I in PGHS-1 would easily be reduced by Tyr385, which will then be involved in the cyclooxygenase reaction. In the peroxidases, Compound I is more stable and therefore longer-lived, which would be advantageous to avoid the formation of a protein radical before it is reduced by the substrate. This has been shown to occur in the reaction of ferric myoglobin with H_2O_2, where Compound I is short-lived and immediately decays to Compound II with the formation of a protein radical (42,43). The formation of a protein radical does not serve any purpose to normal peroxidases; on the other hand, PGHS-1 uses this radical for its cyclooxygenase activity.

Table 3.4. Frequency of the Fe^{2+}-N(his) bond in heme proteins and model compounds.

Protein	$\nu(Fe^{2+}-N_{his})$ (cm^{-1})
HRP[a]	243
CcP[b]	240
CcP (D235N)[b]	205
MPO[c]	248
Mb[d]	219
Fe^{2+}(OEP)-2MeIm [a]	208
Fe^{2+}(OEP)-2MeIm⁻ [a]	233
PGHS-1	206, 222

[a]obtained from reference: (22)

[b]obtained from reference: (35)

[c]obtained from reference: (44)

abbreviations:

Mb: myoglobin, MPO: myeloperoxidase, OEP: octaethylpoprphyrin, 2MeIm: 2-methyl imidazole.
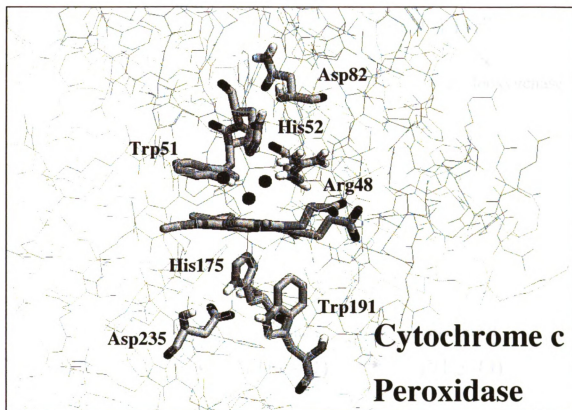
Figure 3.9. The X-ray crystallographic structure of the heme pocket of cytochrome c peroxidase (from reference (32)).

peroxidase

PGHS-1

Resting State — Compound I — Intermediate II

$$P(Fe^{3+})\ Tyr^{385} \xrightarrow[ROH]{ROOH} {}^{\bullet}_{+}P(Fe^{4+}{=}O)\ Tyr^{385} \longrightarrow P(Fe^{4+}{=}O)\ Tyr^{385}$$

cyclooxygenase

6-c hs
$E^0(Fe^{3+}/Fe^{2+}) = -50\ mV$

peroxidases

Resting State — Compound I — Compound II

$$P(Fe^{3+}) \xrightarrow[H_2O]{HOOH} {}^{\bullet}_{+}P(Fe^{4+}{=}O) \xrightarrow[{}^{\bullet}AH]{AH_2} P(Fe^{4+}{=}O)$$

5-c hs
$E^0(Fe^{3+}/Fe^{2+}) = -250\ mV$
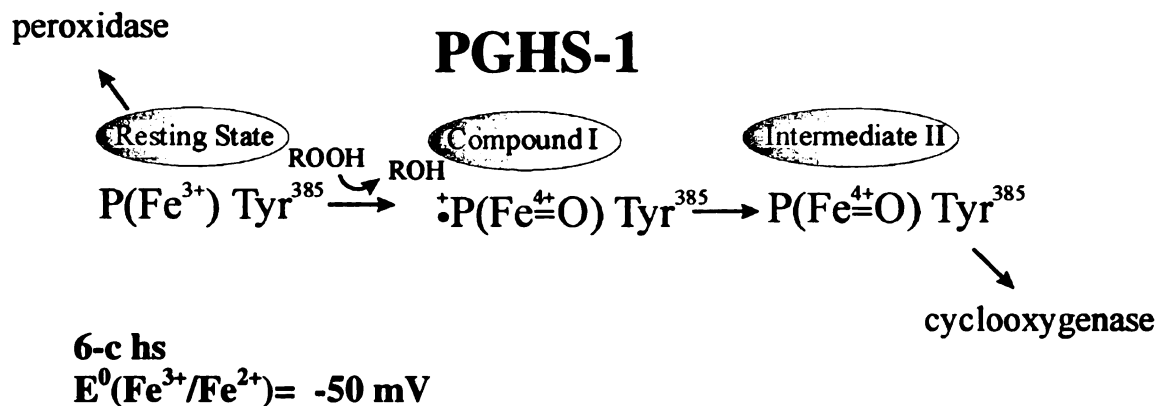
Figure 3.10. The intermediates that are formed in the peroxidase reaction of PGHS-1 (top), while the bottom part of the figure shows the steps that lead to the formation of Compound I and II in other known peroxidases.

3.5 Literature Cited

1. Smith, W. L., DeWitt, D. L., and Garavito, R. M. (2000) *Annu. Rev. Biochem.* **69**, 145-182.

2. Marnett, L. J., Rowlinson, S. W., Goodwin, D. C., Kalgutkar, A. S., and Lanzo, C. A. (1999) *J. Biol. Chem.* **274**, 22903-22906.

3. Smith, W. L., Garavito, R. M., and DeWitt, D. L. (1996) *J. Biol. Chem.* **271**, 33157-33160.

4. Smith, W. L., Garavito, R. M., and DeWitt, D. L. (1996) *Faseb J.* **10**, 1303-1303.

5. Smith, W. L., and Marnett, L. J. (1991) *Biochim. Biophys. Acta* **1083**, 1-17.

6. Tsai, A. L., Wu, G., Palmer, G., Bambai, B., Koehn, J. A., Marshall, P. J., and Kulmacz, R. J. (1999) *J. Biol. Chem.* **274**, 21695-21700.

7. Wu, G., Wei, C. H., Kulmacz, R. J., Osawa, Y., and Tsai, A. L. (1999) *J. Biol. Chem.* **274**, 9231-9237.

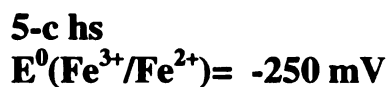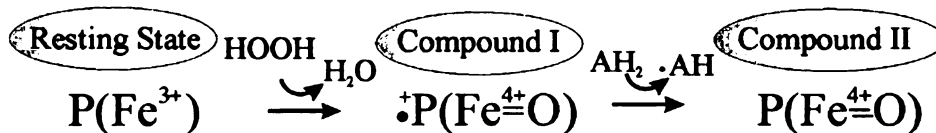8. Lu, G. Q., Tsai, A. L., Van Wart, H. E., and Kulmacz, R. J. (1999) *J. Biol. Chem.* **274**, 16162-16167.

9. Shi, W. J., Hoganson, C. W., Espe, M., Bender, C. J., Babcock, G. T., Palmer, G., Kulmacz, R. J., and Tsai, A. L. (2000) *Biochemistry* **39**, 4112-4121.

10. Tsai, A. L., Kulmacz, R. J., and Palmer, G. (1995) *J. Biol. Chem.* **270**, 10503-10508.

11. Dietz, R., Nastainczyk, W., and Ruf, H. H. (1988) *Eur. J. Biochem.* **171**, 321-328.

12. Karthein, R., Dietz, R., Nastainczyk, W., and Ruf, H. H. (1988) *Eur. J. Biochem.* **171**, 313-320.

13. Picot, D., and Garavito, R. M. (1994) *FEBS Lett.* **346**, 21-25.

14. Seibold, S. A., Cerda, J. F., Mulichak, A. M., Song, I. S., Garavito, R. M., Arakawa, T., Smith, W. L., and Babcock, G. T. (2000) *Biochemistry* **39**, 6616-6624.

15. Tsai, A. L., Kulmacz, R. J., Wang, J. S., Wang, Y., Vanwart, H. E., and Palmer, G. (1993) *J. Biol. Chem.* **268**, 8554-8563.

16. Gaspard, S., Chottard, G., Mahy, J. P., and Mansuy, D. (1996) *Eur. J. Biochem.* **238**, 529-537.

17. Picot, D., Loll, P. J., and Garavito, R. M. (1994) *Nature* **367**, 243-249.

18. Spiro, T. G., and Li, X.-Y. (1988) in *Biological Applications of Raman Spectroscopy* (Spiro, T. G., ed) Vol. 3, pp. 1-38, 3 vols., John Wiley & Sons.

19. Hu, S. Z., Smith, K. M., and Spiro, T. G. (1996) *J. Am. Chem. Soc.* **118**, 12638-12646.

20. Hu, S. Z., Morris, I. K., Singh, J. P., Smith, K. M., and Spiro, T. G. (1993) *J. Am. Chem. Soc.* **115**, 12446-12458.

21. Choi, S. H., and Spiro, T. G. (1983) *J. Am. Chem. Soc.* **105**, 3683-3692.

22. Kitagawa, T. (1988) in *Biologial Applications of Raman Spectroscopy* (Spiro, T. G., ed) Vol. 3, pp. 97-132, 3 vols., John Wiley & Sons.

23. Stavrov, S. S. (1993) *Biophys. J.* **65**, 1942-1950.

24. Smulevich, G., Mantini, A. R., Paoli, M., Coletta, M., and Geraci, G. (1995) *Biochemistry* **34**, 7507-7516.

25. Kerr, E. A., and Yu, N. T. (1988) in *Biological Applications of Raman Spectroscopy* (Spiro, T. G., ed) Vol. 3, pp. 39-96, 3 vols., John Wiley & Sons.

26. Smulevich, G., Evangelistakirkup, R., English, A., and Spiro, T. G. (1986) *J. Mol. Struct.* **141**, 411-414.

27. Evangelistakirkup, R., Smulevich, G., and Spiro, T. G. (1986) *Biochemistry* **25**, 4420-4425.

28. Wang, J. L., Takahashi, S., and Rousseau, D. L. (1995) *Proc. Natl. Acad. Sci. U. S. A.* **92**, 9402-9406.

29. Ray, G. B., Li, X. Y., Ibers, J. A., Sessler, J. L., and Spiro, T. G. (1994) *J. Am. Chem. Soc.* **116**, 162-176.

30. Smulevich, G. (1998) *Biospectroscopy* **4**, S3-S17.

31. Smulevich, G., Miller, M. A., Kraut, J., and Spiro, T. G. (1991) *Biochemistry* **30**, 9546-9558.

32. Wang, J. M., Mauro, J. M., Edwards, S. L., Oatley, S. J., Fishel, L. A., Ashford, V. A., Xuong, N. H., and Kraut, J. (1990) *Biochemistry* **29**, 7160-7173.

33. Schelvis, J. P. M., Seibold, S. A., Cerda, J. F., Garavito, R. M., and Babcock, G. T. (2000) *J. Phys. Chem. B* **104**, 10844-10850.

34. Smulevich, G., Neri, F., Marzocchi, M. P., and Welinder, K. G. (1996) *Biochemistry* **35**, 10576-10585.

35. Smulevich, G., Mauro, J. M., Fishel, L. A., English, A. M., Kraut, J., and Spiro, T. G. (1988) *Biochemistry* **27**, 5486-5492.

36. Newmyer, S. L., Sun, J., Loehr, T. M., and deMontellano, P. R. O. (1996) *Biochemistry* **35**, 12788-12795.

37. Wu, G., Wei, C., Kulmacz, R. J., Osawa, Y., and Tsai, A. L. (1999) *Faseb J.* **13**, A1439-A1439.

38. Wu, G., Vuletich, J. L., Kulmacz, R. J., Osawa, Y., and Tsai, A. L. (2001) *J. Biol. Chem.* **276**, 19879-19888.

39. Wu, G., Vuletich, J. L., Kulmacz, R. J., Osawa, Y., and Tsai, A. L. (2000) *Faseb J.* **14**, 614.

40. Dawson, J. H. (1988) *Science* **240**, 433-439.

41. Poulos, T. L. (1996) *J. Biol. Inorg. Chem.* **1**, 356-359.

42. Egawa, T., Shimada, H., and Ishimura, Y. (2000) *J Biol Chem* **275**, 34858-34866.

43. Brittain, T., Baker, A. R., Butler, C. S., Little, R. H., Lowe, D. J., Greenwood, C., and Watmough, N. J. (1997) *Biochem J* **326**, 109-115..

44. Oertling, W. A., Kean, R. T., Wever, R., and Babcock, G. T. (1990) *Inorg. Chem.* **29**, 2633-2645.

CHAPTER IV: Histidine Rich Protein II

4.1 Introduction

Malaria is produced by the parasite *Plasmodium falciparum*. This bacterium

invades the host red blood cells and digests hemoglobin in an acidified vacuole. Aspartic

and cysteine proteases are involved in the digestion of hemoglobin, but cannot degrade

the heme (1-3). The released free heme is toxic to the bacterium because it interferes

with the regulation of the biosynthesis of other proteins. Heme oxygenase is a protein

that can catabolize porphyrins, however this enzyme is not found in the malaria parasite.

Devoid of such a heme-digestive protein, the parasite aggregates the free heme into an

insoluble, inert, crystalline polymer called the malaria pigment or hemozoin. Various

groups have studied hemozoin (2,4,5) and concluded that this polymer is structurally

similar to β-hematin, a heme polymer spontaneously formed when hematin (Fe

protoporphyrin-IX OH) is treated under nonphysiological conditions. The polymer is

formed by the coordination of the propionate oxygen of one heme to the ferric ion of the

next heme. It was thought that hemozoin, under physiological conditions, was produced

by an enzyme, which remained elusive until recently where it has been identified as

HRP-II (1). Histidine rich protein (known as HRP-II, but termed $HR_{ich}P$ in this thesis)

has been found in the digestive vacuole of the parasite. Recombinant $HR_{ich}P$ has been

shown to promote the synthesis of hemozoin at an optimal pH of 4.0 (1). This enzyme

contains 51 repeating units of his-his-ala that constitutes 76% of the protein.

The role of $HR_{ich}P$-II in hemozoin formation is not yet understood. This protein

can bind 50 hemes to form a stable heme bound protein at pH 7.0 (6). The properties of

the heme bound $HR_{ich}P$-II has been studied by using resonance Raman spectroscopy and

will be discussed in this chapter. In this work, the effects of the anti-malarial drug on the heme bound $HR_{ich}P$-II, has also been investigated and such findings will also form part of the discussions in this thesis.

4.2 Materials and methods

4.2.1 Sample preparation for $HR_{ich}P$-II

$HR_{ich}P$ was purified and prepared by Clara Choi as reported in the literature (6). The concentration of the enzyme was 40 µM (heme) after dissolving it in 100 mM Hepes (pH 7.0 or pH 9.0), while the same enzyme was dissolved in 100 mM MES at pH 5.5. Ferrous $HR_{ich}P$ was prepared by adding sodium dithionite to the oxidized sample under an argon atmosphere. The normal abundance carbon monoxide complex ($^{12}C^{16}O$) was prepared by adding CO to the ferrous $HR_{ich}P$ at pH 5.5, 7.0 and 9.0. The isotopically labeled carbon monoxide complex ($^{13}C^{18}O$) was prepared in the same way as the normal abundance CO derivative. The integrity of the samples was monitored by observing the Raman spectra during the measurements and by UV-vis spectroscopy before and after the Raman scattering. Formation of the complexes was confirmed by UV-vis spectroscopy. Native $HR_{ich}P$ have a Soret band at 414 nm, while the dithionite-reduced form is at 424 nm. Ferrous $HR_{ich}P$-bound CO has a Soret at 423 nm.

4.2.2 Resonance Raman measurements

The Raman spectra of oxidized $HR_{ich}P$ and of the carbon monoxy form of $HR_{ich}P$ were obtained by excitation at 413.1 nm from a Kr^+ laser (Coherent K-90). In the experiments in which the protein sample was incubated with chloroquine, excitation was

done at 363.6 nm, obtained from an Ar^+ laser. The spectra of the dithionite-reduced, histidine rich protein were obtained by laser excitation at 422 nm produced by a stilbene dye laser (Coherent CR599), which was pumped by an Ar^+ laser (Coherent Innova 200). The laser power was 10mW at the sample, each of which was contained in a spinning cell at a temperature between 5 and 15°C. The Raman scattering was focused on to the entrance slit of a spectrometer (Spex 1877 Triplemate) and detected with a liquid N_2 cooled CCD detector (EG&G OMA 4, Model 1530-CUV-1024S).

4.3 Results

Figure 4.1 shows the resonance Raman spectrum of oxidized $HR_{ich}P$. The core size markers v_4, v_3 and v_2 are at 1376 cm^{-1}, 1506 cm^{-1} and 1580 cm^{-1}, respectively, and are in accordance to similar assignments made in other heme proteins and model compounds (7-11). These bands indicate that oxidized heme-bound $HR_{ich}P$-II is ferric, six-coordinate low-spin state. The modes, v_{38} and v_{37} at 1552 cm^{-1} and 1601 cm^{-1}, respectively, are also indications of ferric low spin heme. The 1620 cm^{-1} to 1640 cm^{-1} region contains three bands. The peak at 1640 cm^{-1} corresponds to mode v_{10}, a value expected for ferric low spin iron. The other two bands are the $v(C=C)$ stretch of the vinyls, which clearly show two conformations. Resonance Raman spectra of various heme proteins and heme models have shown that the peripheral vinyls- 2 and -4 can conjugate to the heme in two distinct conformers (12,13). The vinyl closest to an in-plane heme conformation will have the lowest $v(C=C)$ stretching frequency (14,15). The axial ligands in $HR_{ich}P$-II have not been identified yet, but because of the high content of

histidines, these are a good candidate as residues that bind to both sides of the heme iron. Results for ferric $HR_{ich}P$-II are tabulated in Table 4.1.

The high frequency region of the Raman spectrum of the dithionite reduced $HR_{ich}P$ is shown in Figure 4.2. The oxidation state marker v_4 is at 1360 cm^{-1}, which is 2-5 cm^{-1} higher than ferrous, high-spin heme proteins. Moreover, the modes v_3 and v_2, at 1494 cm^{-1} and 1582 cm^{-1}, respectively, indicate ferrous, low-spin heme. The intensity of the 1470 cm^{-1} band is rather high and may indicate the presence of ferrous, high-spin heme. Evidence for mixed spin states, in ferrous $HR_{ich}P$ comes from the comparison between the Raman spectra at different pH values. Figure 4.3 displays the Raman spectra of $HR_{ich}P$ at pH 6.0 and at pH 9.0. The spectrum at pH 9.0 (Figure 4.3-b) shows that the relative intensity of the 1470 cm^{-1} peak is much is lower than the peak at 1494 cm^{-1}, in comparison to the Raman spectrum at pH 6.0 (Figure 4.3-a). This means that the high spin conformation is more populated at lower pH. Further evidence of changes in the heme state comes from the UV-vis spectra shown in the insets in Figure 4.3. At pH 6.0, the Soret band is split, with maximas at ~ 386 and 422 nm, while at pH 9.0 the UV-vis spectrum only shows one Soret band at 426 nm. The absorption at 386 nm is due to free heme, an indication that heme loss occurs at pH < 7.0. Table 4.2 lists the mode assignments for the dithionite reduced $HR_{ich}P$-II in comparison to other model compounds.
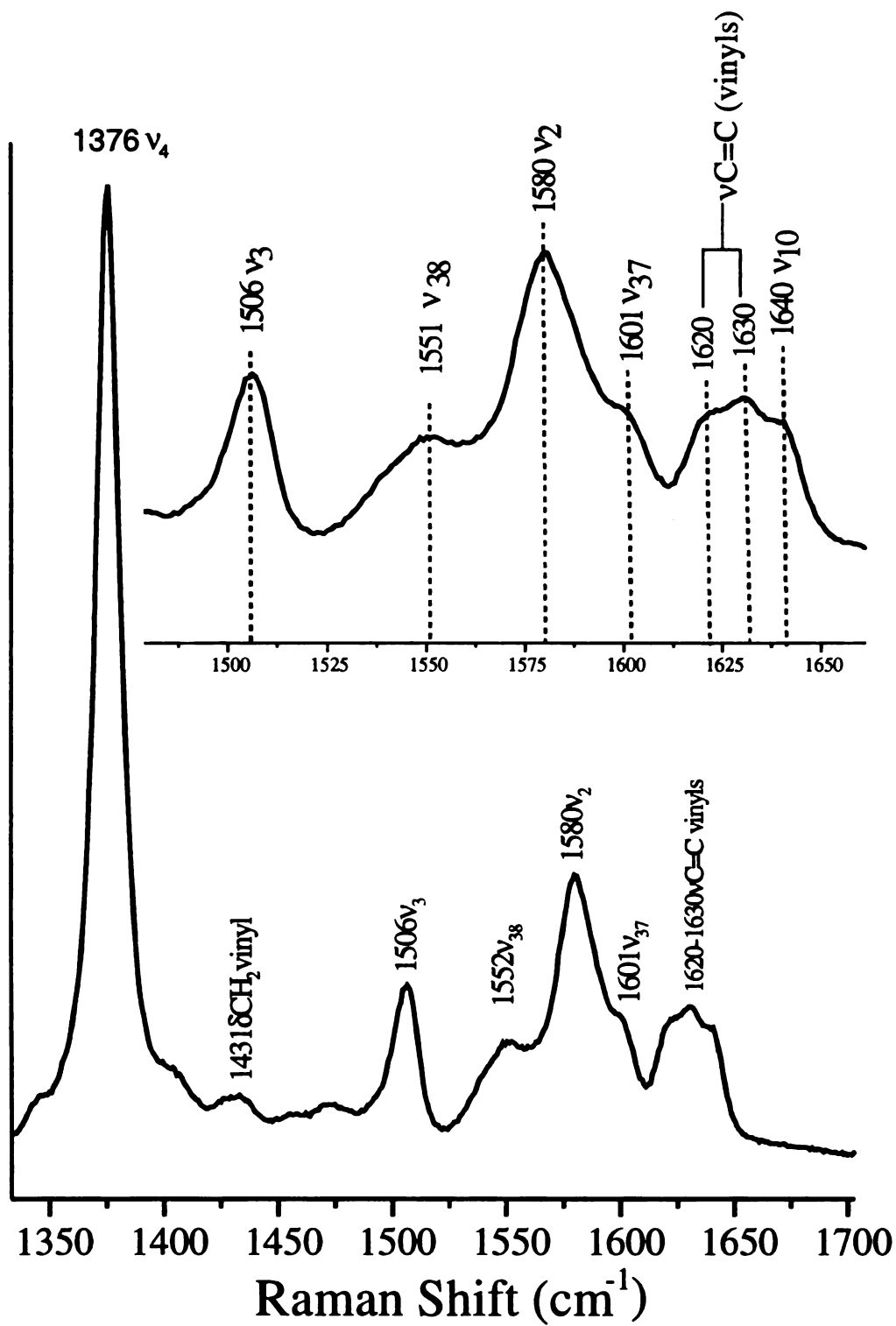
110

Figure 4.1. High frequency region of the resonance Raman spectrum of ferric heme-bound $HR_{ich}P-II$.

Table 4.1. Selected core size markers in the high frequency region of horse heart

myoglobin, ferric heme model complexes, and $HR_{ich}P$-II.

Mode	HHMb(H_2O) (Fe^{+3}6-c hs)[a]	FePP(Im)$_2$ (Fe^{+3} 6-c ls)[b]	FePP(Cl) (Fe^{+3} 5-c hs)[b]	$HR_{ich}P$
$v(C=C)_{vinyls}$	1618	1620	1626	1630, 1620
v_{10}	1608	1640	1626	1640
v_{37}	1583	1602	1591	1601
v_2	1563	1579	1570	1580
v_{19}	1552	1586	1571	
v_{11}	1543	1562	1553	
v_{38}	1514	1554	1533	1551
v_3	1481	1502	1491	1506
v_{28}	1451	1469	1453	
v_4	1373	1373	1373	1376

[a]obtained from reference: (16)

[b]obtained from reference: (7)

abbreviations:

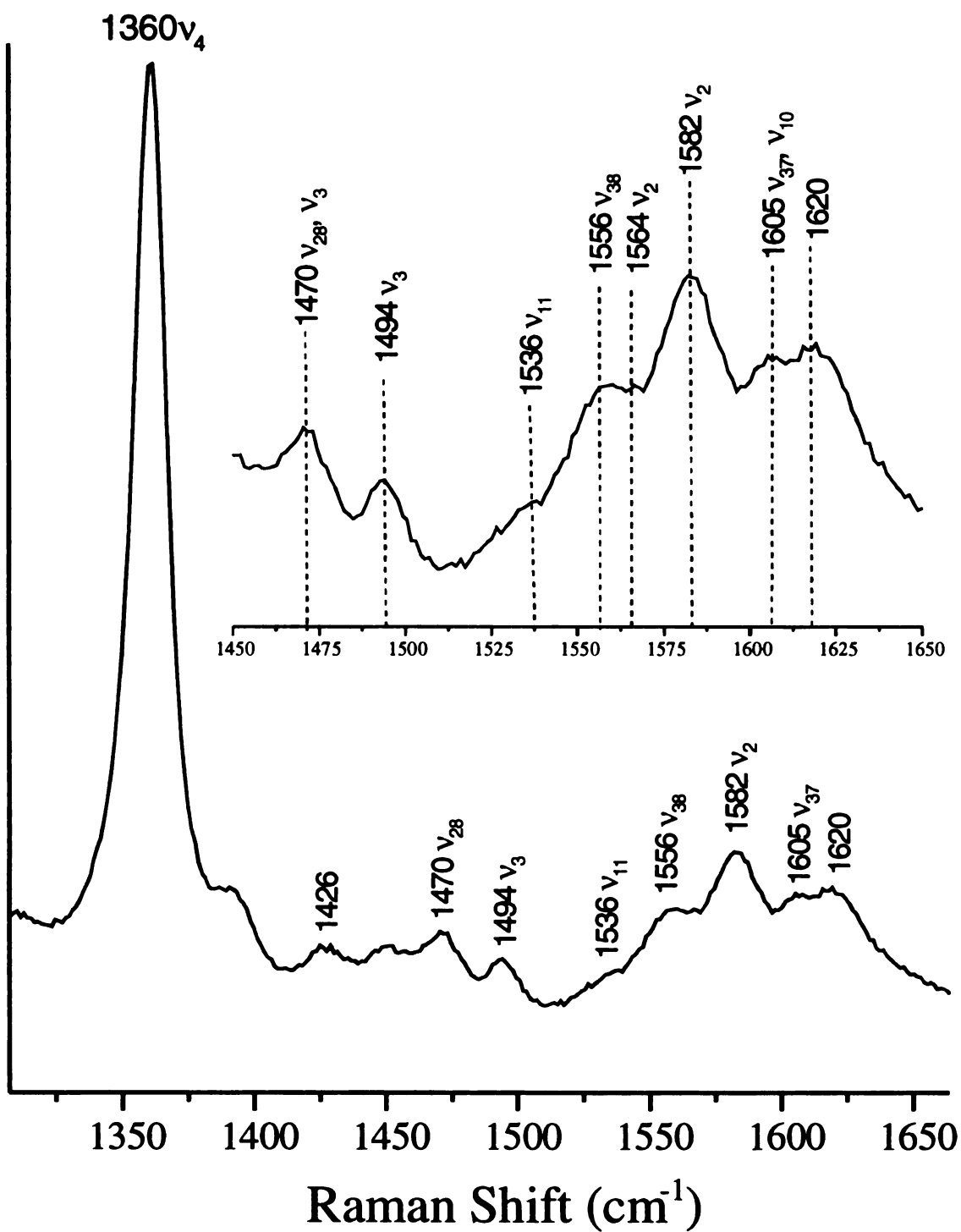PP: protoporphyrin-IX, Im: imidazole, ls: low spin, hs: high spin, 5/6-c: 5/6-coordinate

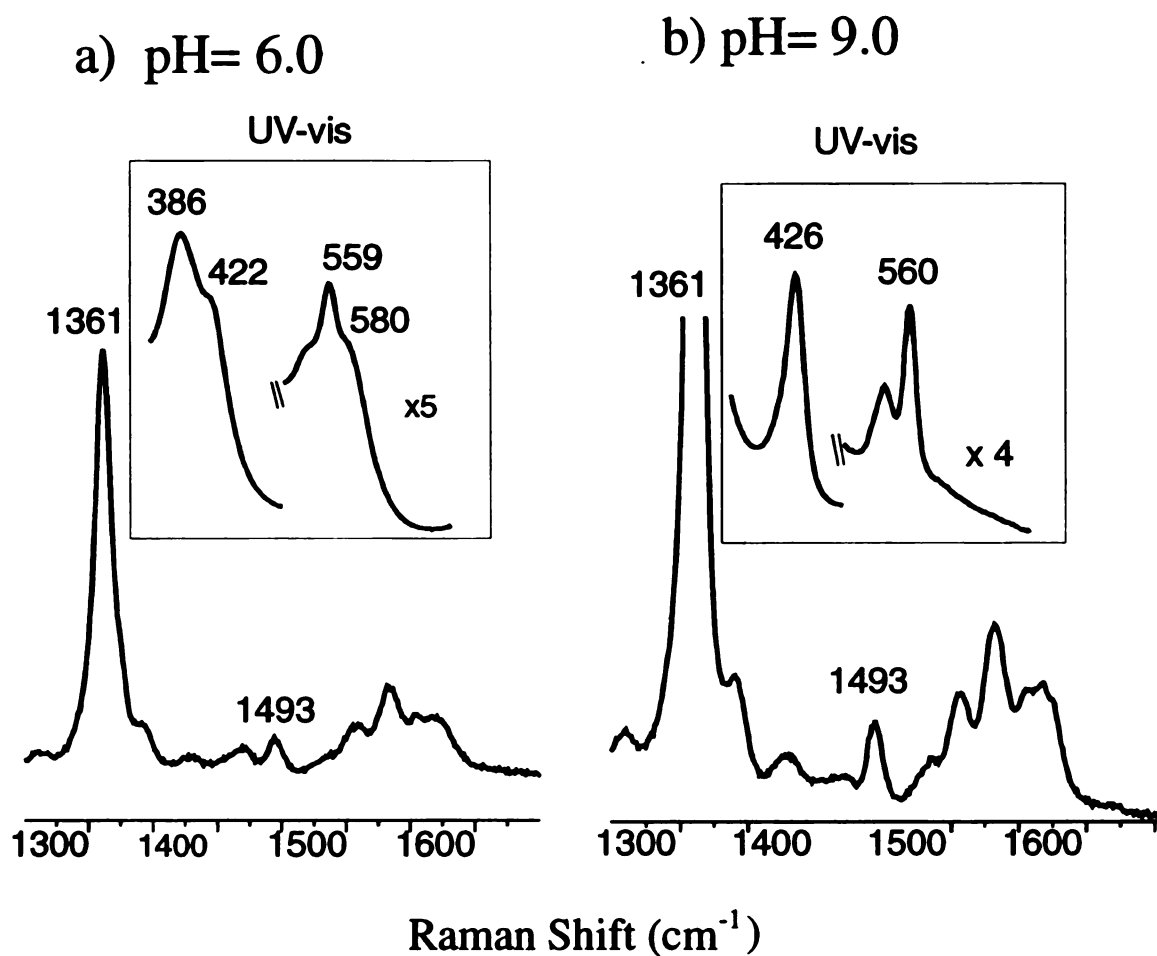**Figure 4.2.** High frequency region of the resonance Raman spectrum of ferrous heme-bound HR$_{ich}$P-II.

Figure 4.3. High frequency region of the resonance Raman spectrum of ferrous heme-bound HR$_{ich}$P-II at pH= 6.0 a), and pH= 9.0 b). The UV-vis spectra are shown in the insets.

Table 4.2. Selected core size markers in the high frequency region of horse heart myoglobin, ferrous heme model complexes, and $HR_{ich}P$-II.

Mode	HHMb (Fe^{+2} 5-c hs)[a]	FePP(Im)$_2$ (Fe^{+2} 6-c ls)[b]	FePP(2-MeIm) (Fe^{+2} 5-c hs)[b]	$HR_{ich}P$
$v(C=C)_{vinyls}$	1617	1620	1622	~1620
v_{10}	1605	1617	1604	
v_{37}	1583	1604	1583	1605
v_2	1565	1584	1562	1582, 1564
v_{19}	1552	1583	1550	
v_{11}	1563	1539	1547	
v_{38}	1522	1560	1521	1551
v_3	1470	1493	1471	1494, 1470
v_{28}	1446	1461		
v_4	1355	1359	1357	1360

[a]obtained from reference: (10)

[b]obtained from reference: (7)

abbreviations:

protoporphyrin-IX - PP, imidazole - Im, low spin - ls, high spin - hs, 5/6-coordinate -5/6-c.

The low frequency region of the resonance Raman spectra of oxidized (ferric), ferrous, and CO-bound ferrous (ferrous-CO) $HR_{ich}P$-II is shown in Figure 4.4. The 150 to 600 cm^{-1} region is expanded in the inset in Figure 4.4. The ferrous spectrum does not show indications of an $Fe-N_{his}$ band in the 150 to 250 cm^{-1} regions, which is expected for six-coordinate complex. The only significant band in this region comes from the ferrous-CO complex, at 238 cm^{-1}. The band at 497 cm^{-1} in the ferrous-CO spectrum is assigned to the $v(Fe-CO)$ stretching mode, as will be demonstrated.

Figure 4.5 shows the low frequency region of the resonance Raman spectra of $HR_{ich}P$-CO at pH=5.5, 7.0 and 9.0. Normal abundance CO ($^{12}C^{16}O$) was used for all samples, while isotopically enriched CO ($^{13}C^{18}O$) was used only for $HR_{ich}P$-CO pH=7.0. The bands at 347 cm^{-1} and 416 cm^{-1} are mode v_8 and the in-plane bending vibration of the vinyls, repectively. No changes are observed in these bands with pH. The strong band at 497 cm^{-1} does not change with pH. This band shifts to 486 cm^{-1} with $^{13}C^{18}O$ at pH=7.0. This shift is in the range expected for a Fe-CO stretching vibration and therefore the 497 cm^{-1} band is assigned to the $v(Fe-CO)$ stretch in $HR_{ich}P$-CO. A smaller band in the 575 cm^{-1} region shifts from under another mode to 556 cm^{-1} with $^{13}C^{18}O$ at pH=7.0. The $\delta(Fe-CO)$ bending mode has been observed in this region for the Fe-CO unit in other heme proteins (17) and similarly the 575 cm^{-1} band may be assigned to the Fe-CO bending vibration in $HR_{ich}P$-CO.

The Raman spectra of the high frequency region (1300 cm^{-1}- 2100 cm^{-1}) of $HR_{ich}P$-CO at pH=5.5, 7.0 and 9.0 are shown in Figure 4.6. The inset shows that isotopic substitution of CO results in a 93 cm^{-1} downshift of the 1953 cm^{-1} band at pH=7.0.
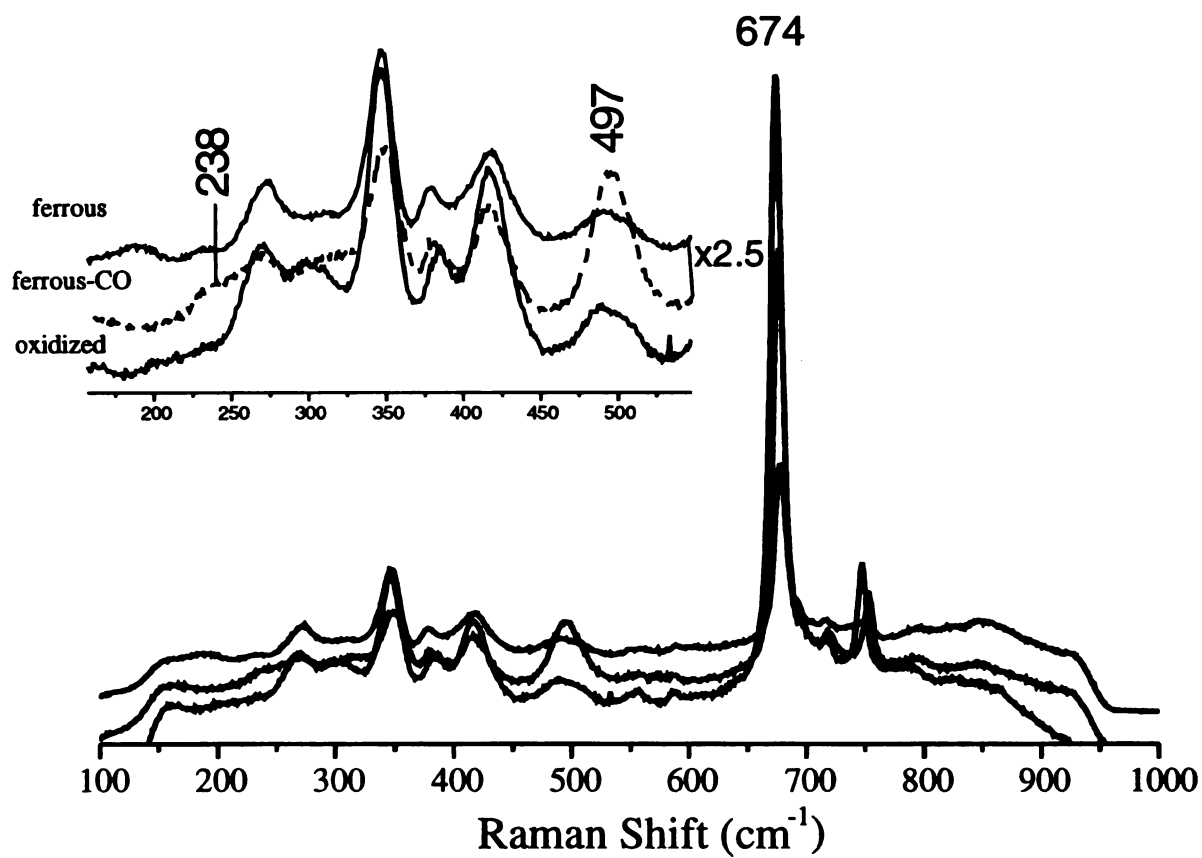
Figure 4.4. Low frequency region of the resonance Raman spectra of ferric, ferrous and ferrous-CO HR$_{ich}$P-II. The Ferrous-CO spectrum is represented by the dashed line.
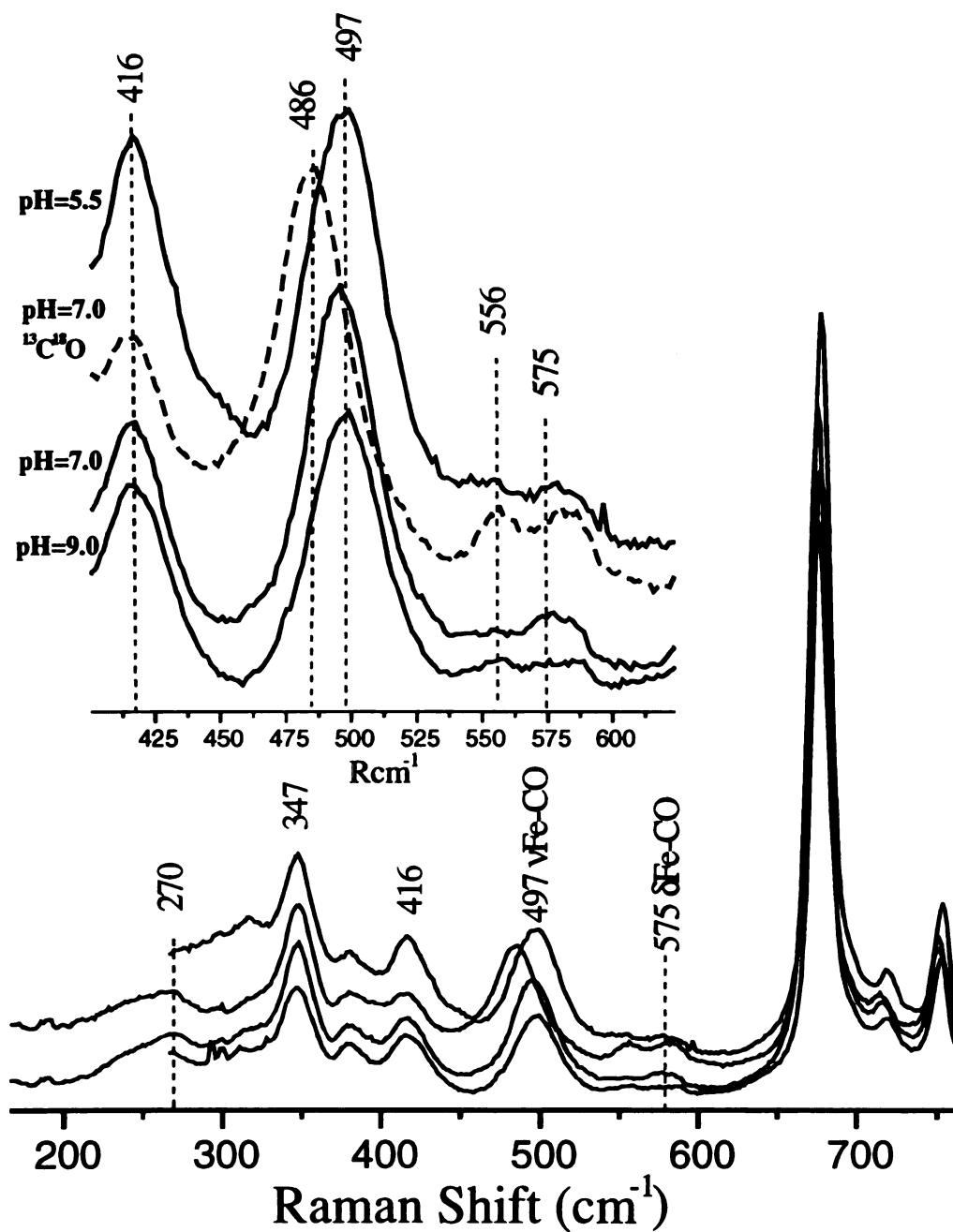
Figure 4.5. Low frequency region of the resonance Raman spectra of ferrous-CO

$HR_{ich}P$-II at pH 5.5, 7.0 and 9.0. The Ferrous-$^{13}C^{18}O$ spectrum is represented by the

dashed line.

118

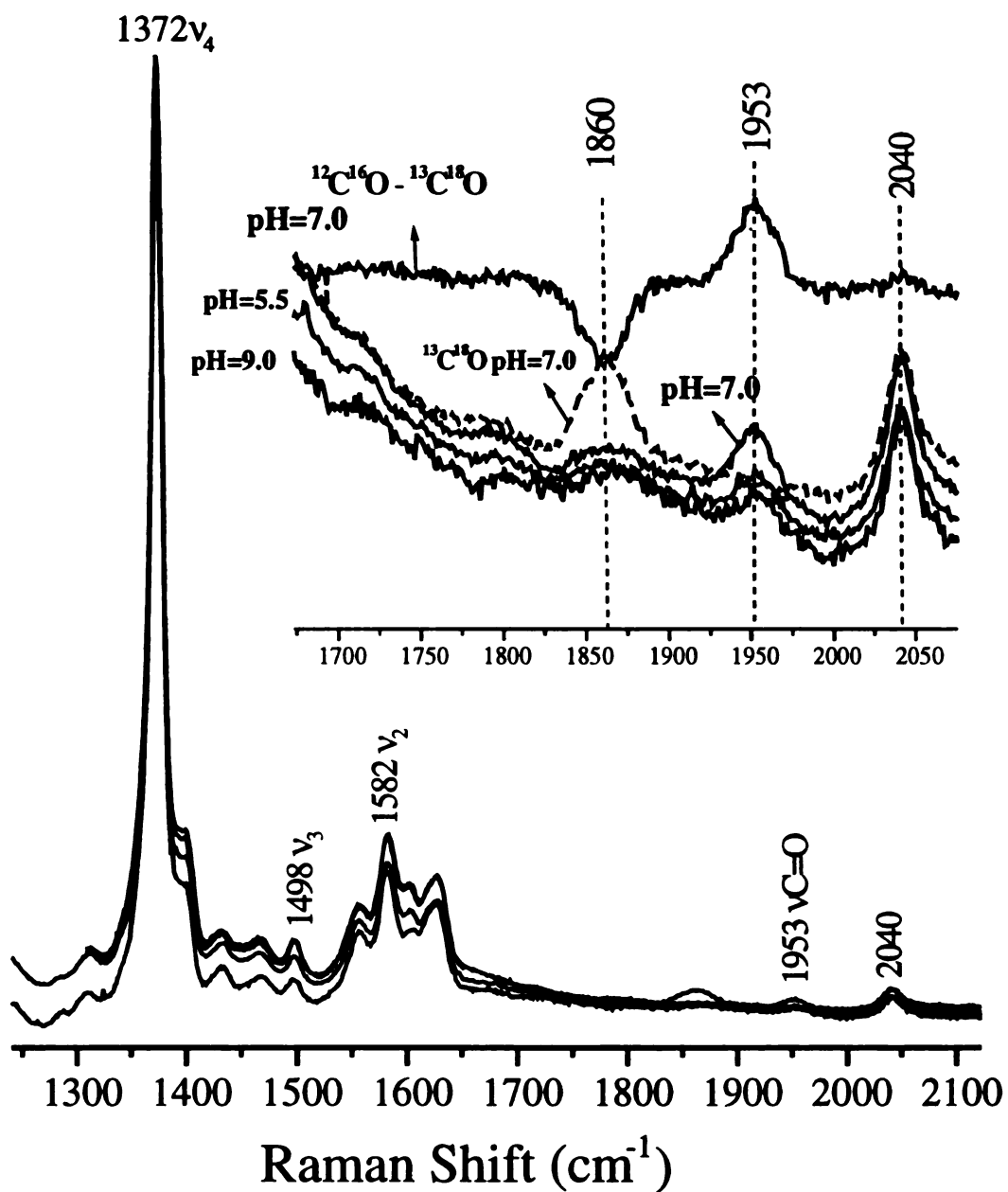**Figure 4.6.** High frequency region of the resonance Raman spectra of ferrous-CO HR$_{ich}$P-II at pH 5.5, 7.0 and 9.0. The Ferrous-^{13}C^{18}O spectrum is represented by the dashed line.

This band corresponds to the CO stretching vibration in $HR_{ich}P$-CO. The frequency of this mode does not change with variation in pH as shown by the spectra at pH=5.5 and 9.0. Vibrations v_3 and v_2 at 1498 cm^{-1} and 1582 cm^{-1} confirm the ferrous low spin state of the heme. However, mode v_4 with a frequency at 1372 cm^{-1}, has a value characteristic of an iron (III) enzyme; the basis for this was explained in Chapter I.

Resonance Raman experiments were done to elucidate the effects of the anti-malarial drug, chloroquine (CQ) (inset of Figure 4.7), on the heme-bound $HR_{ich}P$-II. Figure 4.7 shows the high frequency region of the resonance Raman spectra of the oxidized heme-bound $HR_{ich}P$-II and the same sample incubated with 500 μM CQ, with Raman excitation at 413.1 nm. When $HR_{ich}P$-II was incubated with CQ, the overall intensities of the bands in the Raman spectra decreased in comparison to that of the native $HR_{ich}P$-II. Other than differences in the intensities between these two samples, there are no changes in the "core size marker" modes when the sample is incubated with CQ. The core size marker bands at 1506 and 1581 cm^{-1}, modes v_3 and v_2, respectively, are indicative of the ferric low spin structures. The only observation of a change is the formation of a side band in the CQ-incubated $HR_{ich}P$-II at 1491 cm^{-1}. This small band is v_3 for ferric 5-coordinate heme complex, indicative of free heme.

Since there was no appreciable change in the Raman spectrum of the CQ-incubated $HR_{ich}P$-II at excitation 413.1 nm, Raman experiments were done with excitation at 363.8 nm, the wavelength at which free heme absorbs. Figure 4.8 displays the high frequency region of the Raman spectra of free heme, CQ-incubated free heme, heme-bound $HR_{ich}P$-II, and CQ-incubated heme-bound $HR_{ich}P$-II. The peak at 1492 cm^{-1} (mode v_3) is present in all spectra and is an indication of the presence of 5-coordinate free

heme. The 1506 cm^{-1} peak, mode v_3 for ferric six-coordinate heme iron, is only present in the heme-bound HR$_{ich}$P-II and the CQ-incubated heme-bound HR$_{ich}$P-II. When heme-bound HR$_{ich}$P-II is incubated with CQ, the 1506 cm^{-1} peak decreases while the 1492 cm^{-1} peak increases in comparison to the untreated heme-bound HR$_{ich}$P-II sample. This indicates the loss of heme and formation of free heme when the heme-bound HR$_{ich}$P-II is incubated with CQ. The spectra show that the 1555 cm^{-1} peak is only present when the free heme and heme-bound HR$_{ich}$P-II are incubated with CQ. The origin of this peak is not understood, however the CQ does not coordinate to the heme iron, as the "core size marker" mode v_3 is unaffected when free heme is incubated with CQ. The 1555 cm^{-1} mode may be indications of a different type of interaction between the CQ and free heme, such as π-π stacking as has been reported elsewhere (18,19). Thus, the free heme-CQ complex can be identified by the presence of the 1555 cm^{-1} peak. When the heme-bound HR$_{ich}$P-II is treated with CQ the Raman spectrum shows the presence of 1555 cm^{-1} peak, indications of the formation a free heme-CQ complex.

4.4 Discussion

In a UV-vis spectroscopic study done by Choi et al. (6) it was shown that HR$_{ich}$P-II can bind up to 50 hemes at pH = 7.0. The Raman spectrum of the heme-bound HR$_{ich}$P-II shows that the hemes are ferric six-coordinate low-spin state. When the heme-bound HR$_{ich}$P-II is reduced, the Raman spectrum shows the formation of ferrous six-coordinate low-spin heme iron. Addition of CO to ferrous heme-bound HR$_{ich}$P-II results in the formation of a six-coordinate CO-bound heme complex. With

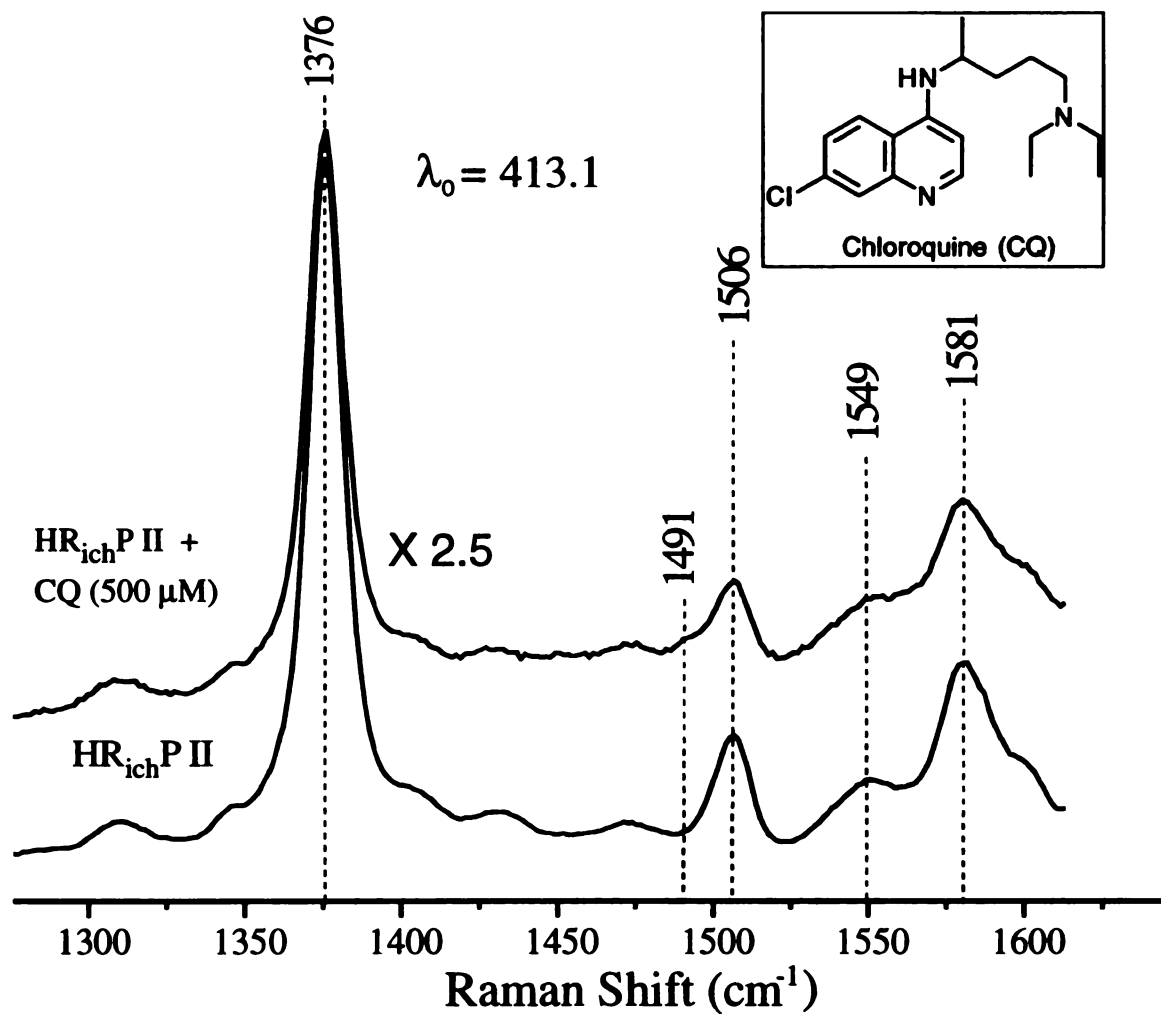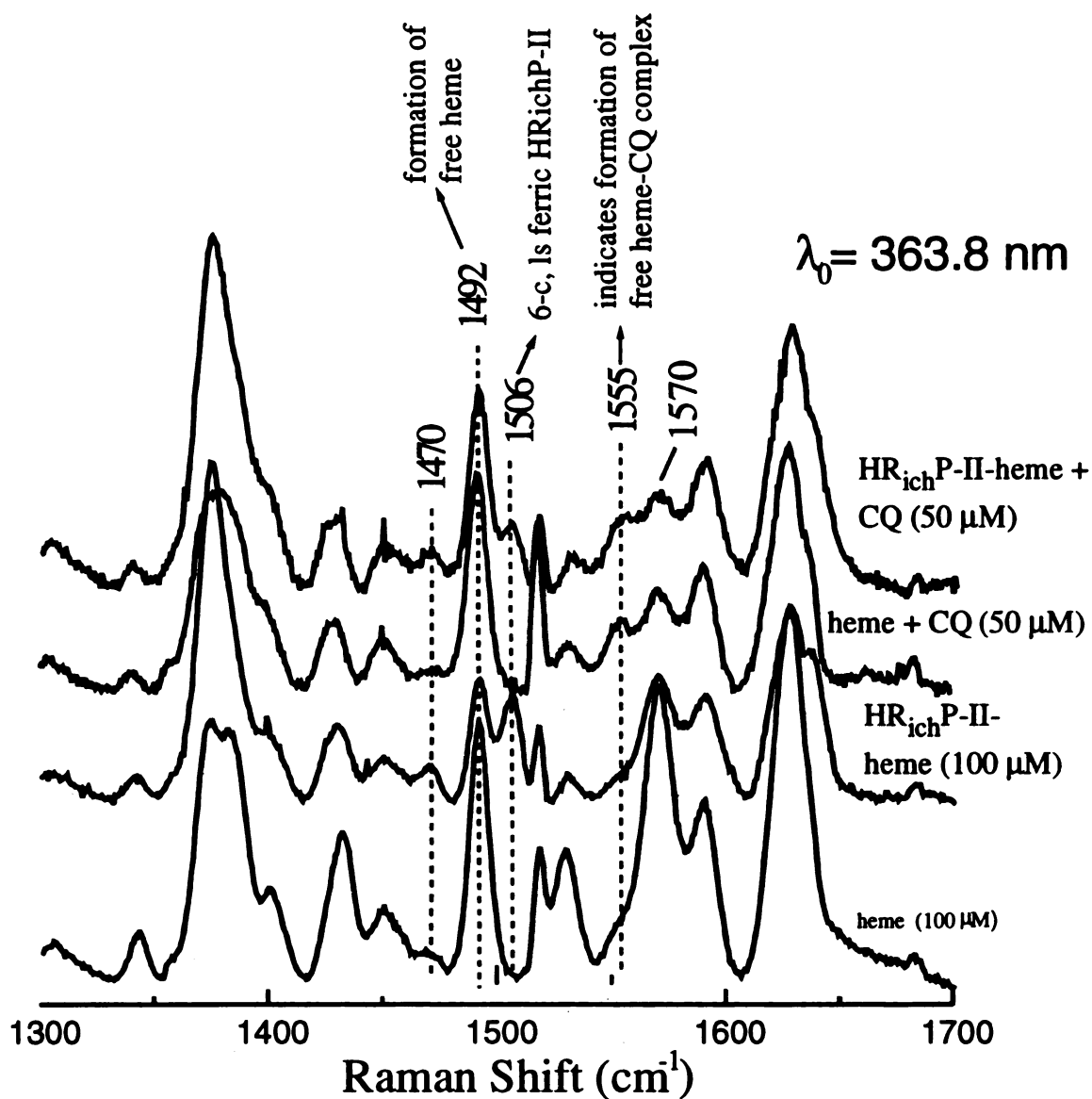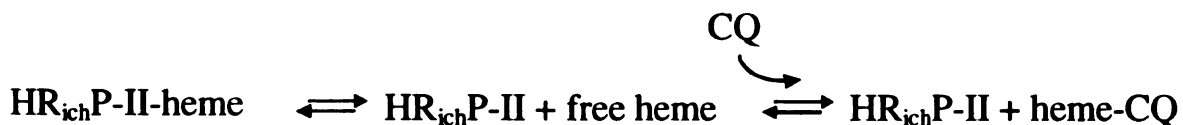**Figure 4.7.** High frequency region of the Raman spectra of ferric heme-bound $HR_{ich}P$-II CQ-incubated ferric heme-bound $HR_{ich}P$-II.

Figure 4.8. High frequency region of the Raman spectra of free heme, CQ-incubated free heme, ferric heme-bound $HR_{ich}P$-II and CQ-incubated ferric heme-bound $HR_{ich}P$-II.

frequency values of $v(Fe-CO) = 497$ cm^{-1} and $v(CO) = 1953$ cm^{-1}, HR$_{ich}$P is found on the curve with imidazole/histidine *trans*-ligands. Therefore, the proximal ligand in HR$_{ich}$P is a histidine. Thus, the oxidized and ferrous six-coordinate hemes are axially coordinated by two histidines. This is in agreement with the amino acid composition of HR$_{ich}$P-II, which contains ~50 pairs of histidines. Tables 4.1 and 4.2 show the resemblance in the frequencies of the high frequency bands between ferric and ferrous heme-bound HR$_{ich}$P-II and the bis-imidazole heme compounds, which further confirms the bis-histidine axial ligation of the hemes in HR$_{ich}$P-II.

The pH of the solution affects the heme-bound HR$_{ich}$P-II. Such effects are demonstrated in Figure 4.2, which show differences in the UV-vis and Raman spectra between ferrous heme-bound HR$_{ich}$P-II at pH=6.0 and that at pH=9.0. The 386 nm band that is formed at pH=6.0 is due to free heme. This band, however, is not present at pH=9.0. In addition, the Raman spectra show that high-spin state heme disappears as the pH is increased from 6.0 to 9.0. This behavior is may be caused by the protonation/deprotonation of the axial histidines in HR$_{ich}$P-II. At high pH, the histidines are deprotonated and the population of six-coordinate heme is high. As the pH decreases, some of the axial histidines become protonated and thus the population of the six-coordinate heme decreases and results in the formation of free heme. Data obtained from the Raman spectra of ferric heme bound HR$_{ich}$P-II show that there are no changes when the pH is varied from 5.5 to 9.0. This is an indication of a pKa change in the axial histidines when the oxidation state of the heme iron changes. The Raman experiments done with the ferrous heme-bound HR$_{ich}$P-II show that the pKa is ~ 7.0. This value is

close to that of histidine. On the other hand, in accordance to what has been observed this work, the pKa of the oxidized heme-bound $HR_{ich}P$-II must be below 5.5. The change in the pKa of the axial histidine with changes in the oxidation state of the heme iron is expected because of the proximity between the heme and the histidines. Thus, the higher oxidized state of the iron cation disfavors formation of a protonated histidine, which results in a lower pKa than that when the heme is iron is in the ferrous state. Since it is proposed that polymerization of free heme occurs at pH< 5.0 in an acidified vacuole (1), $HR_{ich}P$ can maximized heme binding at pH ~ 7.0 when the heme is in its ferric state. The heme polymerization process may occur in two steps: heme binding in the blood stream at pH~ 7.0, and the polymerization step, which occurs in the acidified vacuole. As shown in the Raman experiments, the ferrous state of the heme iron would result in a decreased heme binding of $HR_{ich}P$ at pH~ 7.0. Moreover, it has been shown that the ferrous hemes inhibit heme polymerization and kills malaria parasites (20).

EPR experiments done on ferric heme-bond $HR_{ich}P$-II at pH= 7.0, showed that there is about 5% of high-spin heme (6). The origin of this high-spin heme may be due to the presence of free heme, which is a 5-coordinate complex. In this case, this would indicate an equilibrium between heme-bound $HR_{ich}P$-II and free heme. Since the Raman spectra show that addition of CQ to heme-bound $HR_{ich}P$-II results in the loss of heme, the anti-malarial agent may act by shifting this equilibrium towards the formation of free heme:

$$HR_{ich}P\text{-II-heme} \rightleftharpoons HR_{ich}P\text{-II} + \text{free heme} \xrightarrow{CQ} \rightleftharpoons HR_{ich}P\text{-II} + \text{heme-CQ}$$

This was also proposed by Vippagunta et al. (19), in which calorimetric studies was done to show the formation of a heme-CQ complex when free heme is incubated with the anti-malarial drug. The Raman data shows that formation of a heme-CQ complex may be caused by π-π interaction between the aromatic CQ and one of the pyrrole rings of the porphyrin macrocycle. This is based on the presence of the 1555 cm^{-1} band for heme-CQ complex in Figure 4.8. The frequency of this peak is close to the values of mode v_2 for high-spin heme, which is at 1560 cm^{-1} for the untreated free heme (Figure 4.8). The principal coordinate of vibration of this mode is the C_b-C_b bond from the pyrrole rings, as was discussed in Chapter I. If the interaction between the pyrrole ring and the aromatic CQ is of π $-\pi$ nature, then this should result in the decrease in the frequency of mode v_2. This is because the bond order of the C=C bond in the pyrrole ring will decrease due to the electron density sharing between the aromatic rings. The Raman spectra show that this is the case for the heme-CQ complex since a lower frequency band is formed at 1555 cm^{-1}, in the vicinity the mode v_2; this mode typically have frequency values higher than 1560 cm^{-1} for heme proteins and model compounds (tables 4.1 and 4.2). The addition of CQ to heme-bound $HR_{ich}P$-II also result in an adduct that has a similar spectrum to that of the free heme-CQ complex. In this case a band is also formed at 1555 cm^{-1}, which is not present in the untreated heme-bound $HR_{ich}P$-II. Therefore, CQ may act by sequestering the heme from the heme-bound $HR_{ich}P$-II by forward shifting the equilibrium that results in the conversion of a heme-CQ complex.

4.5 Literature Cited

1. Sullivan, D. J., Gluzman, I. Y., and Goldberg, D. E. (1996) *Science* **271**, 219-222.

2. Bohle, D. S., Conklin, B. J., Cox, D., Madsen, S. K., Paulson, S., Stephens, P. W., and Yee, G. T. (1994) in *Inorganic and Organometallic Polymers Ii* Vol. 572, pp. 497-515.

3. Goldberg, D. E., Slater, A. F. G., Cerami, A., and Henderson, G. B. (1990) *Proc. Natl. Acad. Sci. U. S. A.* **87**, 2931-2935.

4. Pagola, S., Stephens, P. W., Bohle, D. S., Kosar, A. D., and Madsen, S. K. (2000) *Nature* **404**, 307-310.

5. Slater, A. F. G., Swiggard, W. J., Orton, B. R., Flitter, W. D., Goldberg, D. E., Cerami, A., and Henderson, G. B. (1991) *Proc. Natl. Acad. Sci. U. S. A.* **88**, 325-329.

6. Choi, C. Y. H., Cerda, J. F., Chu, H. A., Babcock, G. T., and Marletta, M. A. (1999) *Biochemistry* **38**, 16916-16924.

7. Choi, S., Spiro, T. G., Langry, K. C., Smith, K. M., Budd, D. L., and Lamar, G. N. (1982) *J. Am. Chem. Soc.* **104**, 4345-4351.

8. Choi, S. H., and Spiro, T. G. (1983) *J. Am. Chem. Soc.* **105**, 3683-3692.

9. Choi, S., Spiro, T. G., Langry, K. C., and Smith, K. M. (1982) *J. Am. Chem. Soc.* **104**, 4337-4344.

10. Smulevich, G., Mantini, A. R., Paoli, M., Coletta, M., and Geraci, G. (1995) *Biochemistry* **34**, 7507-7516.

11. Spiro, T. G., and Li, X.-Y. (1988) in *Biological Applications of Raman Spectroscopy* (Spiro, T. G., ed) Vol. 3, pp. 1-38, 3 vols., John Wiley & Sons.

12. Kalsbeck, W. A., Ghosh, A., Pandey, R. K., Smith, K. M., and Bocian, D. F. (1995) *J. Am. Chem. Soc.* **117**, 10959-10968.

13. Gersonde, K., Yu, N. T., Lin, S. H., Smith, K. M., and Parish, D. W. (1989) *Biochemistry* **28**, 3960-3966.

14. Desbois, A., Mazza, G., Stetzkowski, F., and Lutz, M. (1984) *Biochimica Et Biophysica Acta* **785**, 161-176.

15. Desbois, A., Henry, Y., and Lutz, M. (1984) *Biochimica Et Biophysica Acta* **785**, 148-160.

16. Hu, S. Z., Smith, K. M., and Spiro, T. G. (1996) *J. Am. Chem. Soc.* **118**, 12638-12646.

17. Kerr, E. A., and Yu, N. T. (1988) in *Biological Applications of Raman Spectroscopy* (Spiro, T. G., ed) Vol. 3, pp. 39-96, 3 vols., John Wiley & Sons.

18. Vippagunta, S. R., Dorn, A., Matile, H., Bhattacharjee, A. K., Karle, J. M., Ellis, W. Y., Ridley, R. G., and Vennerstrom, J. L. (1999) *J. Med. Chem.* **42**, 4630-4639.

19. Vippagunta, S. R., Dorn, A., Ridley, R. G., and Vennerstrom, J. L. (2000) *Biochim. Biophys. Acta-Gen. Subj.* **1475**, 133-140.

20. Monti, D., Vodopivec, B., Basilico, N., Olliaro, P., and Taramelli, D. (1999) *Biochemistry* **38**, 8858-8863.

CHAPTER V: Conclusions

5.1 Cytochrome *c* oxidase

Time resolved resonance Raman (TRRR) spectroscopy has been used in the past to detect transient intermediates formed during O_2 reduction in cytochrome *c* oxidase (CcO). A number of intermediates, identified by their oxygen-isotope sensitive iron-ligand modes, have been detected by using this technique. Historically there have been an overall agreement in the results obtained by the three labs that have used TRRR for the detection of the intermediates that are formed in the reaction of fully reduced CcO. These intermediates are: Compound A, characterized by its $v(Fe^{2+}-O_2)$ stretching mode at 570 cm^{-1}; Compound F, which has a vibration at 785 cm^{-1} due to the $v(Fe^{4+}=O)$ stretching mode; and Compound H, which is a ferric-hydroxy intermediate with an $v(Fe^{3+}-OH)$ stretching mode at 450 cm^{-1}. However, there has been a controversy to whether or not, Compound P_r is detectable by Raman. Kitagawa's lab has shown that this intermediate has a vibration at 804 cm^{-1} with an intensity as strong as that from Compound F. On the other hand, the Rousseau and Babcock camps have never observed this vibration in the reaction of the fully reduced CcO. In this study, TRRR of the reaction between fully reduced CcO and O_2 have been performed from 25 to 400 μs. In this interval, a vibration at 804 cm^{-1} is observed at 50 μs, after the decay of Compound A and before the appearance of Compound F. Accordingly, this mode has been assigned to the P_r intermediate, which have identical vibration to that of the ferryl-oxo intermediate, P_m, which is produced in the reaction of the mixed-valence CcO. According to this work, based on the intensity of this mode, the population of Compound P_r should not exceed 40% before the appearance of Compound F. The intensity of P_r, as detected in this study,

is not as high as has been detected by Kitagawa and co-workers; therefore, the population, of this intermediate might be affected by the experimental conditions, such as temperature.

In addition, careful examination of the spectra produced by 10-ns laser pulses revealed a new vibration at 590/543 cm^{-1} for the reaction between fully reduced CcO and $^{16}O_2/^{18}O_2$. This mode appears after the decay of the ferrous-oxy (Fe^{2+}-O_2) species at 570 cm^{-1} and parallels the formation of the 786 cm^{-1} band, from the ferryl-oxo unit of compound "F", reaching the plateau at about 400 μs. The intensity of the 590 cm^{-1} mode increases at higher probe power at the expense of the 786 cm^{-1} mode, indicative of a photoreaction involving this ferryl-oxo compound. The formation of this photoinduced is also characterized by the re-reduction of heme a, a process that occurs within the duration of the probe pulse, which in this case was 10 ns. Since the 590 cm^{-1} vibration is not observed during the P_r state of the enzyme, it is proposed that the formation of the photoinduced species proceeds from Compound F due to the structural changes that occurs during the P_r-to-F transition. These changes may result in the proximity of Cu_B to the heme iron of a_3 for which the formation of an iron-oxo adduct with strong interactions with Cu_B is possible. However, the structure of such photoinduced species needs to be experimentally determined.

5.2 Prostaglandin H synthase

In PGHS-1, resonance Raman was used to gain insight about the structure of the peroxidase site. This enzyme has an unusually weak bond between the heme iron and the proximal histidine; $v(Fe-N_{his})$ stretching vibration at 206 and 222 cm^{-1}, which is 20 cm^{-1}

lower than that of other peroxidases. Additional evidence of a weak histidine ligand in

PGHS-1, is supported by the v(Fe-CO) and v(C=O) correlation, which shows that the

frequency values of the v(Fe-CO) and v(C=O) stretching modes at 529 and 1952 cm^{-1},

respectively, correspond to a heme compound with a very weak *trans*-ligand. A strong

bond between the heme iron and the imidazolate at the proximal position is believed to

play an essential role in the mechanism of O-O bond cleavage by most known

peroxidases. However in PGHS-1, the proximal ligand plays a more important role in

terms of the stability of the intermediates that are formed during the peroxidase reaction.

Since, a tyrosyl radical is formed in PGHS-1 (for the cyclooxygenase reaction), the

weaker proximal histidine makes the ferryl-oxo intermediate in PGHS-1 (Compound I) a

better oxidant than that of other peroxidases that are involved instead in the oxidation of

substrates.

5.3 Histidine rich protein II

The majority of the heme structures in the 50-heme-bound HR$_{ich}$P-II, is 6-

coordinate, low-spin, as proven by resonance Raman of the oxidized protein. When the

50-heme bound enzyme is reduced followed by the addition of CO, the enzyme forms a

CO-bound adduct in which one of the axial ligand is displaced by the CO. The v(Fe-CO)

and v(C=O) correlation of the CO-bound HR$_{ich}$P-II shows that the protein contains a

histidine as the *trans*-ligand, thus the hemes in the oxidized HR$_{ich}$P-II are axially ligated

by two histidine ligands. The addition of the antimalarial agent CQ to heme-bound

HR$_{ich}$P-II results in the formation of a heme complex that has a similar spectrum to that

of the free heme-CQ complex. Therefore, CQ may act by sequestering the heme from the

heme-bound HR$_{ich}$P-II to form a heme-CQ complex.